A WAVE ACQUISITION STEREO SYSTEM (WASS) FOR THE PREDICTION OF THE EXPECTED HIGHEST WAVES AND DIRECTIONAL SPECTRA AT THE OCEANOGRAPHIC TOWER 'ACQUA ALTA', VENICE, ITALY

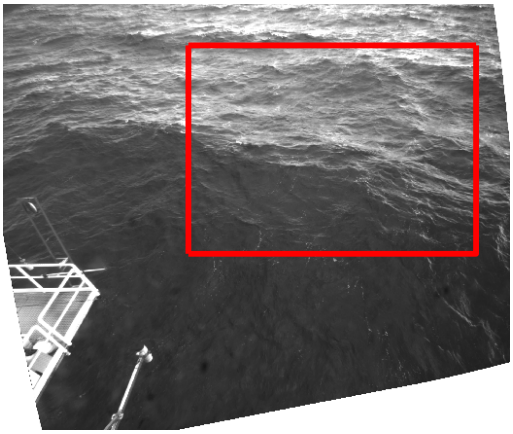

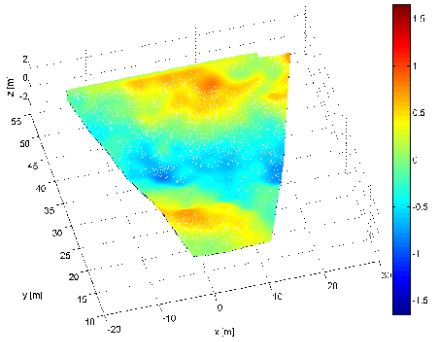

Francesco Fedele
School of Civil and Environmental Engineering
Georgia Institute of Technology, USA

Alvise Benetazzo
PROTECNO S.r.l., ITALY

George Forristall
Forristall Ocean Engineering, Inc., USA

SUMMARY

1. INTRODUCTION

The prediction of large waves is typically based on the statistical analysis of time series of the wave surface displacement retrieved from wave gauges, ultrasonic instruments or buoys at a fixed point P of the ocean. However, in short-crested seas the surface time series gathered at the given location tends to underestimate the true actual wave surface maximum that can occur over a given region of area E_s around P. Indeed, large waves travel on top of wave groups, and the probability that the group passes at its apex through P is practically null. The large crest height recorded in time at P is simply due to the dynamical effects of a wave group that focuses nearby that location within or outside E_s forming a larger wave crest. Thus, point measurements can underestimate the maximum wave group surface height η_{max} attained over E_s, which is not necessarily the highest crest height of the group, unless the area is large enough to cover the entire group dynamics. Indeed, η_{max} can also occur on the region's boundaries, and this is usually the case for smaller areas than the wave group's size. Only in narrow-band sea states, point measurements are exact in predicting such maximum which is expected to be the same at any point in space. However, realistic oceanic conditions are generally short-crested and the expected η_{max} can be underestimated if wave extremes are not modeled both in space and time as maxima of random fields rather than those of random processes of time (Adler 1981, Piterbarg 1995, Adler and Taylor 2007). Quantifying such underestimation is of relevant significance in offshore industry for a proper design of the air gap under the deck of fixed offshore structures. Indeed, localized damages have sometimes been observed on the lower decks of platforms after storms. This may be due to a design that is based on the expected largest crest height from point measurements that underestimate the expected global maximum, i.e. the largest wave surface height, over the rig's area footprint. This can be predicted via applications of Piterbarg's results on global maxima of Gaussian fields (Piterbarg 1995), or by the Euler characteristics of excursion sets (Adler 1981, Adler and Taylor 2007). Forristall (2006) applied for the first time Piterbarg's theorem to the air gap problem showing that it can explain observed damages during hurricanes (Forristall 2007).

The application of such advanced stochastic theories to realistic oceanic conditions requires the availability of wave surface data measurements collected in space on the scale of few hundred meters or smaller. At such scales, the main difficulty for such measurements is that radar or SAR remote sensing is not accurate enough to reconstruct the space-time dynamics and associated spectral properties. On the other hand, a two dimensional wave probe-type array could be used but it can be expensive to install and maintain. A low-cost alternative is a novel non-intrusive optical

sensor, the so-called Wave Acquisition Stereo System (**WASS**) (Benetazzo 2006). **WASS** exploits the state-of-the-art epipolar methods in computer vision (Ma et al. 2004, Benetazzo 2006) for the 3-D stereo reconstruction of both the spatial and temporal dynamics of ocean waves. It has a significant advantage as a low-cost system in both installation and maintenance (Holland et al. 1997, Holland & Holman 1997). A stereo camera view provides both spatial and temporal data whose statistical content is richer than that of a time series retrieved from wave gauges (Benetazzo 2006). Offshore industry can thus benefit from stereo technologies that can *predict the largest wave expected over a given area and the associated spectral properties.*

In this project, we propose **WASS** as a new video observational offshore technology able to provide a multi-dimensional image of the oceanic state for the monitoring of ocean processes or hydrographic factors around offshore structures. Specifically, we have deployed **WASS** at the oceanographic tower '*Acqua Alta'* in the northern Adriatic Sea (Figure 2). As shown in Figure 3, a stereo camera view provides three-dimensional data, both in space and time, whose statistical content is richer than that of a time series retrieved from point probes.

WASS yielded accurate estimates of the oceanic sea state dynamics, the associated directional spectra and wave surface statistics that agree well with theoretical models. We also estimated the expected largest wave surface height over an area via both Piterbarg' s theory (Piterbarg 1995) and the Adler's Euler characteristics (Adler 1981, Adler and Taylor 2007).

Figure 1 – '*Acqua Alta*' tower (Venice, ITALY).

Figure 2 – WASS deployment at '*Acqua Alta*' (Venice, ITALY).

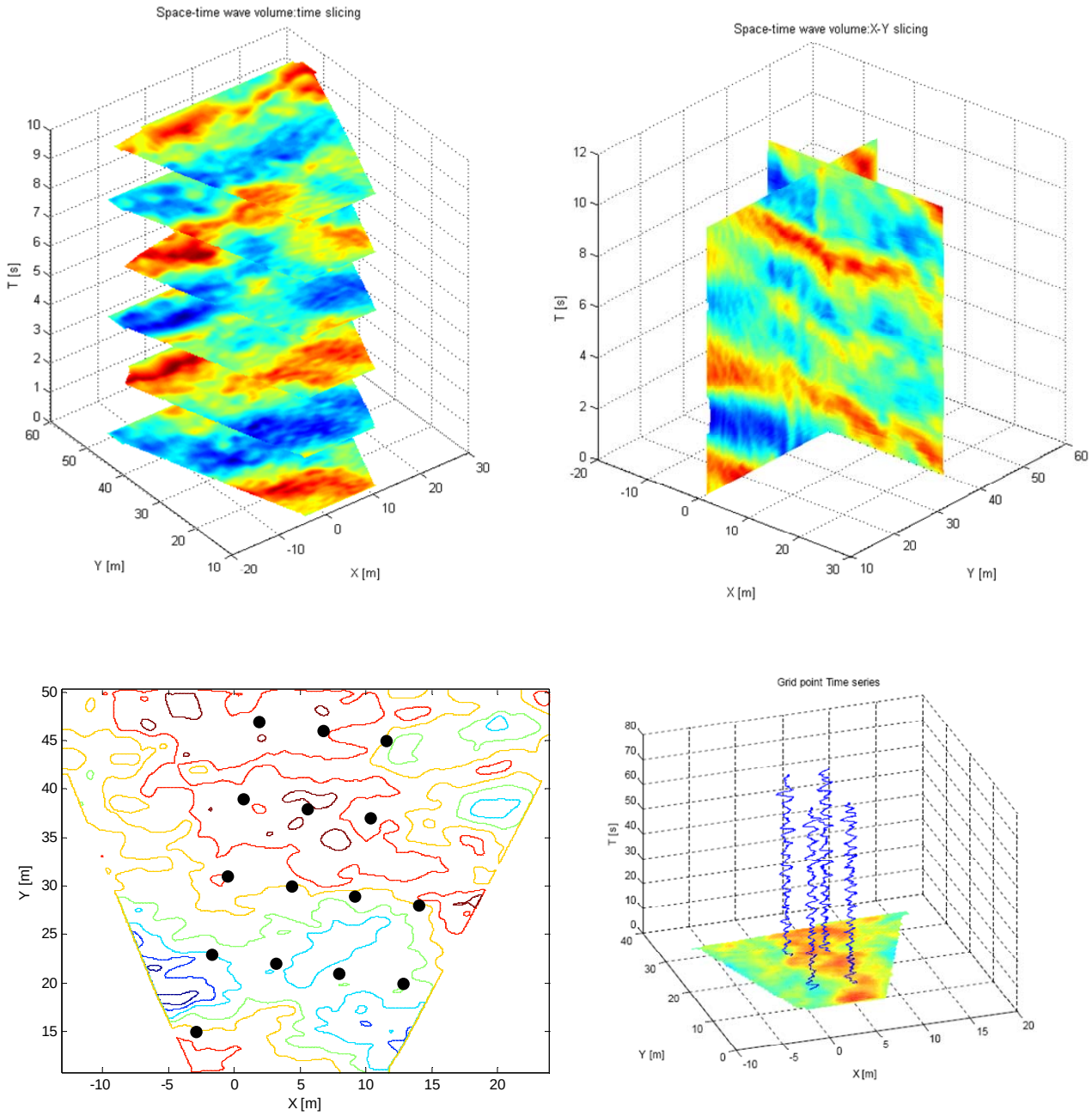

Figure 3 – Example of 3D space-time wave data computed by WASS. (Top-left) horizontal slicing of the wave space-time volume *V* (sequence of snapshots); (Top-right) vertical slicing of *V*; (Bottom-left) location of the virtual probes and (Bottom-right) extracted time series at given virtual point probes.

2. WAVE ACQUISITION STEREO SYSTEM (WASS)

2.1. GENERALITY

Water wave elevations are usually measured by probe-type instruments immersed in water, or linear or 2-D arrays of wave gauges, or using radar-based systems installed on either fixed positions (Dankert et al., 2003) or aircrafts (Hwang et al., 2000). In this scenario, methods of Computer Vision (Ma et al., 2004; Ballard and Brown, 1982) can be successfully exploited to obtain 3-D elevation maps of water waves by using a spatial-widespread and non-intrusive optical system. Moreover, extending image processing on static individual images to image sequences of stereo-pairs enriches the information content of retrieved data. Indeed, the traditional point probes only deliver time series of a quantity (i.e. the water surface elevation) at a fixed or moving point in space. Further, single images give only spatial information (2-D in the case of a single image, 3-D after the stereo reconstruction), while image sequences contain both the temporal and spatial structure of observed phenomena. Image sequences (movies) capture the wave events as best as possible, given a resolution in both time and space and image size. Indeed, for many years images of the water surface in the visible range of the electromagnetic spectrum have provided quantitative information on a number of physical phenomena and parameters associated with the wave dynamics (Dugan et al., 2001; Stockdon and Holman, 2000).

The application of stereo vision to measure the water surface topography started from conventional stereographic technique algorithms used to survey geodetical surfaces or static objects (Klette et al., 1998). However, water surface is a specular object in rapid movement. For this reason each stereo-pair is acquired simultaneously, and the geometry of the stereo system is defined such that the errors due to the surface specularity are minimized. Such techniques were adapted to oceanographic applications in an experiment that used cameras mounted on an ocean going ship (Schumacher, 1939). More recently Coté et al. (1960) demonstrated the use of stereophotography to measure the sea surface topography of long ocean waves. The effort required to extract 3-D elevation maps from an image pair limited the use of this technique to study oceanographic phenomena until late 70s and early 80s (Sugimori, 1975; Holthuijsen, 1983). Nevertheless, the need to measure directional information of waves made stereographic techniques an important investigation tools in oceanographic studies. Shemdin et al. (1988) and Banner et al. (1989) proposed the directional measurements of short ocean waves applying stereography. This experiment used a pair of cameras mounted on an oceanographic offshore tower off San Diego coast (USA) to generate 3-D elevation map of the sea surface from which the directional spectrum

is estimated via Fourier analysis. Banner et al. (1989) applied stereographic measurements in order to study wavenumber spectra of short gravity waves. A quite recent integration of stereographic techniques in oceanography was the WAVESCAN project (Santel et al., 2004) which contributed to the important extension of the analysis of stereographic pairs in time, and Wanek and Wu (2006) proposed a trinocular stereo system for ocean wave detection.

The work presented here proposes a computationally efficient stereo technique that estimates the shape of water waves using video image analysis with both high spatial and temporal resolutions. It employs stereo-based vision of two calibrated views to provide time series of scattered 3-D points of the water surface from a stack of synchronous, overlapping images.

2.2. STEREO ALGORITHM PRINCIPLES

3-D reconstruction is one of the most popular problems in Computer Vision (Faugeras, 1993). One of the earliest methods in this field is stereo analysis, which uses two or more cameras to obtain the 3-D shape of the scene. Stereo analysis can be static if two still images are acquired and used for reconstruction, or dynamic when a movie of the scene is acquired. The main problem in stereo analysis is how to find, given a point in the first image, the corresponding point in the second image. This problem is commonly known as the correspondence problem (Klette et al., 1998). Usually the two cameras are fixed and precalibrated (Zhang, 2000), and the search of correspondences is limited to epipolar lines (Pollefeys, 2000). If the scene is dynamic, i.e. a movie is acquired and objects in the scene are moving, motion can be used to help the research of correspondences and correspondences can be used to infer the motion of rigid bodies in the scene (Kanade and Morris, 1998). This is not the case here, since water waves are definitely far from rigid bodies, and ad-hoc algorithm must be implemented.

In this project the perspective camera model is used. This corresponds to an ideal pinhole camera (Jähne, 1993). Three coordinate systems must be set (Figure 4). The first coordinate system is fixed to the camera observing the scene, and the coordinates are denoted as $X=[X, Y, Z]^T$, where the Z axis coincides with the camera line of sight, and the X and Y axes are parallel to the CCD axes (Charge Coupled Device, i.e. the sensible element of the camera). The camera coordinate system origin is the so-called focal point. Let $X_0=[X_0, Y_0, Z_0]^T$ the 3-D spatial coordinates of a point relative to the Cartesian camera coordinate system, the second coordinate system defines the 2-D image coordinates (in pixels) $J_0=[j_0,i_0]^T$ of the same point. With a CCD camera the relation between these two coordinate systems depends on the focal length, the size and shape of the pixels,

and the position of the CCD chip in the camera-lens system. According to the pinhole approximation, the image coordinates of the point having 3-D coordinates given by [X, Y, Z]^T are:

$$Z\begin{bmatrix} j \\ i \\ 1 \end{bmatrix} = \begin{bmatrix} f_x & 0 & o_x \\ 0 & f_y & o_y \\ 0 & 0 & 1 \end{bmatrix} \begin{bmatrix} 1 & 0 & 0 & 0 \\ 0 & 1 & 0 & 0 \\ 0 & 0 & 1 & 0 \end{bmatrix} \begin{bmatrix} X \\ Y \\ Z \\ 1 \end{bmatrix} \quad (1)$$

with f_x and f_y being the focal length measured in width and height of the pixels, and $[o_x, o_y]^T$ the principal point image coordinates, i.e. the coordinates of the intersection of the camera line of sight with the CCD plane. A third coordinate system is related to the observed scene, and the coordinates are called world coordinates and denoted as X′=[X′,Y′,Z′]T. In this coordinate system, the Z′ axis is parallel to the vertical direction, and the (X′,Y′) plane is parallel to the horizontal plane. The orientation between the camera and world coordinate systems is given by three successive rotations (ϕ, azimuth; τ, tilt; σ, roll) about the axes (Figure 4).

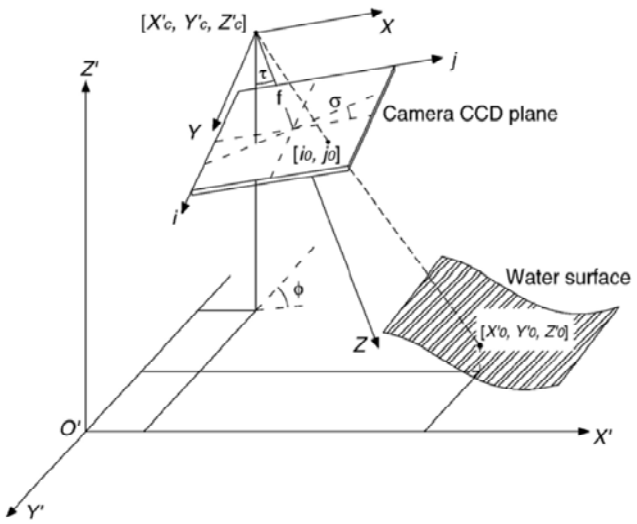

Figure 4 - Relationship between the camera focal point [Xc′, Xc′, Zc′], i.e. the origin of the camera coordinate system, camera coordinates [X,Y,Z], image coordinates [i, j], world coordinates [X′,Y′,Z′], water surface point [X_0,Y_0,Z_0], and rotation angles (ϕ, τ, σ) used in the orientation definition. f is the focal length of the camera-lens system. In figure, the camera CCD and the focal length are magnified.

The complete transformation from world coordinate to camera coordinates (and vice versa) is expressed by the rigid-body motion g=[R,T], which in matrix form becomes

$$g = \begin{bmatrix} R & \mathbf{T} \\ 0_3^T & 1 \end{bmatrix} \quad (2)$$

and then

$$\begin{bmatrix} X \\ Y \\ Z \\ 1 \end{bmatrix} = \begin{bmatrix} R & \mathbf{T} \\ 0_3^T & 1 \end{bmatrix} \begin{bmatrix} X' \\ Y' \\ Z' \\ 1 \end{bmatrix} \tag{3}$$

where R is the rotation matrix (Ma et al., 2004) defined by the three angles (ϕ, τ, σ), and T the translation vector between the origins of the camera and world coordinate systems.

The complete transformation from world coordinates to image coordinates can be then composed of elementary matrices

$$Z\begin{bmatrix} j \\ i \\ 1 \end{bmatrix} = \begin{bmatrix} f_x & 0 & o_x \\ 0 & f_y & o_y \\ 0 & 0 & 1 \end{bmatrix} \begin{bmatrix} 1 & 0 & 0 & 0 \\ 0 & 1 & 0 & 0 \\ 0 & 0 & 1 & 0 \end{bmatrix} \begin{bmatrix} R & \mathbf{T} \\ 0_3^T & 1 \end{bmatrix} \begin{bmatrix} X' \\ Y' \\ Z' \\ 1 \end{bmatrix} \tag{4}$$

which can be simplified to

$$Z\begin{bmatrix} \mathbf{J} \\ 1 \end{bmatrix} = K\Pi_0 g \begin{bmatrix} \mathbf{X'} \\ 1 \end{bmatrix} \tag{5}$$

The constant 3×4 matrix Π_0 represents the perspective projection. Equivalently

$$\begin{bmatrix} \mathbf{J} \\ 1 \end{bmatrix} \approx P \begin{bmatrix} \mathbf{X'} \\ 1 \end{bmatrix} \tag{6}$$

where the 3×4 matrix $P=K\Pi_0 g$ is called camera projection matrix.

The calculation of the 3-D coordinates from corresponding points into the two image planes composing the stereo rig is based on a triangulation resolved by a least square solution. To do this it is necessary to manipulate the camera projection matrix P decomposing it in 4 sub-matrices:

$$P = \begin{bmatrix} D_{2x3} & b_{2x1} \\ q_{1x3} & \gamma_{1x1} \end{bmatrix} \tag{7}$$

so that the projection process can be written as

$$Z\begin{bmatrix} j \\ i \\ \mathbf{1} \end{bmatrix} = \begin{bmatrix} D_{2x3} & b_{2x1} \\ q_{1x3} & \gamma_{1x1} \end{bmatrix} \begin{bmatrix} X' \\ Y' \\ Z' \\ 1 \end{bmatrix} \tag{8}$$

where Z is thought as a proportional coefficient.

From it follows that:

$$Z\begin{bmatrix} j \\ i \\ \mathbf{1} \end{bmatrix} = Z\begin{bmatrix} \mathbf{J} \\ 1 \end{bmatrix} = \begin{bmatrix} D\mathbf{X'}+b \\ q\mathbf{X'}+\gamma \end{bmatrix} \tag{9}$$

which can be decomposed in the system:

$$\begin{cases} \mathbf{J} = (D\mathbf{X}'+b)/Z \\ Z = q\mathbf{X}'+\gamma \end{cases} \tag{10}$$

The camera point J is then expressed as:

$$\mathbf{J} = \frac{(D\mathbf{X}'+b)}{q\mathbf{X}'+\gamma} \tag{11}$$

and then the system (10) can be rewritten as

$$\mathbf{J}(q\mathbf{X}'+\gamma) = D\mathbf{X}'+b \tag{12}$$

or

$$(\mathbf{J}q - D)\mathbf{X}' = b - \gamma\mathbf{J} \tag{13}$$

Knowing the image coordinates (**J**) of the same world point (**X**′) on the two camera planes (L: Left camera; R: Right camera, as depicted in Figure 5, the three coordinates $[X',Y',Z']^T$ are determined solving the system:

$$\begin{cases} (\mathbf{J}_L q_L - D_L)\mathbf{X}' = b_L - \gamma_L \mathbf{J}_L \\ (\mathbf{J}_R q_R - D_R)\mathbf{X}' = b_R - \gamma_R \mathbf{J}_R \end{cases} \tag{14}$$

The previous system in three unknown and four equations cannot be further simplified, and then it must be solved minimizing the squared errors, after each row of the system has been normalized, since the least square method minimizes the distances following a metric proportional to the modulus of each row.

The system (15) is written in terms of 3-D world coordinates X′. In our case, the world coordinate system is a priori unknown. This means that in the stereo method here used, the reference coordinate system is set coincident with the left camera coordinate system of Figure 5. This implies that rotation matrix R and the translation vector T define the mutual position of the cameras' coordinate systems, say the rigid transformation from the right coordinate system to the left coordinate system:

$$\mathbf{X}=\mathbf{X}_L=\boldsymbol{R}\mathbf{X}_R+\mathbf{T}. \tag{15}$$

This rigid motion is obtained by a camera calibration procedure (Ma et al., 2004). In the same way even the effective focal length and principal point coordinates of (7) are determined.

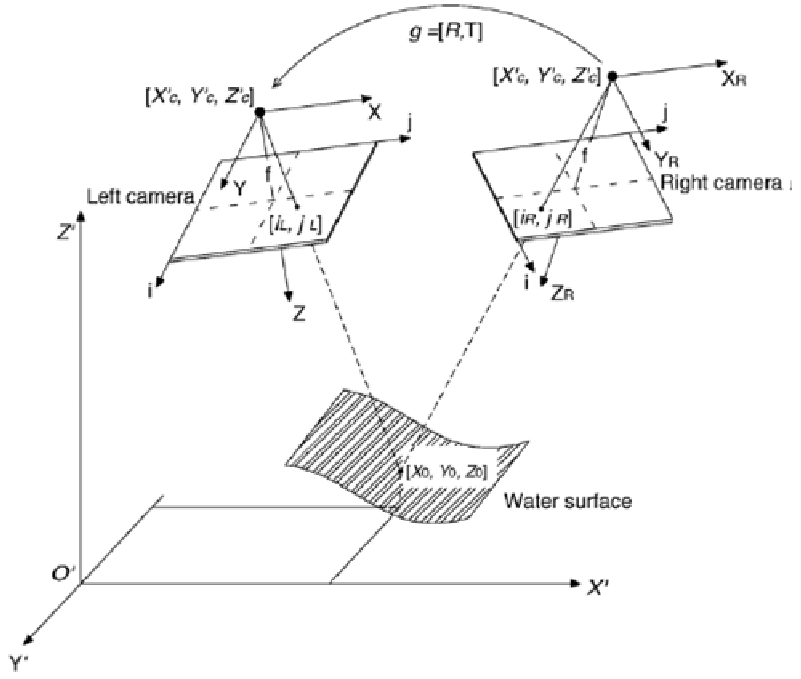

Figure 5 - Set-up of two camera (Left and Right in Figure) stereometric intersection which allows to determinate the three dimensions of a water surface point [X0,Y0,Z0]. [i_L, j_L] and [i_R, j_R] are the Left and Right camera coordinates of the point [X_0,Y_0,Z_0]. g=[R,T] is the rigid transformation between Right [X_R,Y_R,Z_R] and Left [X,Y,Z] camera coordinate systems. In figure, the cameras' CCDs and the focal lengths are magnified.

The stereo-method here proposed is pixel-correlation-based. Window size is kept fixed, since features of water that allow reconstruction (i.e. the water surface reflections) are quite small and homogeneous. Only if the variance of the image gray values in this window is higher than a selected threshold, the search of the corresponding pixel starts. To automatically find the corresponding pixel in the stereo images the principles of epipolar geometry are exploited (Ma et al., 2004). In particular, even if in an optical system the exact position of the 3-D point X_0 is not known, it is bound to lie on the optical axis passing through the corresponding image point J_0 (Figure 4). In a stereo system (Figure 5), if J_L is the left image point of a 3-D point, the unknown corresponding right image point J_R will be on the projection of the optical axis, relative to J_L, on the right image plane. Manipulating the system (16), the equation of this projection (called epipolar line) can be derived (Benetazzo, 2006). On the epipolar line, the corresponding point is searched (Figure 6).

To find the correspondences, cross-correlation is used and a pyramidal search is implemented. The pyramidal process of stereo matching starts from few pixels on a regular grid on the left camera plane, and then iterates the process refining the regular grid in subsequent steps, to obtain a dense disparity map. At the first step, for each pixel of the grid, the correspondence is searched over all

the epipolar line on the right camera plane. The right image pixel whose cross-correlation coefficient is highest is selected as the corresponding point. Only if this coefficient goes over a threshold value (set equal to 0.85) the position of the corresponding pixels in the two image planes and the cameras' projection matrices are used to determine the 3-D coordinates $[X, Y, Z]^T$ of the water surface at the selected point. In the first step, the few pixels of the grid allow only a first approximation of the water surface. Then, the hypothesis that the water surface can be locally approximated by a planar surface is exploited (Figure 7). In the second step, the grid is refined and for each pixel of the new grid this hypothesis constrains the possible location of the corresponding point over a small portion of the epipolar line.

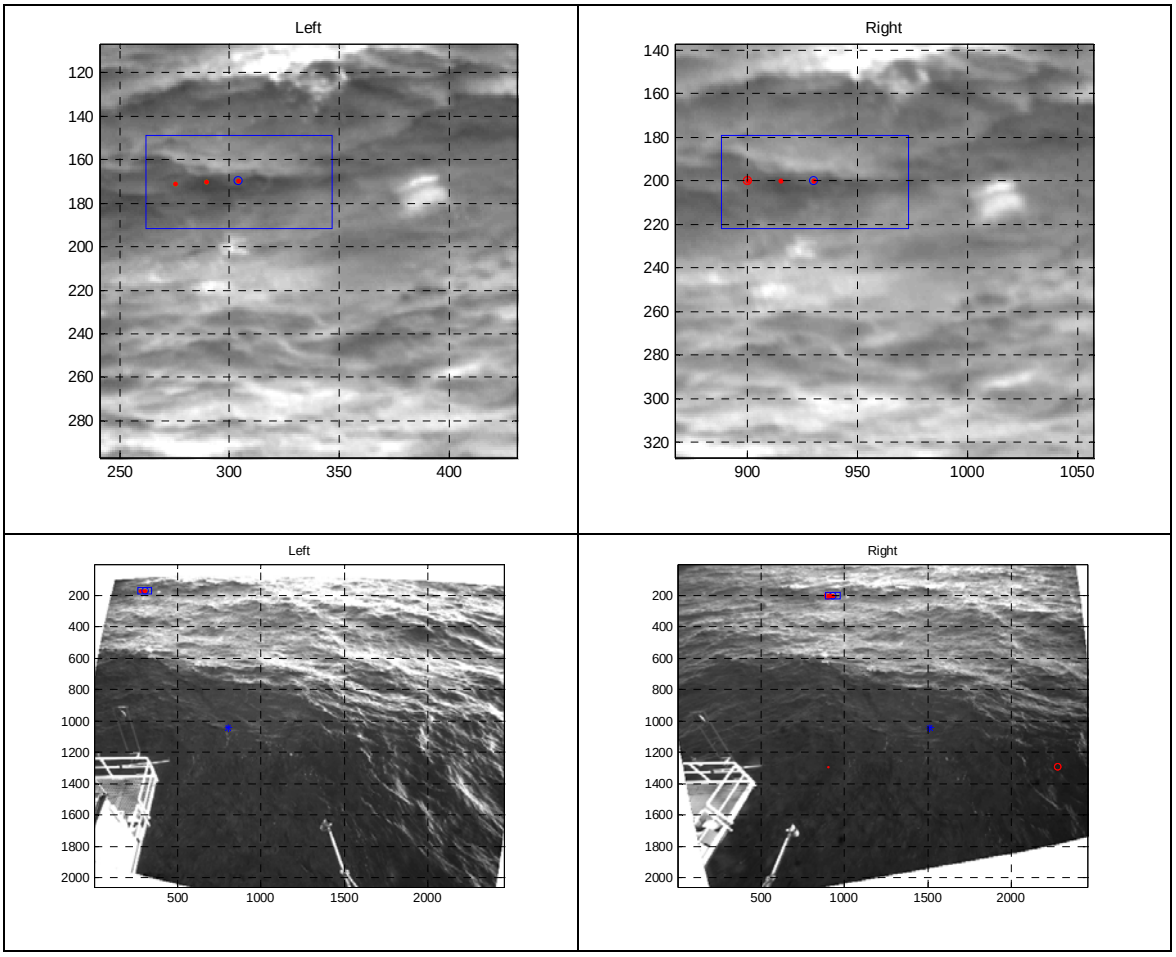

Figure 6 – Example of corresponding pixels between Left and Right images of stereo rig.

This reduces the number of cross-correlations that must be computed and saves computational time. New correspondences are defined and, if the maximum cross-correlation coefficients go over the selected threshold, new 3-D position of the water surface are determined. The 3-D water surface shape is refined with new points, which allow to estimate a new local planar approximation.

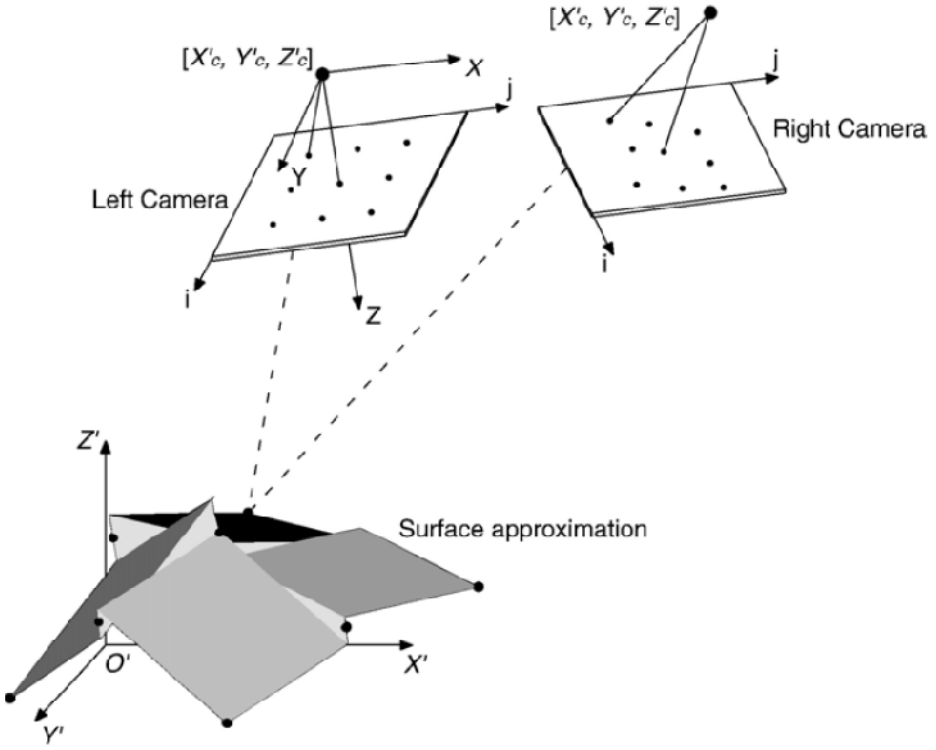

Figure 7 - First step of the pyramidal search. On the Left camera image, pixels on a regular grid are selected (black circles). The search algorithm determines the position of the corresponding pixels in the Right image (black circles). By exploiting the stereo method the 3-D positions (in the Left camera Cartesian coordinate system) of the selected points are determined. These give a first approximation of the surface being analyzed. Locally, the surface is approximated by a plane. The dashed line represents an example of the intersection of the cameras' lines of sight. In figure the cameras' CCDs and the 3-D surface are magnified.

After the triangulation process, the positions of the 3-D water surface points in space and time are given in the left camera coordinate system. Afterwards, to analyze these data it is necessary to rotate the 3-D points in order to set the Z axis aligned in the direction of the gravity acceleration. Generally, no known references that allow a reliable Z′ axis to be computed are present in the images. A challenging application, at least from an operational point of view, is the transformation of 3-D coordinates from the camera coordinate system (image plane and camera line of sight) to world coordinate system (horizontal plane and vertical direction). This rigid transformation is completely described by a rotation matrix, ***R***, and a translation vector **T**, such that

$$\mathbf{X}'=\boldsymbol{R}\mathbf{X}+\mathbf{T}. \qquad (16)$$

For a given sequence, the gravity direction can be found exploiting the hypothesis that the mean time water surface elevation map is a plane, representing the water surface without waves, orthogonal to gravity direction. In fact, it is fair to assume that over a long period of time (say, at

least ten times the dominant period of the waves), the time–mean water surface elevation on a single point on the surface will be zero (if no long period waves are observed).

In the camera coordinate system, the equation of the mean plane ($aX+bY+cZ+d=0$) is obtained through a least square solution. For each point, the water elevation (in the world coordinate system) is calculated as the distance from the mean plane. Then, the last row of the rotation matrix, R, is given

$$r_3 = \frac{\begin{bmatrix} a & b & -1 \end{bmatrix}^T}{\sqrt{a^2+b^2+1}} \tag{17}$$

For a given $[X,Y,Z]^T$ point, the water surface elevation evaluated from the horizontal mean plane can then be expressed as

$$Z' = r_3 \begin{bmatrix} X \\ Y \\ Z \end{bmatrix} + \frac{d}{\sqrt{a^2+b^2+1}} \tag{18}$$

The other two rows are computed with the assumption that R is orthogonal and normalized:

$$r_1 = \frac{\begin{bmatrix} a, -(1+a^2)/b, -1 \end{bmatrix}^T}{\sqrt{a^2+((1+a^2)/b)^2+1}} \tag{19}$$

$$r_2 = \frac{\begin{bmatrix} b, 0, ab \end{bmatrix}^T}{\sqrt{a^2b^2+b^2}} \tag{20}$$

and finally

$$R = \begin{bmatrix} r_1 \\ r_2 \\ r_3 \end{bmatrix} \tag{21}$$

where a and b are the parameters from the equation of the mean plane.

Thus, the transformation between camera and world coordinate systems is given by

$$\begin{bmatrix} X' \\ Y' \\ Z' \end{bmatrix} = R \begin{bmatrix} X \\ Y \\ Z \end{bmatrix} + \begin{bmatrix} 0 \\ 0 \\ \frac{d}{\sqrt{a^2+b^2+1}} \end{bmatrix} \tag{22}$$

The individual elements R_{ij} of the 3×3 orthonormal rotation matrix are exploited to calculated the three successive rotations (ϕ, azimuth; τ, tilt; σ, roll) about the camera axes (Figure 4).

Figure 8 shows an example of all the processes describe to obtain 3D coordinates in World reference system. Figure 9 shows an example of 2D water elevation map in world reference system.

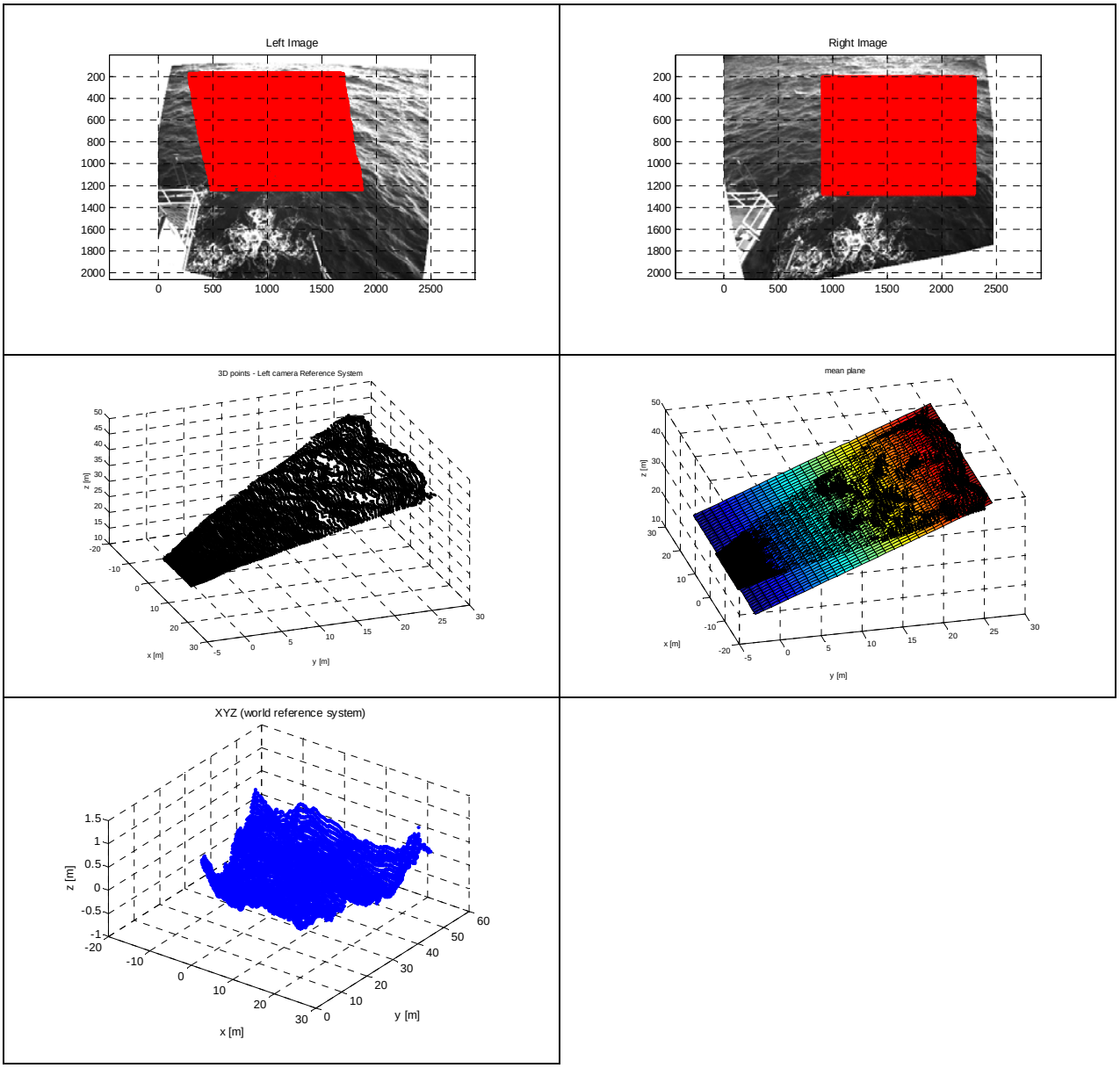

Figure 8 - Sketch of principal steps of stereo algorithm base on epipolar geometry. Top-row: corresponding points between left and right images of stereo pairs. Central-row: 3D points in camera reference system, and mean plane of data. Bottom-row: rotation of 3D data set to the z axis parallel to vertical direction.

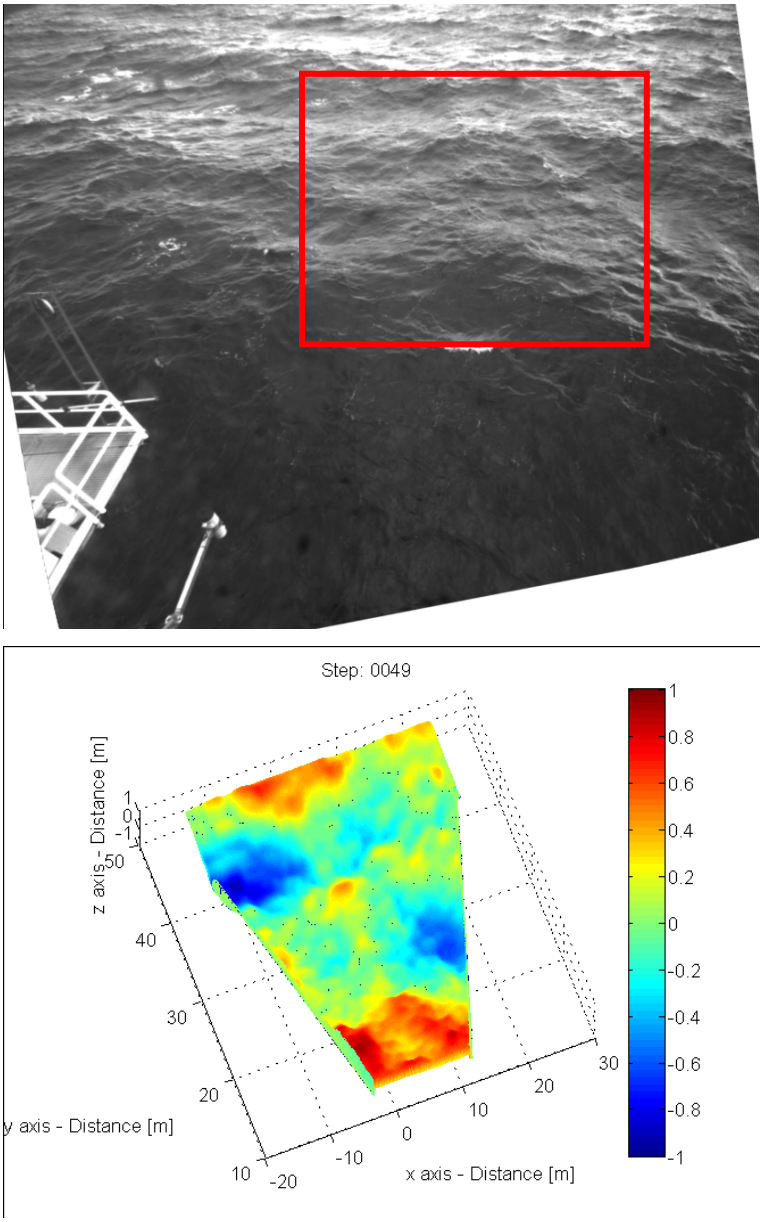

Figure 9 - Example of 2D water elevation map in world the reference system.

2.3. ACCURACY OF STEREO MEASUREMENTS OF SEA WATER SURFACE BY WASS

In this project a window stereo matching algorithm is used. Usually stereo matching works properly if the surface is not reflective and has Lambertian properties (Jähne, 1997). However it can be shown (Jähne, 1993) that some conditions on the position of cameras and characteristics of the surface allow the reflections to be considered as texture on the water surface. After stereo-matching and triangulation, elevations of the waves can be determined with a bias, which is due to the specular properties of the surface. Such bias depends on both the wavelength of the waves and their steepness. It is small for steep waves, i.e. when the angle formed by the slope with the horizontal plane is much larger than the inclination of the lines of sight of the cameras. Thus, this error can be reduced using a small angle between the lines of sight of the cameras; however, this increases the quantization error. A trade-off has to be found: the geometry of the camera set-up used for this work is characterized by a base to height ratio, $|\mathbf{T}|/Z_0$ (Figure 5), of about 0.1, and the inclination of the line of sight of the cameras is about 0.05 radiants. This is a very small value, if compared with typical maximum slopes of waves: therefore waves can be reconstructed with accuracy. A summary (after Jähne, 1993) of the characteristics of the stereo camera set-up used in recent investigations to measure the height of ocean waves is summarized in Table 1, where Res is the resolution. We justify the high values of the ratio $|\mathbf{T}|/Z_0$ given in Table 1, through the need, for the authors, to keep high resolution. The water surface specularity was not a problem, since the stereo-correlation in all the works cited was done using an analytical plotter instead of an automatic algorithm as in the project presented herein.

Reference	$\|\mathbf{T}\|/Z_0$	Size (m × m)	*Z*-Res (mm)	*X*/*Y*-Res (mm)
Coté et al. (1960)	0.6	900 × 600	150	600
Dobson (1970)	n/a	3.6 × 3.6	0.75	n/a
Holthuijsen (1983)	≈ 0.5	(54–220) × (54–220)	n/a	n/a
Shemdin et al. (1988)	0.4	2.5 × 2.5	3	8.5
Banner et al. (1989)	0.3-0.4	2.0 × 2.0	1	n/a
Santel et al. (2004)	0.25-1.0	200 × 200	40	40–80

Table 1 - Summary of the characteristics of the stereo set-up used in different investigation to measure the 3-D shape of water waves.

A systematic source of error, intrinsic to stereo processing, is the resolution error, the so called quantization error. It arises from pixels quantization operated by the CCD, and from the

triangulation process. The quantization error is not uniform in the matched area, and only its maximum value may be estimated. The 2-D model of the stereo rig geometry is shown in Figure 10, where the $\hat{Z}$ axis is perpendicular to the baseline *b*, and the $\hat{X}$ axis is parallel to the baseline. The achievable 3-D accuracy is influenced by the object distance ($\hat{Z}$), the focal length (f), the camera resolution (i.e. the CCD physical size, equal to the number of pixels times the CCD cell size) and the cameras' mutual position (**T**), as well as the angle between the cameras' lines of sight (α). The *m* and *n* axes are the image coordinates of the pixels on the first and the second image, relative to the principal points of the CCDs. In this 2-D model the CCD is approximated with a only one axis, i.e. it degenerates to a segment. If *N* is the number of pixels of this 1-D CCD, the quantization effect is maximum when *m*=− *N*/2, *n*=N/2. The maximum absolute error, $er_{\hat{Z}}$, along the $\hat{Z}$ axis is given, for a distance $\hat{Z}$ from the baseline, by:

$$e_{r\hat{Z}} = \frac{\hat{Z}^2}{2|\mathbf{T}|\,N}\frac{\sin(2\beta)}{\cos(\beta+\alpha)^2} \tag{23}$$

where β is half the angle of view of the cameras. The maximum errors on $\hat{X}$ axis is only due to pixel resolution (differently from the error on $\hat{X}$ axis, which is due to the triangulation), and it is equal to:

$$e_{r\hat{X}} = \frac{\hat{Z}}{2N}\frac{\sin(2\beta)}{\cos(\beta+\alpha)^2} \tag{24}$$

The extension to the third axis $\hat{Y}$ (such that $\hat{X}$, $\hat{Y}$, $\hat{Z}$ axes are an orthonormal space) gives for the maximum error the relation

$$e_{r\hat{Y}} = \frac{\hat{Z}}{2N}\frac{\sin(2\beta)}{\cos(\beta)^2} \tag{25}$$

The $\hat{X}$, $\hat{Y}$, $\hat{Z}$ axes are considered parallel to the X, Y, Z axes of Figure 10 given the small values of α. This means that the previous formulae will be exploited to estimate the errors in the camera coordinate system.

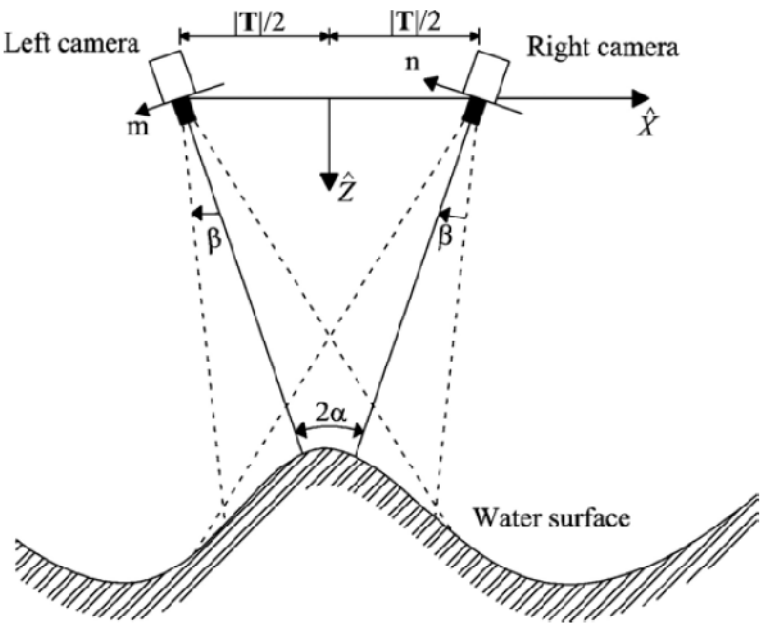

Figure 10 - 2-D projection of the acquisition set-up. The direction $\hat{X}$ is defined by the line (baseline) connecting the two cameras' focal points. $\hat{Z}$ is the direction orthogonal to the baseline and lying in the plane defined by the lines of sight of the cameras. The two cameras lines of sight are not parallel.

The errors in the world coordinate system are calculated from the errors in the camera coordinate system applying the rotation matrix R which transforms the camera coordinate system to the world coordinate system:

$$\begin{bmatrix} er_{X'} \\ er_{Y'} \\ er_{Z'} \end{bmatrix} = R \begin{bmatrix} er_X \\ er_Y \\ er_Z \end{bmatrix} \tag{26}$$

Another possible error in the stereo analysis is the matching error. There are two types of matching errors, false negative (or missed matches) and false positive (or erroneously made matches). Only the uncorrected matches are taken into consideration here. In order to estimate their effect in the 3-D stereo measurement, a series of virtual experiments are carried out. Two hundreds images reproducing natural and artificial subjects were created, and some stereo-images of real water waves were taken into consideration. The virtual stereo rig consists of a couple of 480×640 pixel cameras. The baseline, |**T**|, is set to 1.0 m and the mean distance between the baseline and the target, Z_0, is 10.0 m. The angle of view of each camera is 43°, and the angle between the camera lines of sight is 4°. In this condition the maximum quantization error in the Z direction is approximately 0.065 m. Each virtual image is projected on a synthetic sinusoidal waveform

(wavelength equal to 10 m, and wave amplitude equal to 0.5 m) as texture. The textured wave is then projected on the two camera planes forming the stereo rig using the projection matrix of the camera model. Then, images are corrupted with a Gaussian noise, with the characteristics of the signal-to-noise ratio of a real CCD. At the end, the stereo algorithm is applied. The water surface shape is reconstructed and the original synthetic wave is compared with its stereo reconstruction. For each point, the error in the water elevation measurement is computed as the difference between the measured elevation and the elevation of the original synthetic wave. Without loss of generality, the position of the cameras has been chosen according to a simple rotation around the left camera *Y* axis and a translation parallel to the same axis. In real experiments the cameras will always be positioned close to this situation. We note that an important parameter which describes the possibility to find reliable matches between images is the variance along the epipolar lines of images:

$$LV_i(\mathrm{Im}) = E_{(j)}\left[(\mathrm{Im}(i,j) - \mathrm{Im}(i,j+1))^2\right] \qquad (27)$$

where *Im(i, j)* is the intensity value of the pixel at position (*i, j*) and $E_{(j)}$ is the expectation operator along the coordinate *j* of the epipolar line in the image coordinate system (Figure 11).

Figure 11 shows an example of the relation between the variance of the errors (that include both the matching error and quantization error intrinsic in the triangulation process) and the epipolar line variance $LV_i(Im)$, relative to the virtual experiments described. The curve approximately follows an hyperbole. Assuming a normal distribution of errors (matching+quantization), the contribution of the matching error, for the virtual stereo rig used, in the definition of the maximum expected error ranges between 0.005 mm and 0.800 m, in dependence on LV_i parameter. We can note that the natural wave texture is such that the epipolar line variance is sufficiently high to consider this error generally negligible in the water elevation measurement with stereo techniques, under the condition of base to height ratio approximately 0.1. In the stereo method it is implemented even a 2-D sub-pixel detector to improve accuracy of correspondences.

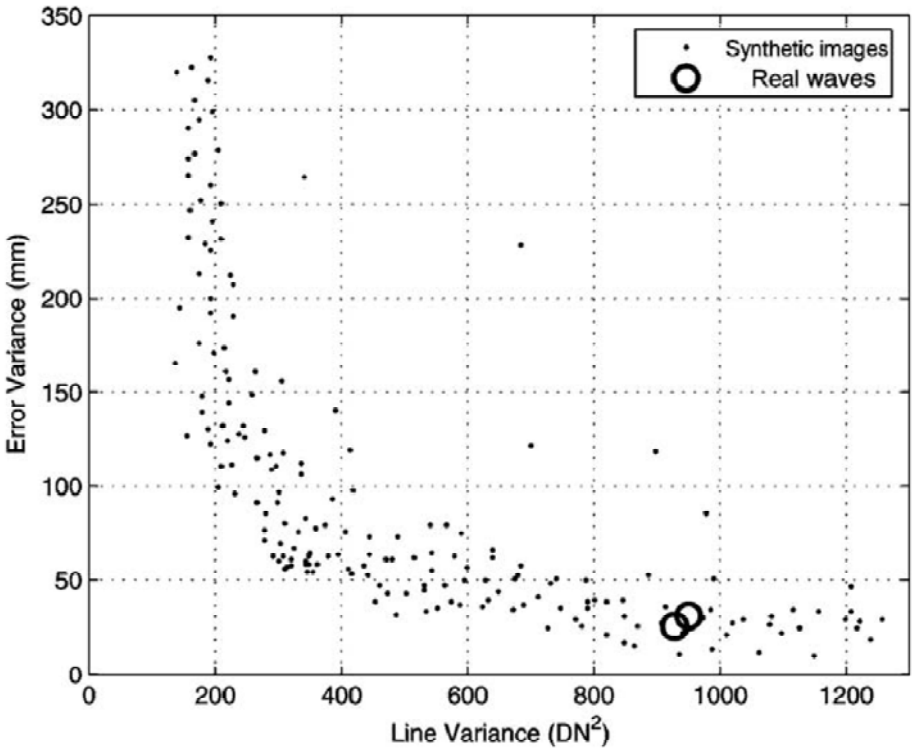

Figure 11 - Example of the error variance distribution experienced by synthetic images and images of real water surface waves. The horizontal axis of figure represents the epipolar line variance expressed in square Digital Number (DN), where the Digital number is the gray value representing the pixel brightness. In this example is used a 8 bit CCD, i.e. DN ranges between 0 and 255. For this example, the distribution of the error variance follows approximately a hyperbole.

2.4. WASS DEPLOYMENT AT THE OCEANOGRAPHIC TOWER '*ACQUA ALTA*' (VENICE)

2.4.1. Installation site

The '*Acqua Alta*' tower of the CNR-ISMAR Institute is located in the Northern Adriatic Sea, East of Italy, 16 km off the coastline of Venice, on 16 m of depth as shown in Figures 12-13. The tower was used as the calibration site for the ERS-1 radar altimeter. The tower is equipped with a tide gauge and various meteorological instruments that provided an independent set of measurements of the sea level which were compared against those measured by the radar altimeter.

Figure 12 - Installation site at '*Acqua Alta*' in the Northern Adriatic Sea, ITALY.

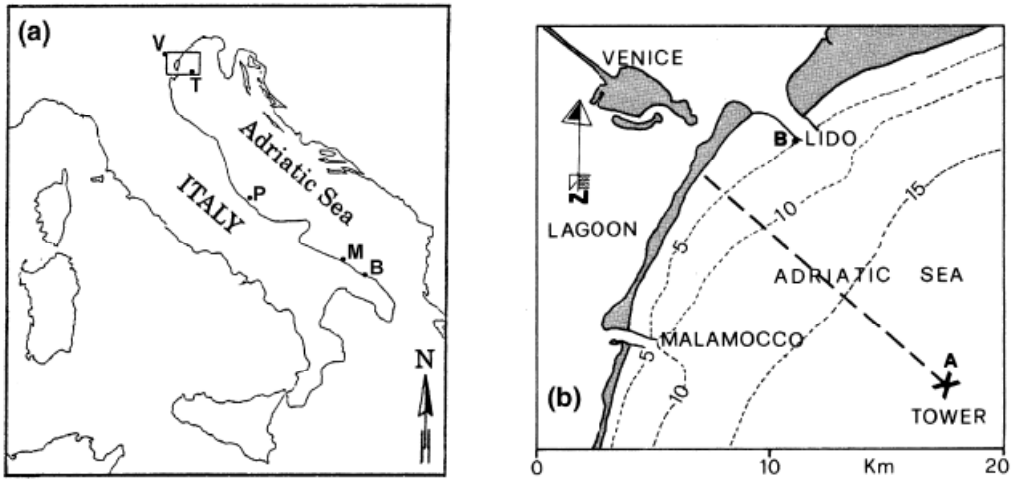

Figure 13 - (a). The Adriatic Sea. Its dimensions are about 700=200 km^2. V=Venice, T=tower, P=Pescara, M=Monopoli, B=Brindisi. The small rectangle marks the area enlarged in (b). The tower is about 15 km off the coast. The Lido, Malamocco and Chioggia inlets connect the Venice lagoon with the sea. Chioggia inlet is out of the map.

The tower was built in 1970. As shown in Figure 14 its basic structure is a four leg, framed template extending 4 m above the sea surface. The template is firmly fixed on the bottom, the poles penetrating 22 m inside the sediments. The housing structure (three floors plus the top terrace) is firmly joined to the upper end of the template. The submerged part is protected by zinc anodes. The splash zone (+3, -2 m) is covered with a fully protective layer of epoxy resin. The three floors are at 4.5, 6.7, 9.3 m above the mean sea level, respectively. The terrace floor is at 12.3 m. Starting from the second floor, a large platform extends horizontally 7 m in the southeast direction. Two smaller platforms protrude towards the southwest and northeast. The tower is equipped with 380, 220, 125 VAC 50 Hz, available when personnel are on board. A large set of batteries provides 12 and 24 VDC for occasional measurements and for some basic regular needs. At the tower internet connection is provided. The tower is not continuously manned. People move on board either for specific needs or for maintenance (if so, on a fortnight basis). The living quarters are on the third floor. They include a 5x5 m living room, a 1x2 m bath, a 2x3 m kitchen, and a 2x2 m room devoted to on board instruments. Cooking and sleeping facilities, taken care by devoted personnel, allow four persons on board for an unlimited period of time. The connection with the institute is by motor-boat with cabin and by pilot boat, both capable to stand stormy conditions. The travel time between the institute and the tower is 80 minutes.

The tower is also equipped with a meteo-oceanographic station. The data are recorded on board and also sent to land by telemeters. The station includes measurements of wind, temperature, humidity, solar radiation, rain, waves (directional), tides and sea temperature. The water level has been recorded since 1971. Two tide gauges of the conventional well type are installed. Wave gauges are also operational and consist of three pressure transducers located on three of the four platform legs at 5 m depth. Continuous recording is performed for 17 min every 3 h. The system, which allows an estimate of the directional wave spectrum, has, with appropriate upgrading, been in operation since 1978.

We have deployed **WASS** on the North-west side of the tower in order to have a camera field of view with respect to both the Scirocco and Bora wind sea states (Figure 15). Further, **WASS** has been installed at the third floor of the tower to maximize the stereo camera field view as shown in Figure 16 which reports a sketch of the stereo camera field perspective from the platform.

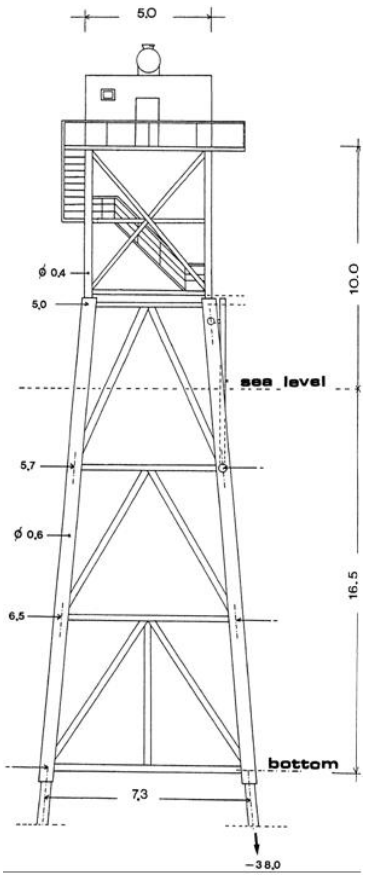

Figure 14 - '*Acqua Alta*' tower.

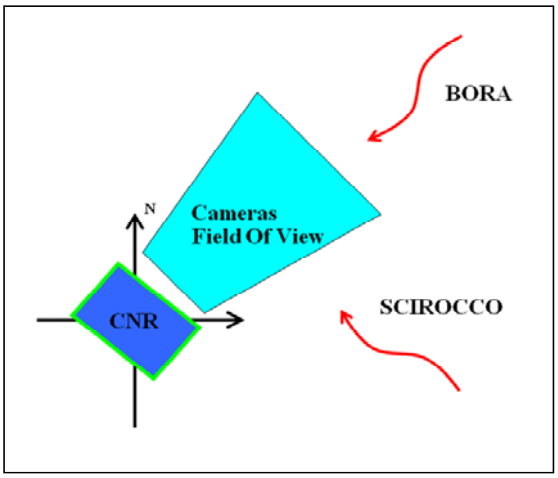

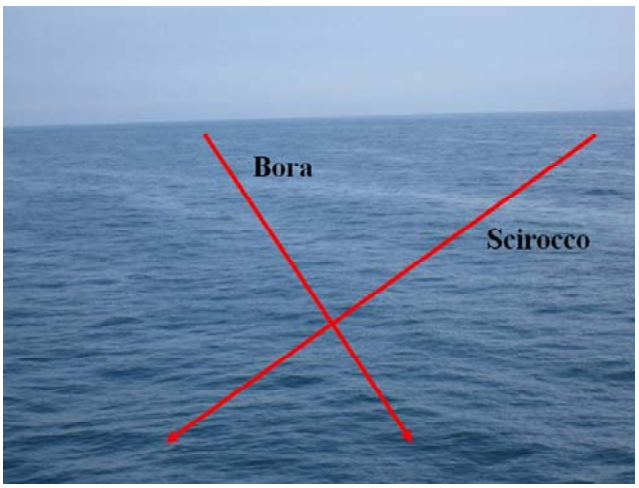

Figure 15 - Stereo camera field of view (left) and Camera view from the '*Acqua Alta*' platform (right) with respect to the Sirocco and Bora wind sea states.

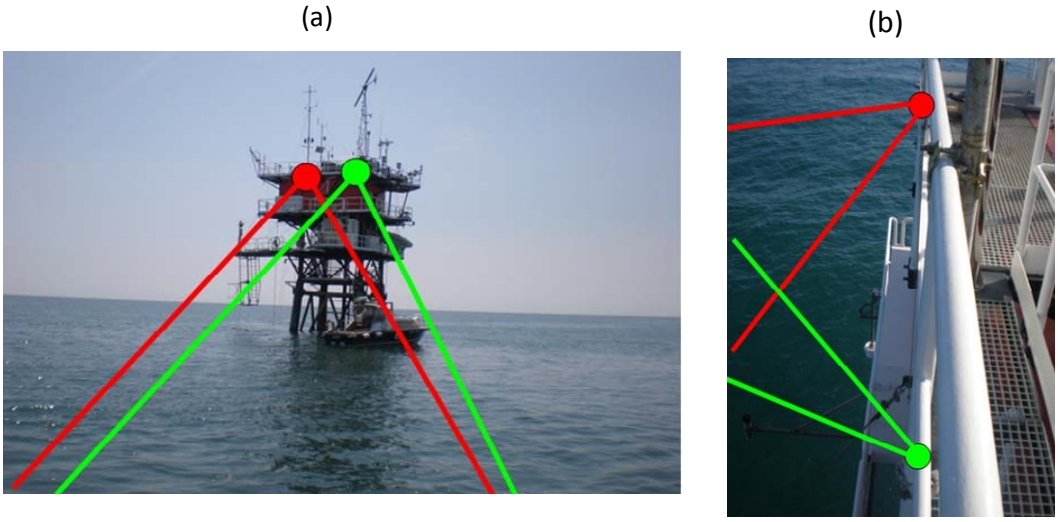

Figure 16 - (a) Sketch of the stereo camera field perspective and (b) view from the platform (red: right camera, green: left camera).

The Wave climate nearby the "*Acqua Alta*" area can be partially described through directional measurement available at "Punta della maistra" buoy (Figure 17), managed by the Italian Environmental Agency. It is dominated by Scirocco winds blowing from South-East with a Fetch of approximately 700 km as clearly seen in Figure 18. Note also that Bora winds (45° wave contribution) concur to generate high waves in the area.

Figure 17 - Northern Adriatic Sea: 'Acqua Alta' tower (T) and Punta della Maistra buoy (B) .

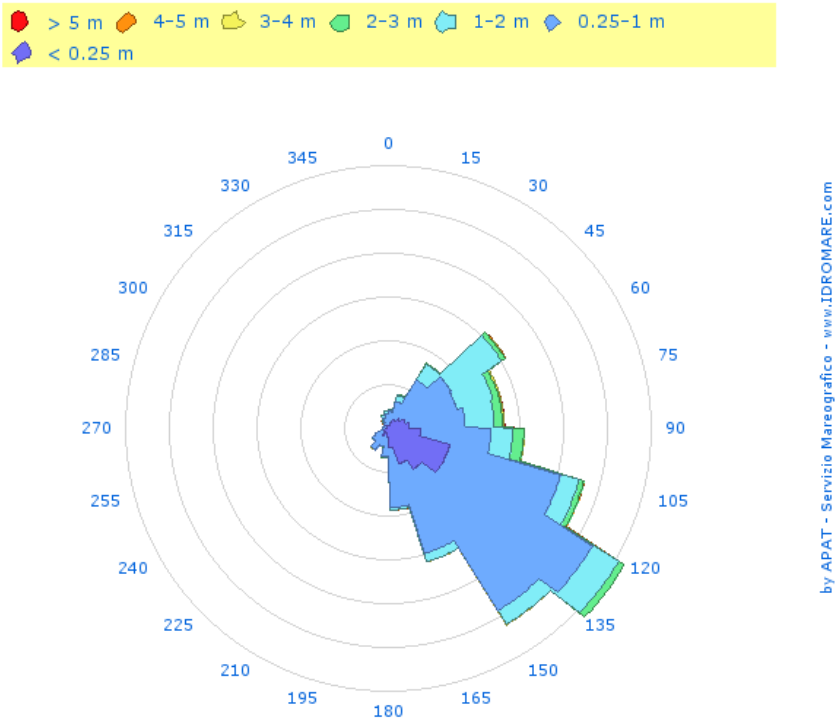

Figure 18 - Punta della Maistra wave climate. Period: 01-january-2004 (01:00 UTC+0) to 24-november-2004 (20:30 UTC+0).

2.4.2. WASS hardware specifications

WASS installed at '*Acqua Alta*' is mainly composed of

- A Couple of 5 Megapixel BM-500GE JAI (Figure 19) cameras with specifications
  - Sensor 2/3" progressive scan CCD (8 bit)
  - Pixel Clock 60 MHz
  - Frame rate full frame 15 frames/second
  - Active area 8.45 (h) x 7.07 (v)
  - Cell size 3.45 (h) x 3.45 (v)
  - Active pixels 2456 (h) x 2058 (v). Cell size = 3.45 µm x 3.45 µm
  - Read-out modes
  - GigE Vision interface with 12, 10 or 8-bit output

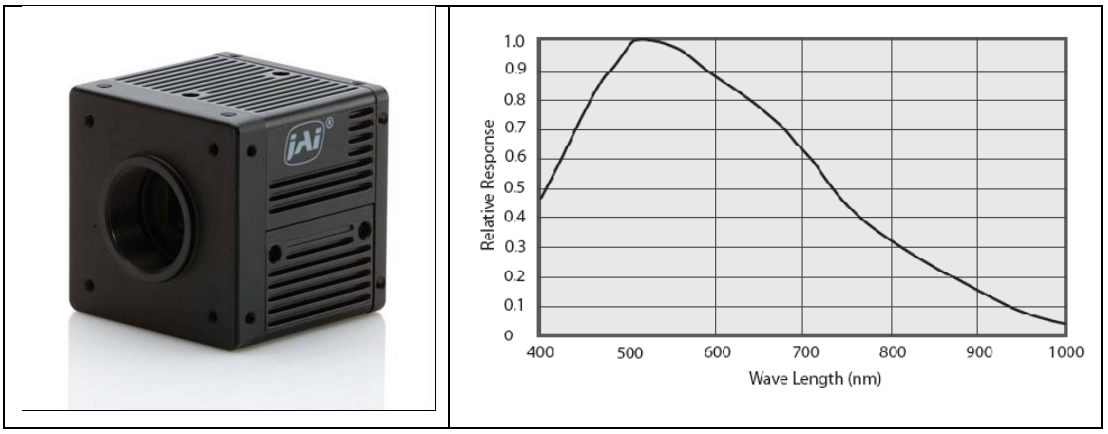

Figure 19 - JAI 5 Megapixel BM-500GE JAI camera. Right panel: Spectra Response of camera.

- 5-mm focal length low distortion lens (Figure 20)

Figure 20 – Low distortion lens.

- Trigger board: 5 fps, 6 fps, 10 fps, 15 fps selectable (Figure 21)

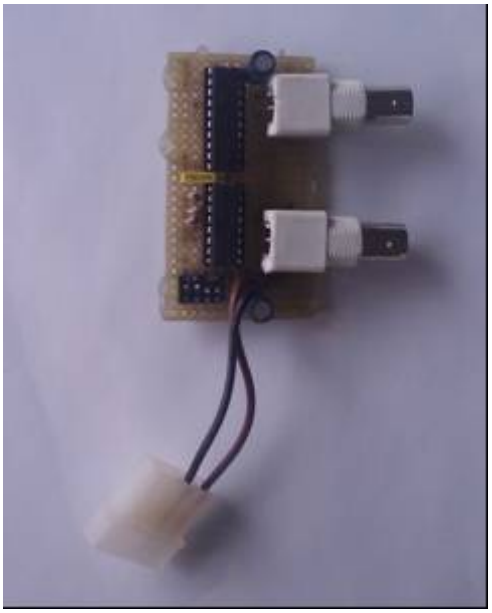

Figure 21 – Trigger board.

- Workstation and cables (Figure 22, Figure 23)

Figure 22 – Workstation and cables at '*Acqua Alta*'.

Figure 23 – (Top) JAI BM-500 GE camera with trigger and (Bottom) power cable (black) and GigaEthernet cable (blue) for data communication.

As the stereo system frames moving objects (i.e. waves) both the cameras must be synchronized, that is left and right cameras images must be framed approximately at the same instant of time. To impose synchronization on an electronic board we mounted a series of 10 LEDs in order to turn on them sequentially with an ignition delay of 1 ms apart. Stereo acquisition of the LEDs, triggered by an electronic device (trigger board), revealed that the system remained synchronous (the images of

the two cameras always see the same LED on) the all time during a continuous 24-hour testing (Figure 24).

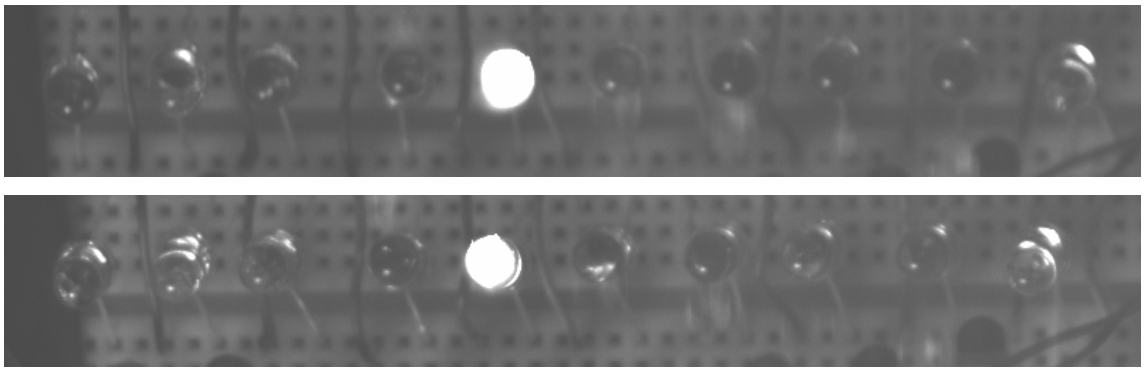

Figure 24 – Synchronization test. Upper panel shows image acquired at a certain time from left camera. Lower panel shows image acquired at a certain time from right camera. The images show the same led on.

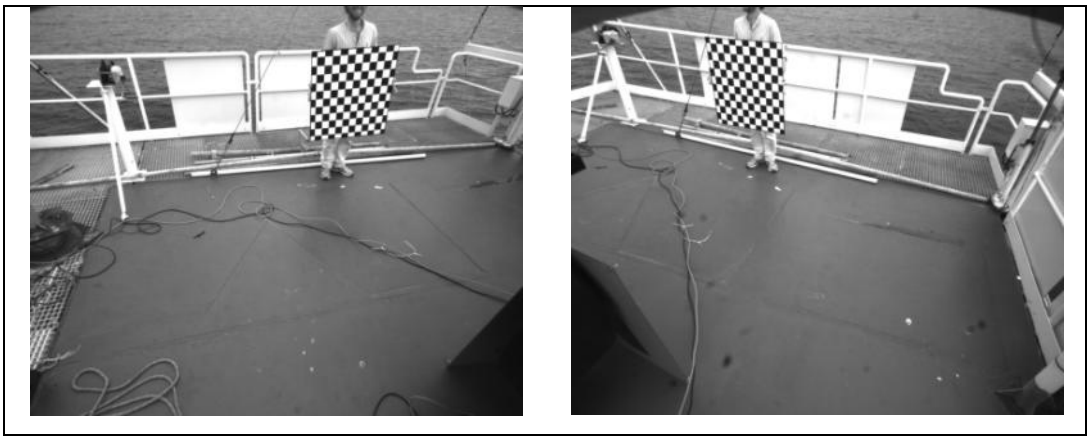

Figure 25 - Left panel: example of left camera image used for stereo calibration. Right panel: example of right camera image used for stereo calibration.

2.4.3. Stereo rig calibration

A stereo system must be calibrated in order to acquire some intrinsic characteristics of camera lens (internal camera parameters) and the reciprocal position between cameras (external stereo parameters). To do so, standard image analysis technique (Ma et al. 2004) exploits a given known reference (for example, a chess-board plane as shown in Figure 25) to estimate

1. *Internal parameters*
    a. Lens focal length;
    b. Principal point;
    c. Distortion, i.e. lens angular aberration (see Figure 26)

and

2. *External parameters* (see Figure 27)
    a. Rotation matrix (or rotation matrix following Rodrigues formulation as in Ma et al. 2004);
    b. Translation vector.

During field campaign at Acqua Alta, five calibration sessions were completed: two of these to measure internal parameters, and the other three sessions to estimate the external parameters. Results from these sessions are reported in Tables 2-8.

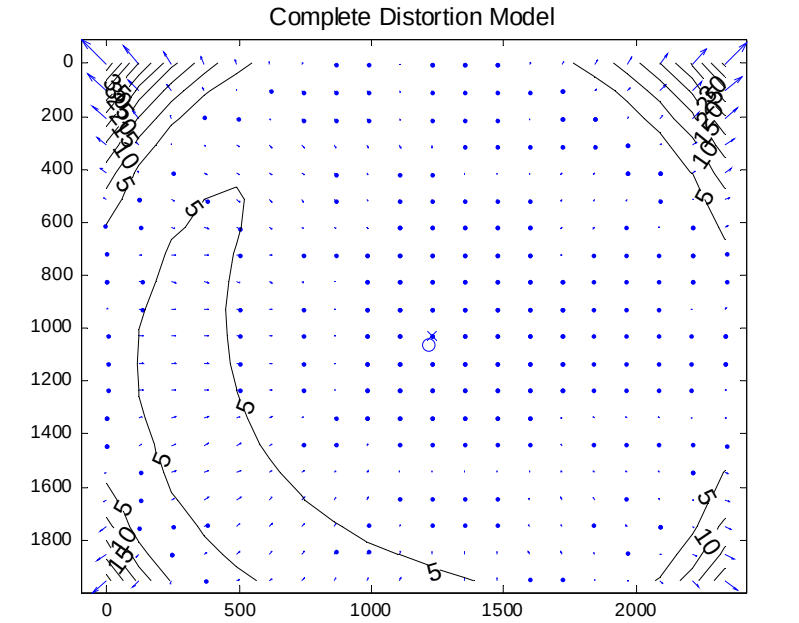

Figure 26 - Typical pixel error due to angular aberration of lens.

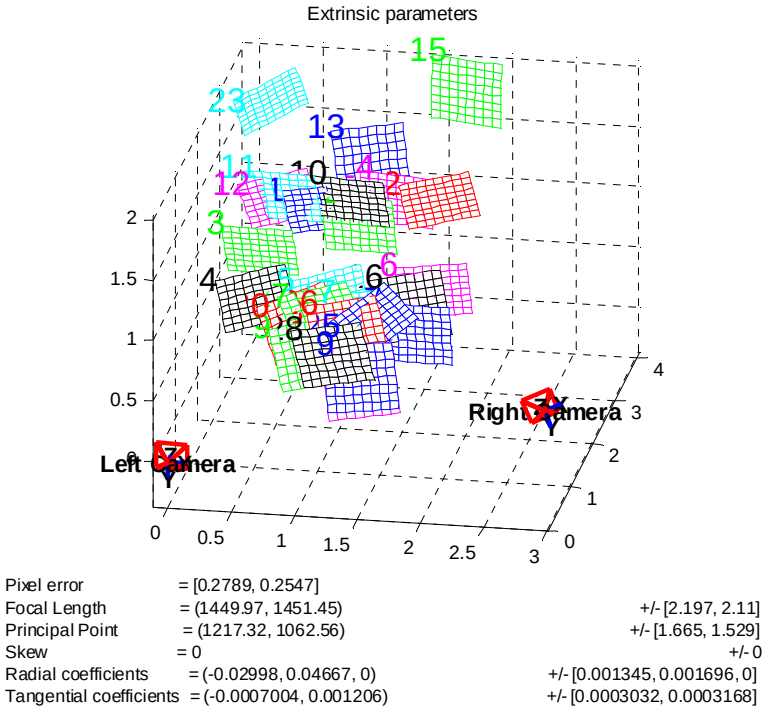

Figure 27 - Positions of target in left camera reference system used for extrinsic parameters calibration.

Focal Length:	fc = [1449.96894 1451.44925] ± [2.19693 2.10982] pixel
Principal point:	cc = [1217.31526 1062.55611] ± [1.66544 1.52933] pixel
Distortion:	kc = [-0.02998 0.04667 -0.00070 0.00121 0.00000] ± [0.00135 0.00170 0.00030 0.00032 0.00000]
Pixel error:	err = [0.27891 0.25472] pixel

Table 2 –Internal parameters. Session 1: 05 June 2009. Left camera.

Focal Length:	fc = [1446.14338 1448.12191] ± [1.47173 1.41854] pixel
Principal point:	cc = [1219.55662 1069.38976] ± [1.44445 1.32332] pixel
Distortion:	kc = [-0.04305 0.06810 -0.00043 -0.00012 0.00000] ± [0.00115 0.00169 0.00026 0.00029 0.00000]
Pixel error:	err = [0.26614 0.23369] pixel

Table 3 –Internal parameters. Session 1: 05 June 2009. Right camera.

Focal Length:	fc = [1454.85655 1456.68424] ± [1.57676 1.59637] pixel
Principal point:	cc = [1219.43339 1061.19205] ± [1.36561 1.51188] pixel
Distortion:	kc = [-0.04020 0.06626 -0.00082 -0.00075 0.00000] ± [0.00155 0.00268 0.00028 0.00027 0.00000]
Pixel error:	err = [0.30082 0.29708] pixel

Table 4 –Internal parameters. Session 2: 14 January 2010. Left camera.

Focal Length:	fc = [1453.62650 1455.11406] ± [1.72342 1.71283] pixel
Principal point:	cc = [1206.33308 1068.62332] ± [1.56173 1.62724] pixel
Distortion:	kc = [-0.03520 0.06117 -0.00057 0.00008 0.00000] ± [0.00143 0.00251 0.00029 0.00030 0.00000]
Pixel error:	err = [0.33688 0.29345] pixel

Table 5 –Internal parameters. Session 2: 14 January 2010. Right camera.

Rotation vector:	om = [0.00188 0.40390 0.37816] ± [0.00144 0.00284 0.00086]
Translation vector:	T = [-2.8110 -0.69220 0.6453] ± [0.0021 0.0014 0.0055] m

Table 6 –External parameters. Session 1: 06 June 2009.

Rotation vector:	om = [-0.08445 0.28549 0.24875] ± [0.00059 0.00138 0.00024]
Translation vector:	T = [-2.9581 -0.3480 0.3609] ± [0.0010 0.0004 0.00306] m

Table 7 –External parameters. Session 2: 03 September 2009.

Rotation vector:	om = [0.03504 0.27344 0.07547] ± [0.00097 0.00218 0.00051]
Translation vector:	T = [-2.4844 -0.1364 0.24202] ± [1.5576 0.7244 3.4562] m

Table 8 –External parameters. Session 3: 14 January 2010.

3. 3D WAVE MEASURMENTS AT "*ACQUA ALTA*" PLATFORM (VENICE, ITALY)

3.1. VALIDATION OF STEREO MEASUREMENTS

The video data were collected by **WASS** during three field campaigns at the "*Acqua Alta*" oceanographic platform in 2009-2010. The wave climate conditions during the three experiments are shown in Table 9. In the same Table, we also report distance (base) between principal points of the two cameras, number of frames and acquisition rate as well as the horizontal resolution (res) of the reconstructed 2-D sea maps.

Exp #	Starting date and hour	Wind Speed [m/s, dir from]	# frames	frame rate [fps]	Base [m]	Res [m]
1	2009/06/05 1428 UTC	6.5, 133.0 (±11.3)°N	6000	10	~ 3.0	0.05
2	2009/10/14 0755 UTC	6.3, 90.0 (±11.3)°N	21000	10	~ 3.0	0.05
3	2010/03/09 1120 UTC	17.9, 67.5 (±11.3)°N	9000	5	~ 2.5	0.05

Table 9 – Experiments at Acqua Alta: duration, wind speed, reconstructed number of frames and correspondent frame rate, base distance between cameras and horizontal resolution (Res) of the reconstructed 2-D maps.

The three experiments cover a broad range of wave height conditions and steepness ε as shown in Table 10. Here, T_p is the peak wave period, ε is defined as the ratio between the significant wave height H_s and the average wavelength L_{mean} estimated from the average zero-crossing period T_z via the linear dispersion (water depth d=16 m).

Exp #	Date	H_s [m]	T_p [s]	T_z [s]	L_{mean} [m]	ε
1	2009/06/05	0.46	4.34	3.09	14.9	0.03
2	2009/10/14	1.10	4.83	3.62	20.5	0.05
3	2010/03/09	2.16	6.36	4.85	36.5	0.06

Table 10 – Wave conditions during the three experiments at Acqua Alta. H_s=Significant wave height, T_p=peak wave period, T_z=zero up-crossing period, L_{mean}=mean wave length and ε=steepness.

Experiment 3, with a much higher wind speed, exhibited the largest H_s / L_{mean} ratio among the three wave fields and the acquired videos confirmed the occurrence of wide spread breaking. To illustrate some stereo results, Figure 28 shows an example of a reconstructed 2D sea surface map from experiment 2.

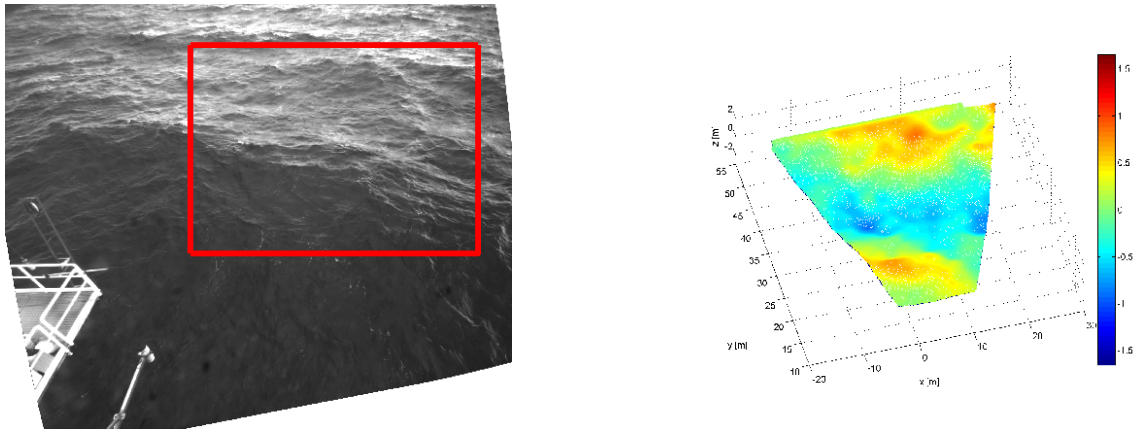

Figure 28 – (Left panel) Image of sea surface taken during Experiment 2 and selected area for stereo reconstruction (50 m x 50 m); (Right panel) correspondent reconstructed sea surface topography.

Wave data calculated by using **WASS** stereo analysis were compared against reference point time series measurements provided by instruments available at "*Acqua Alta*": wired wave gauges and AWAC ADCP. Such comparison was performed by first selecting a virtual point probe within the reconstructed area and then extracting the associated time series of the stereo reconstructed wave surface displacements (see set of Figures 29-30 and 31-32 for experiments 2 and 3, respectively). Given the wave time series, various statistical and spectral properties of waves were computed and compared against those obtained from *Acqua Alta* instruments. Tables 11, 12 and 13 report such comparisons for experiments 1,2 and 3 respectively. Here, spectral spreading and mean wavelengths for **WASS** data are estimated from the 3D measurements via the 2-D wavenumber spectrum. The peak wavelength L_{peak} and period T_{peak} are relative to the spectral peak of the 1D wavelength spectrum. Estimates of the significant wave heights H_{mo}, $H_{1/3}$ and $H_{1/10}$, and wave periods T_m and T_z follow from a zero-crossing analysis of the extracted time series low-pass filtered at roughly 2.0 Hz. The largest wave surface height estimated during the experiments is denoted with H_{max}. The directional distributions of the observed wave spectrum at the peak wavenumber and their cubic interpolation are shown in Figures 33, 34 and 35 for experiments 1, 2 and 3 respectively. Note that Acqua Alta directional measurements were not available during experiment 1. Such comparisons clearly prove that the accuracy stereo measurements via **WASS** is comparable to that of more traditional wave instruments.

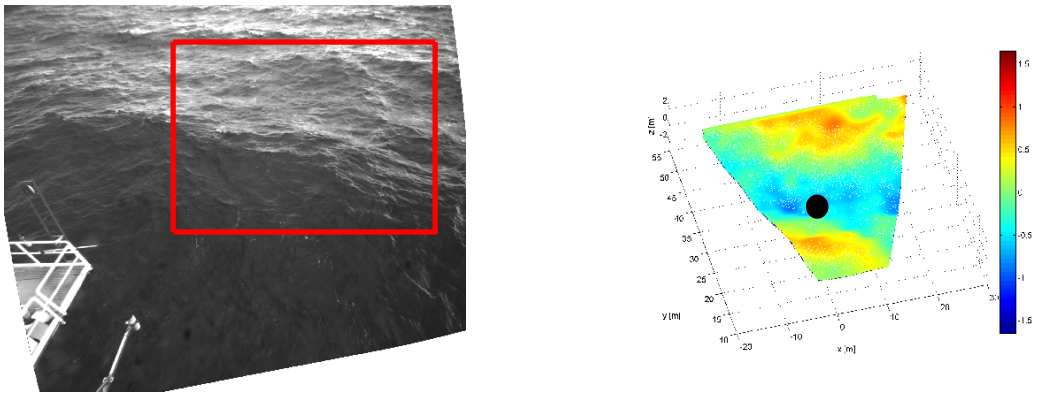

Figure 29 - Time series extraction from 3D data from experiment 2: black dot denotes virtual point probe.

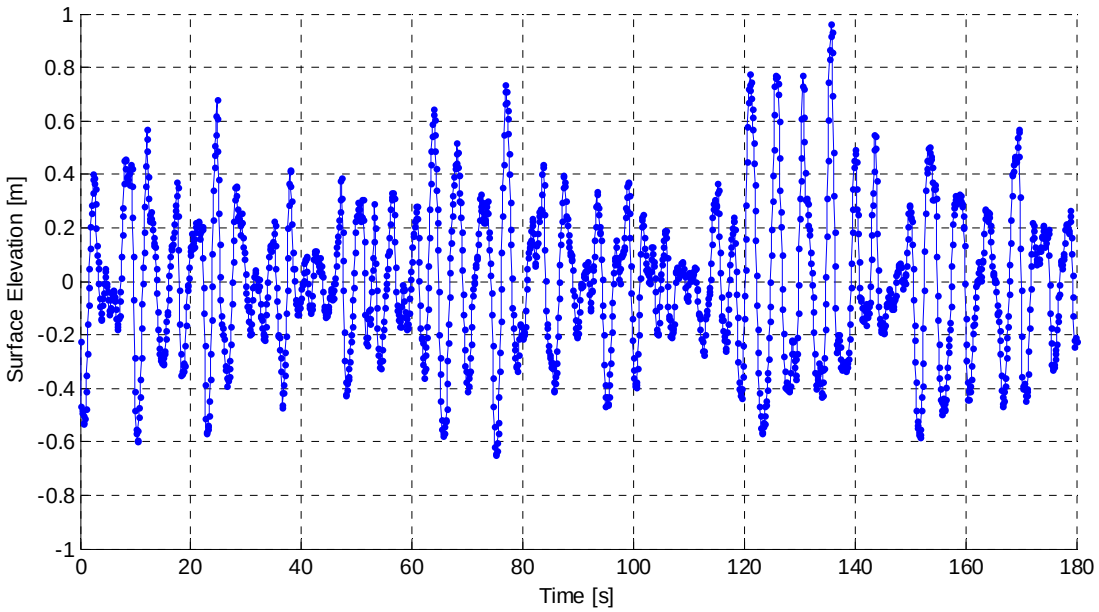

Figure 30 - Water elevation time series extracted from virtual point probe in Figure 29 (Experiment 2).

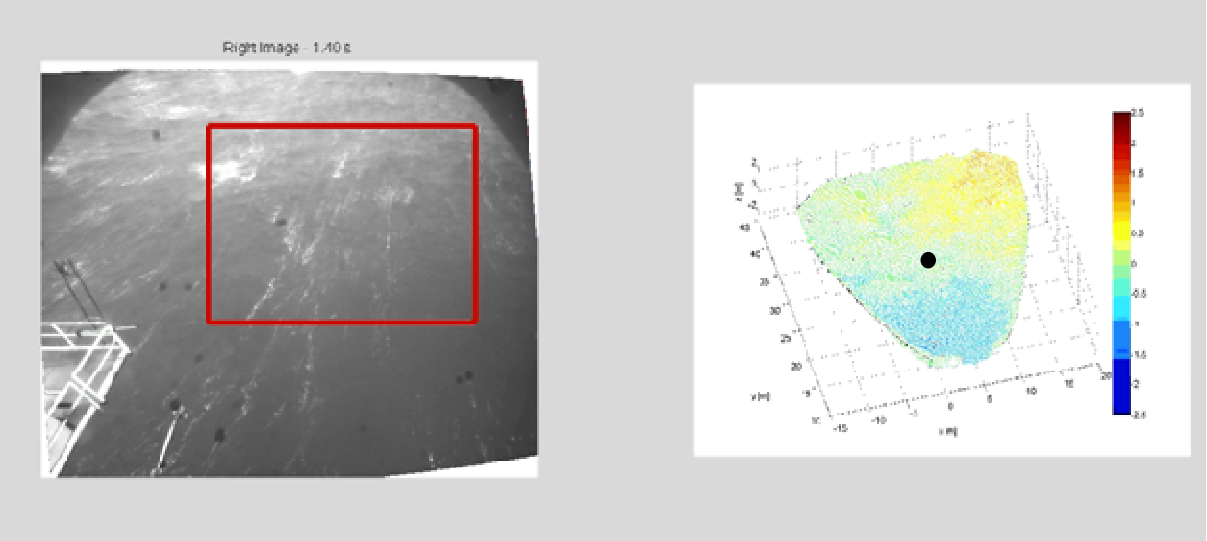

Figure 31 - Time series extraction from 3D data from experiment 3: black dot denotes virtual point probe.

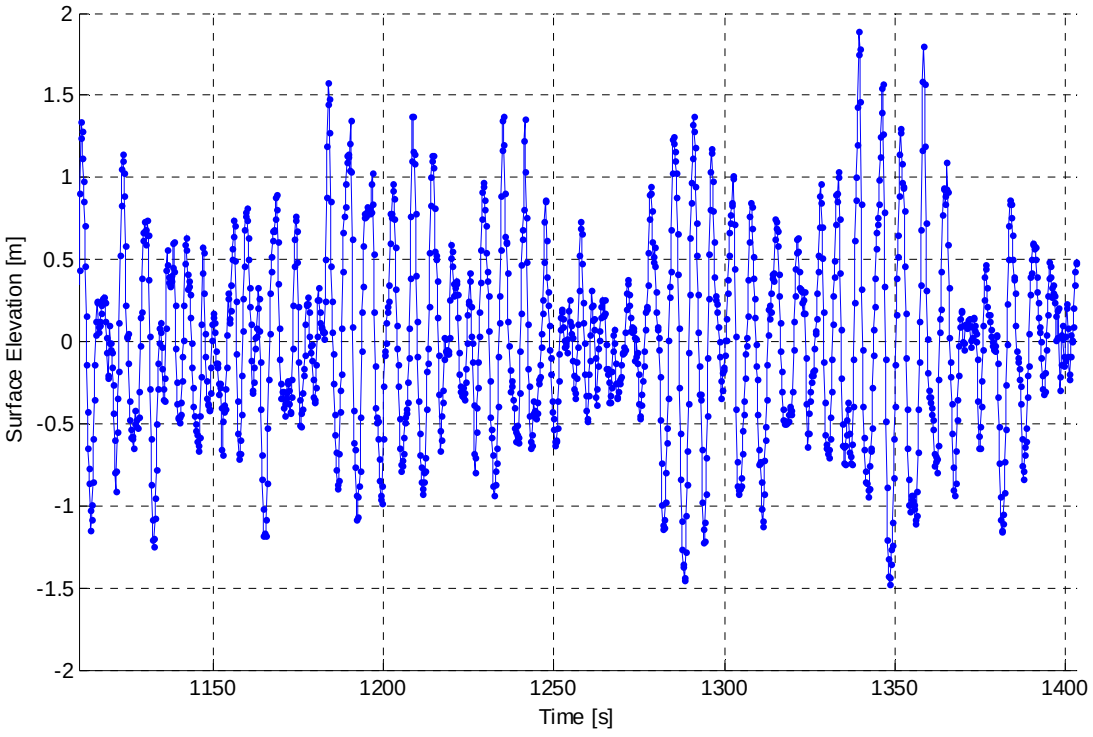

Figure 32 - Water elevation time series extracted from virtual point probe in Figure 31 (Experiment 3).

start Date (UTC)	end Date (UTC)	
05/06/2009 14.30	05/06/2009 14.45	**CNR**
05/06/2009 14.28	05/06/2009 14.38	**WASS**

Hm0 [m]	H 1/3 [m]	H1/10 [m]	Hmax [m]
-	**0.47***	-	**0.68***
0.41	**0.46**	**0.60**	**0.83**

start Date (UTC)	end Date (UTC)	
05/06/2009 14.30	05/06/2009 14.45	**CNR**
05/06/2009 14.28	05/06/2009 14.38	**WASS**

Tp [s]	Tz [s]	T max [s]
-	**3.92 ***	**5.29 ***
4.34	**3.09**	**5.40**

* CNR instrument partially influenced by platform piles

Table 11 – Experiment 1: comparison of WASS/*Acqua-Alta* measurements.

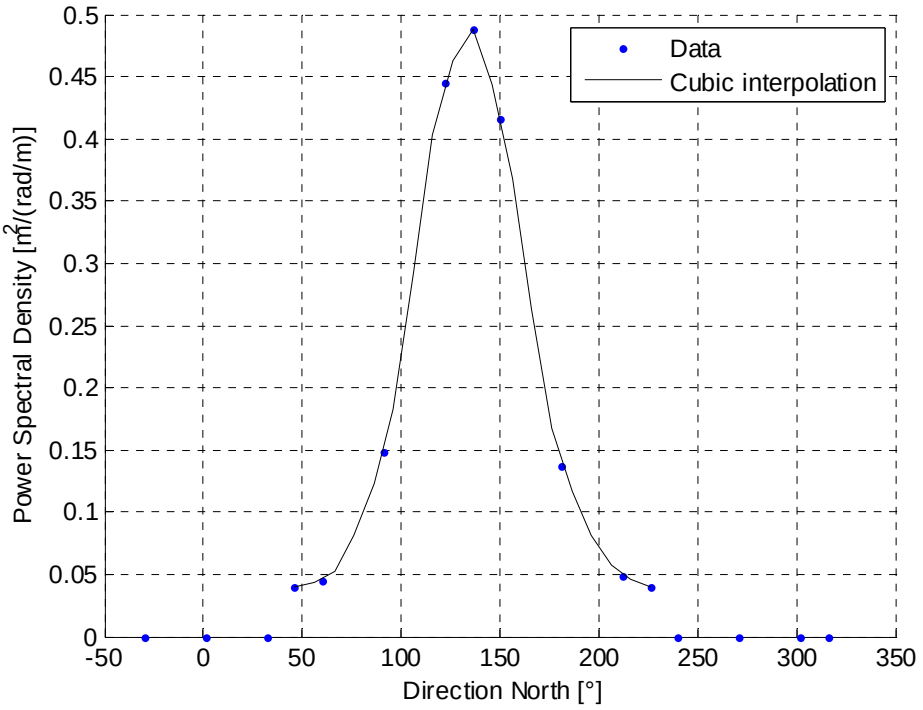

Figure 33 – Experiment 1: WASS directional distribution of the spectral intensities at peak wavenumber and the associated cubic interpolation.

\

start Date (UTC)	end Date (UTC)		Hm0 [m]	H 1/3 [m]	H1/10 [m]	Hmax [m]
14/10/2009 8.00	14/10/2009 8.30	**CNR**	**1.13**	**1.09**	**1.36**	**2.18**
14/10/2009 7.55	14/10/2009 8.30	**WASS**	**1.15**	**1.10**	**1.34**	**2.03**

start Date (UTC)	end Date (UTC)		Tp [s]	Tz [s]	T max [s]
14/10/2009 8.00	14/10/2009 8.30	**CNR**	**4.59**	**3.51**	**6.00**
14/10/2009 7.55	14/10/2009 8.30	**WASS**	**4.83**	**3.62**	**6.40**

start Date (UTC)	end Date (UTC)		L peak **[m]	T from L peak [s]	L mean ***[m]	T from L mean [s]
14/10/2009 8.00	14/10/2009 8.30	**CNR**	-	-	-	-
14/10/2009 7.55	14/10/2009 8.30	**WASS**	**33.7**	**4.66**	**22.3**	**3.77**

** estimated from 1D wavenumner spectrum (21000 3D maps)
*** estimated from 2D wavenumner spectrum (21000 3D maps)
Note: T from L is calculated by exploting linear dispersion relationship

start Date (UTC)	end Date (UTC)		Peak dir [°]	Spreading [°]	Mean dir [°]
14/10/2009 8.00	14/10/2009 8.30	**CNR**	**60.3 ± 2**	**33.2**	**65 ± 2**
14/10/2009 7.55	14/10/2009 8.30	**WASS**	**64.6** *	See Figure	**59.5***

* uncertainity in platform orientation = 2°

Table 12 - Experiment 2: comparison of WASS/*Acqua-Alta* AWAC measurements Direction dir in [°] with respect to the geographical North.

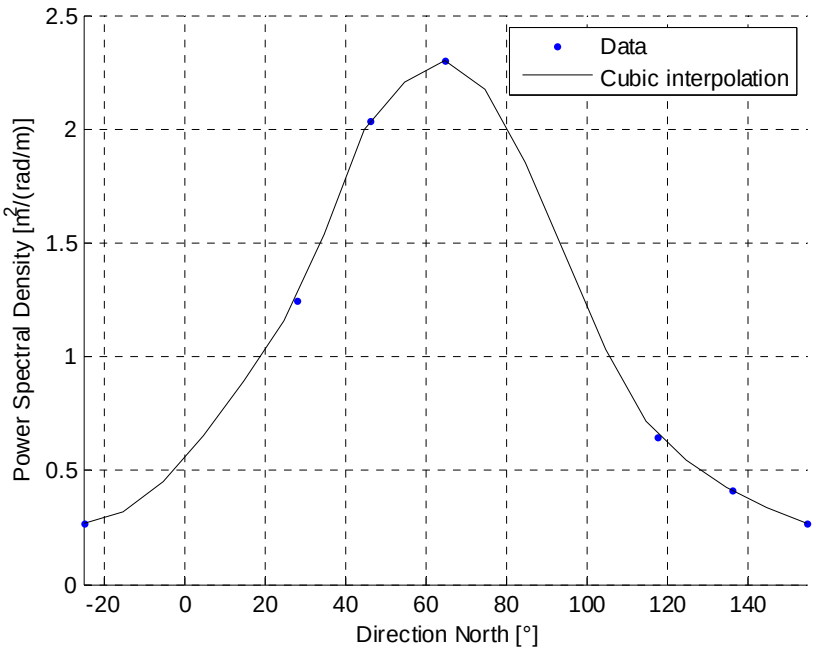

Figure 34 - Experiment 2: WASS directional distribution of the spectral intensities at peak wavenumber and associated cubic interpolation.

start Date (UTC)	end Date (UTC)		Hm0 [m]	H 1/3 [m]	H1/10 [m]	Hmax [m]
09/03/2010 11.28	09/03/2010 11.58	**CNR**	**2.23**	**2.16**	**2.79**	**3.80**
09/03/2010 11.20	09/03/2010 11.50	**WASS**	**2.17**	**2.16**	**2.64**	**3.95**

start Date (UTC)	end Date (UTC)		Tp [s]	Tz [s]	T max [s]
09/03/2010 11.28	09/03/2010 11.58	**CNR**	**6.37**	**4.62**	**8.50**
09/03/2010 11.20	09/03/2010 11.50	**WASS**	**6.36**	**4.85**	**8.20**

start Date (UTC)	end Date (UTC)		Peak dir [°]	Spreading [°]	Mean dir [°]
09/03/2010 11.28	09/03/2010 11.58	**CNR**	**74.4±2**	**33.0**	**69.7±2**
09/03/2010 11.20	09/03/2010 11.50	**WASS**	**67.7***	See Figure	**70.1***

* uncertainity in platform orientation = 2°

Table 13 – Experiment 3: comparison of WASS/*Acqua-Alta* AWAC measurements Direction dir in [°] with respect to the geographical North.

.

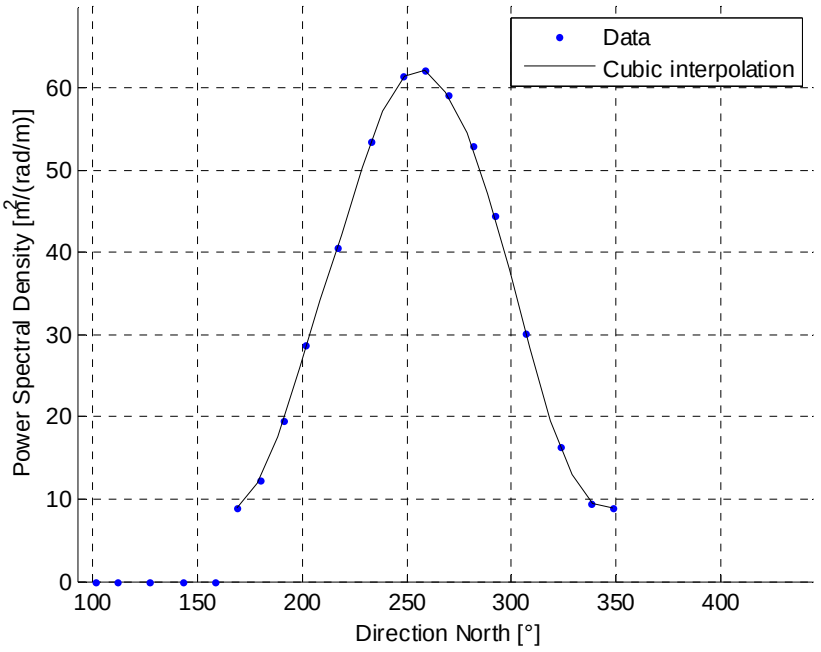

Figure 35 – Experiment 3: WASS directional distribution of the spectral intensities at peak wavenumber and the associated cubic interpolation.

3.2. EXPERIMENT 1: 2009 JUNE 05, 1428 UTC ÷ 1438 UTC

3.2.1. Stereo cameras setup and 3D reconstruction

A sketch of **WASS** left and right camera field of view is shown in Figure 36 and an example of stereo pairs (snapshots of the water surface at the same instant of time) is shown in Figure 37. Figure 38 shows various images framed by the right camera that provide an idea of the wave conditions during experiment 1. An example of stereo correspondences (i.e. corresponding pixels in left and right cameras of the same point in the world reference system) are shown in Figures 39-40. Here, both the images are corrected for lens aberration and also stereo rectified. Since the imaging set up is discrete in nature, the image coordinates of each pixel can be assumed to suffer from quantization errors of up to ± 1/2 pixel for each camera. The quantization error distribution of the final 3-D points in the x, y and z directions after stereo triangulation and the associated exceedance probability of its absolute value are shown in Figure 41. Because of quantization error, 3-D coordinates are biased. These errors can be reduced by applying subpixeling detection techniques (see Figure 42). Figure 43 shows the reconstructed 3D points in the left camera reference system, obtained after triangulation of stereo pairs (corresponding pixels in left and right cameras images), and Figure 44 grids the same 3D points in the world reference system. Successive snapshots of the 3D reconstruction of the water surface in time are shown in Figure 45, and Figure 46 reports time series of the wave displacements extracted at given virtual point probes. Finally, Figure 47 shows the variability of the significant wave height at Acqua Alta during experiment 1.

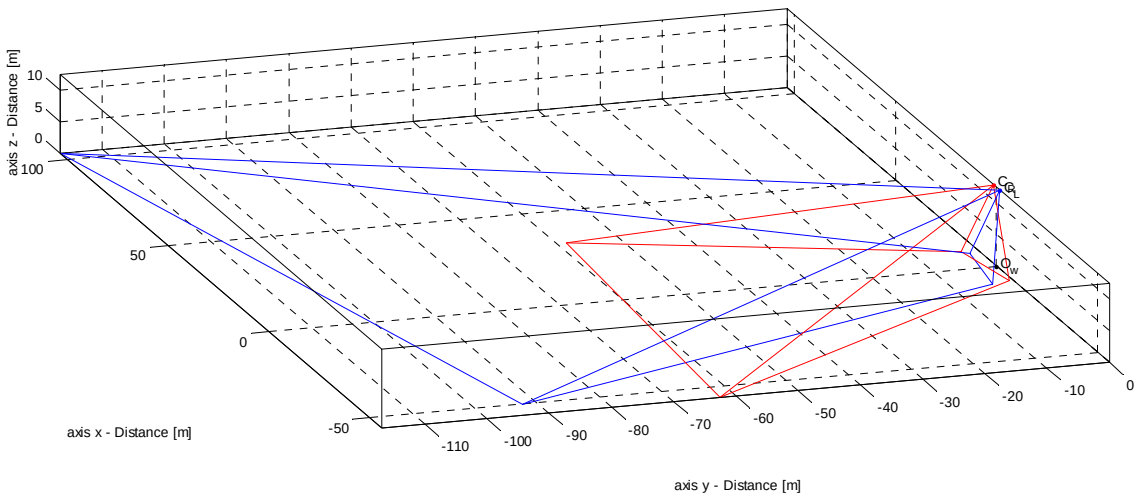

Figure 36 - Sketch of WASS installation for Experiment 1 in june 05, 2009. Fields of View of Left (blue lines) and right (red lines) cameras. Cameras are positioned at approximately 12.5 m above the mean sea level (z = 0).

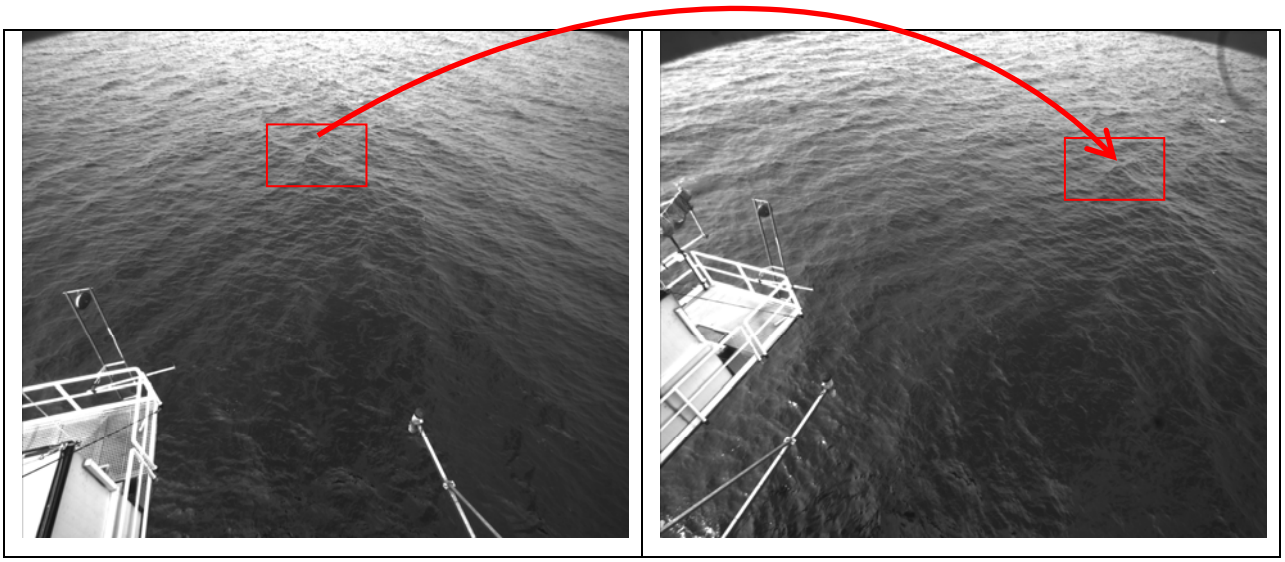

Figure 37 – Experiment 1: example of stereo pair snapshots, left and right camera images before lens aberration correction and stereo rectification. Arrows points at corresponding sea points in the two frames.

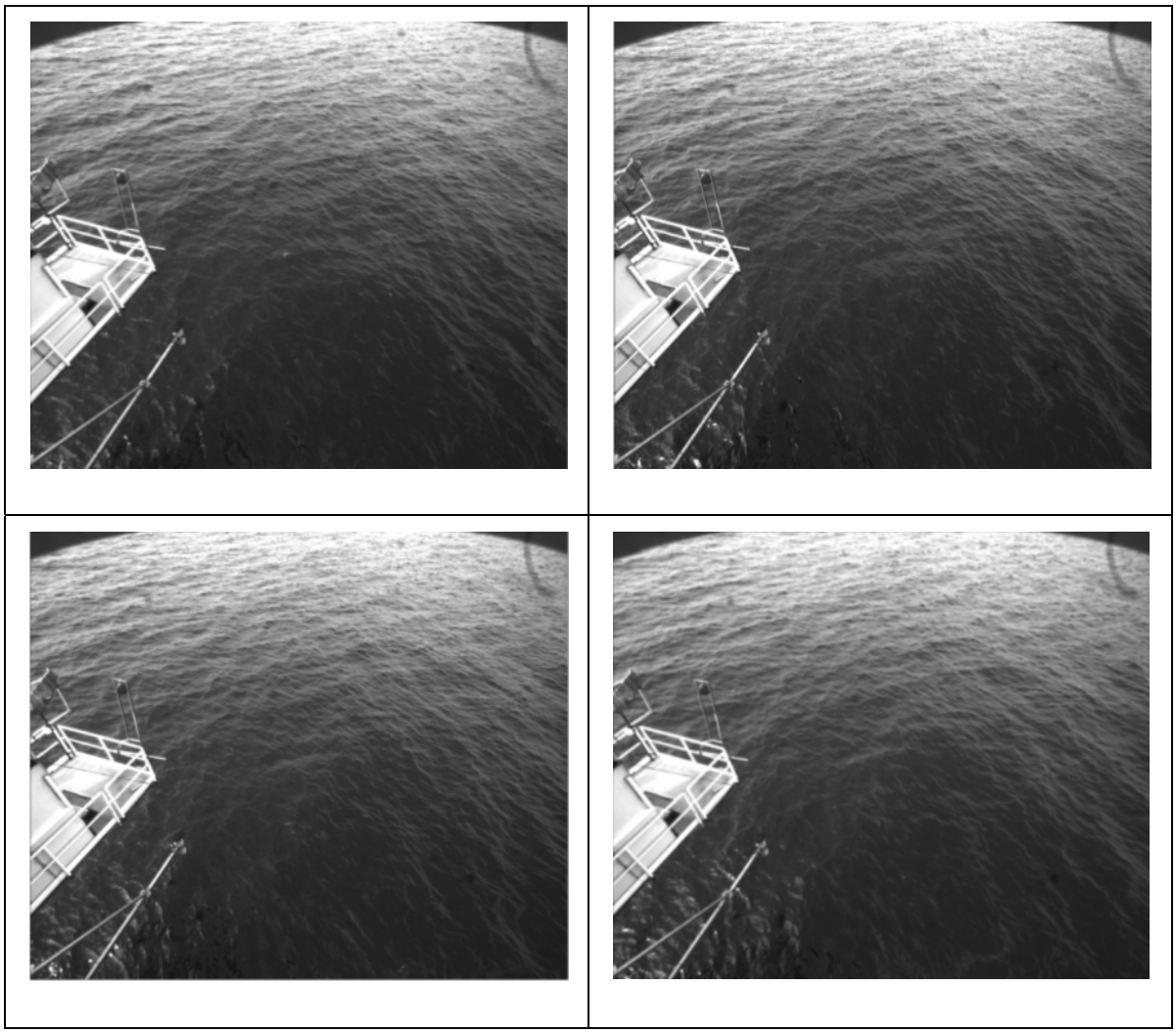

Figure 38 – Experiment 1: example of images framed by right camera during 2009, June 05 Experiment.

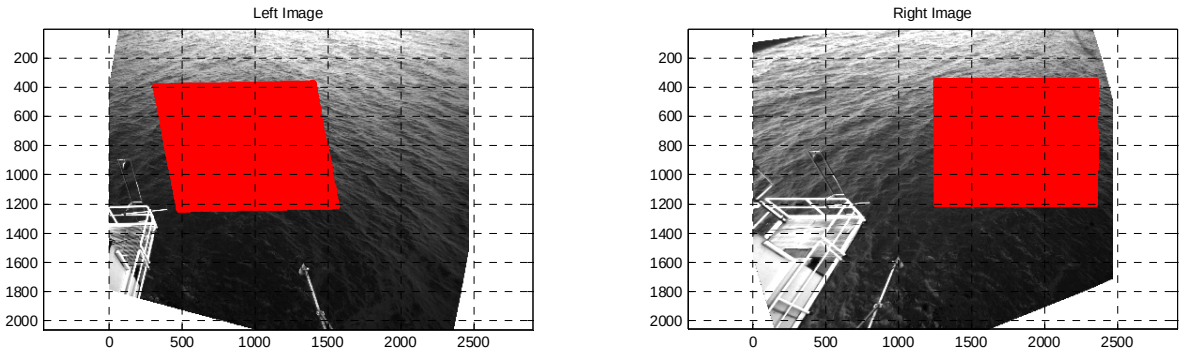

Figure 39 – Experiment 1: example of stereo correspondences. Red points in Left and Right images are corresponding points of the same sea surface pixel. Images are corrected for lens aberration and stereo rectified.

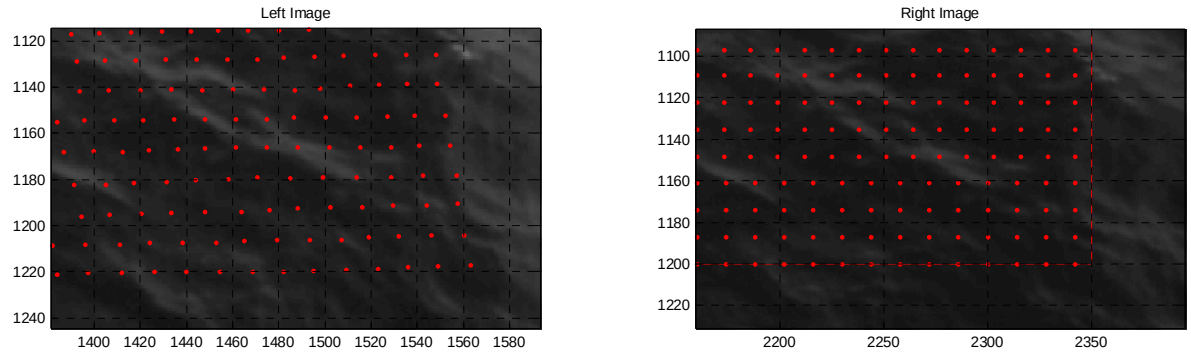

Figure 40 – Experiment 1: example of stereo correspondences. Red points in Left and Right images are corresponding points of the same sea surface 3D point.

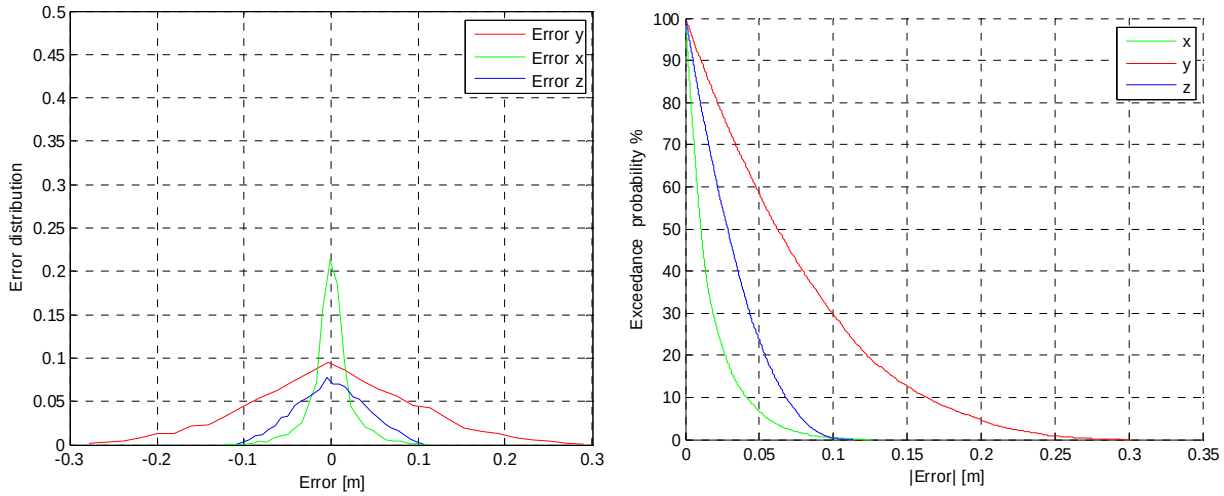

Figure 41 – Experiment 1: (Left) distribution of quantization errors and (Right) exceedance probability of their absolute values along the x,y, and z axes. Errors refer to pixel-to-pixel triangulation of red pixels of Figure 39 without any subpixel detection. (x,y,z axes as in Figure 36).

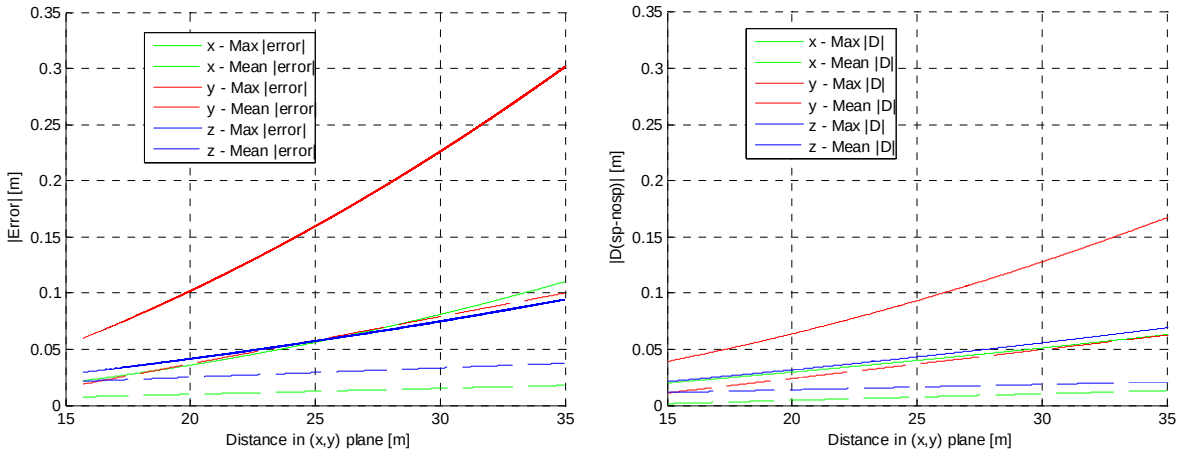

Figure 42 – Experiment 1: (Left) Max and mean absolute quantization errors as function of the horizontal distance from the cameras after stereo triangulation and (Right) after subpixel correction.

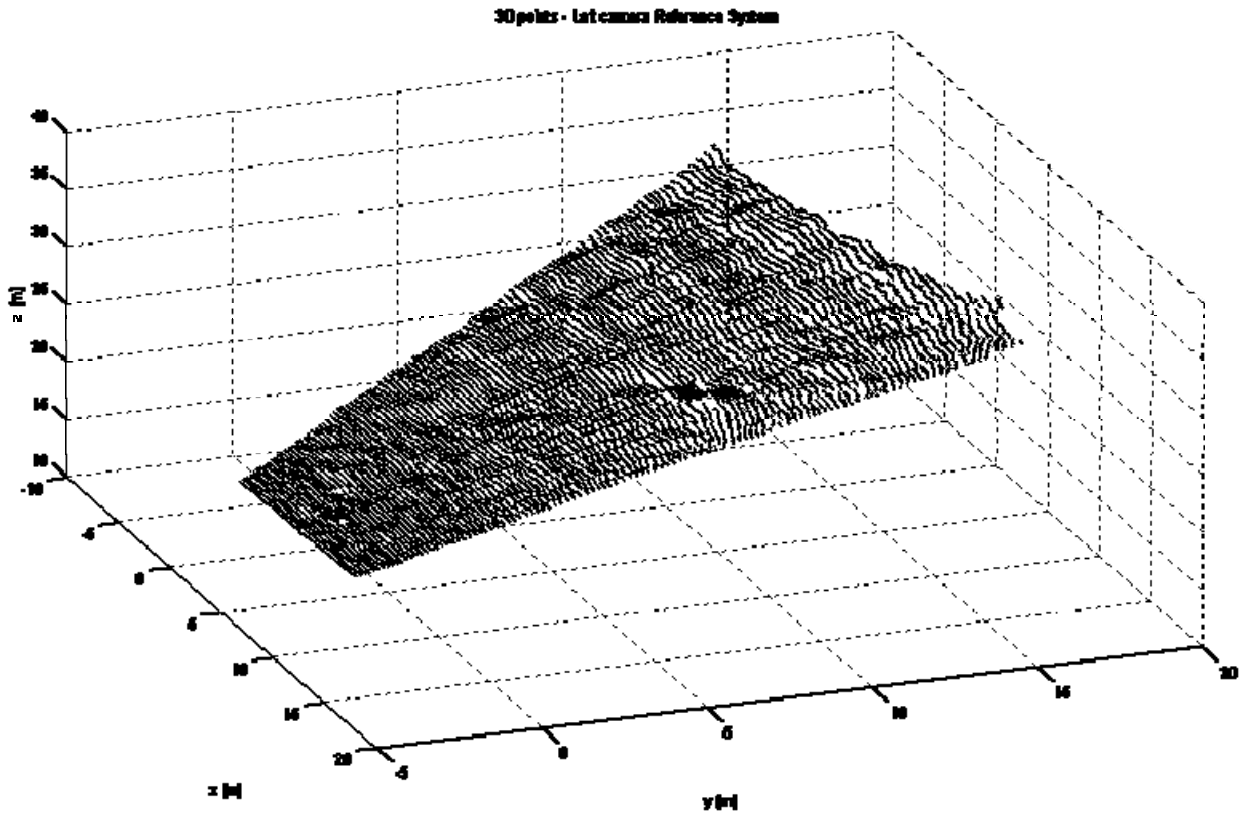

Figure 41 - Experiment 1: 3D points in Left camera reference system. Z is the distance of each 3D point from the CCD principal point.

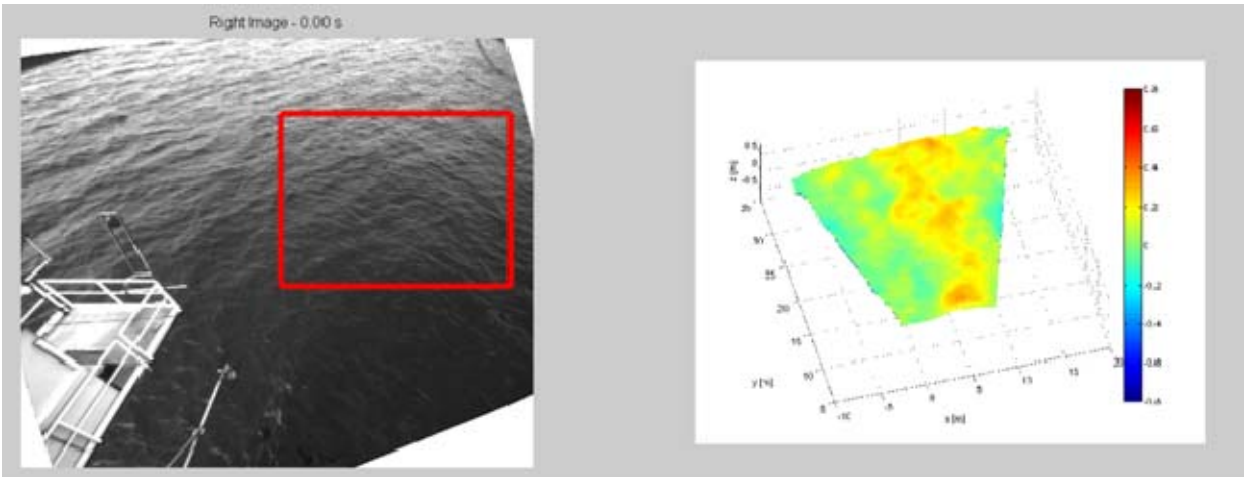

Figure 42 - Experiment 1: (Right panel) 3D points gridded in the world reference system where (x,y) plane is orthogonal to gravity direction z, and (Left Panel) recosntructed area.

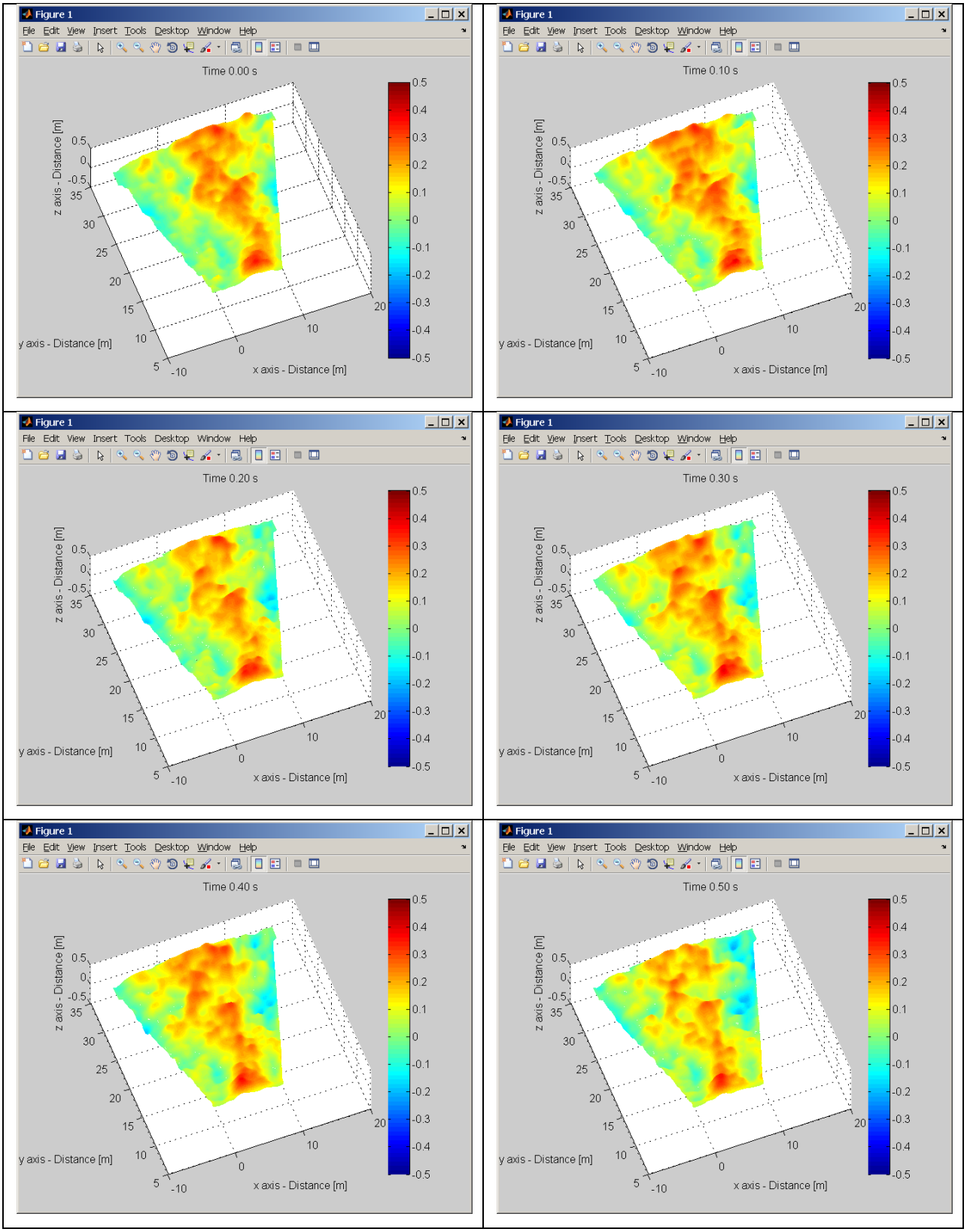

Figure 43 – Experiment 1: example of 3D reconstruction of the water surface shape in time. Time distance between consecutive images (from left to right, from top to bottom) is 0.1 s.

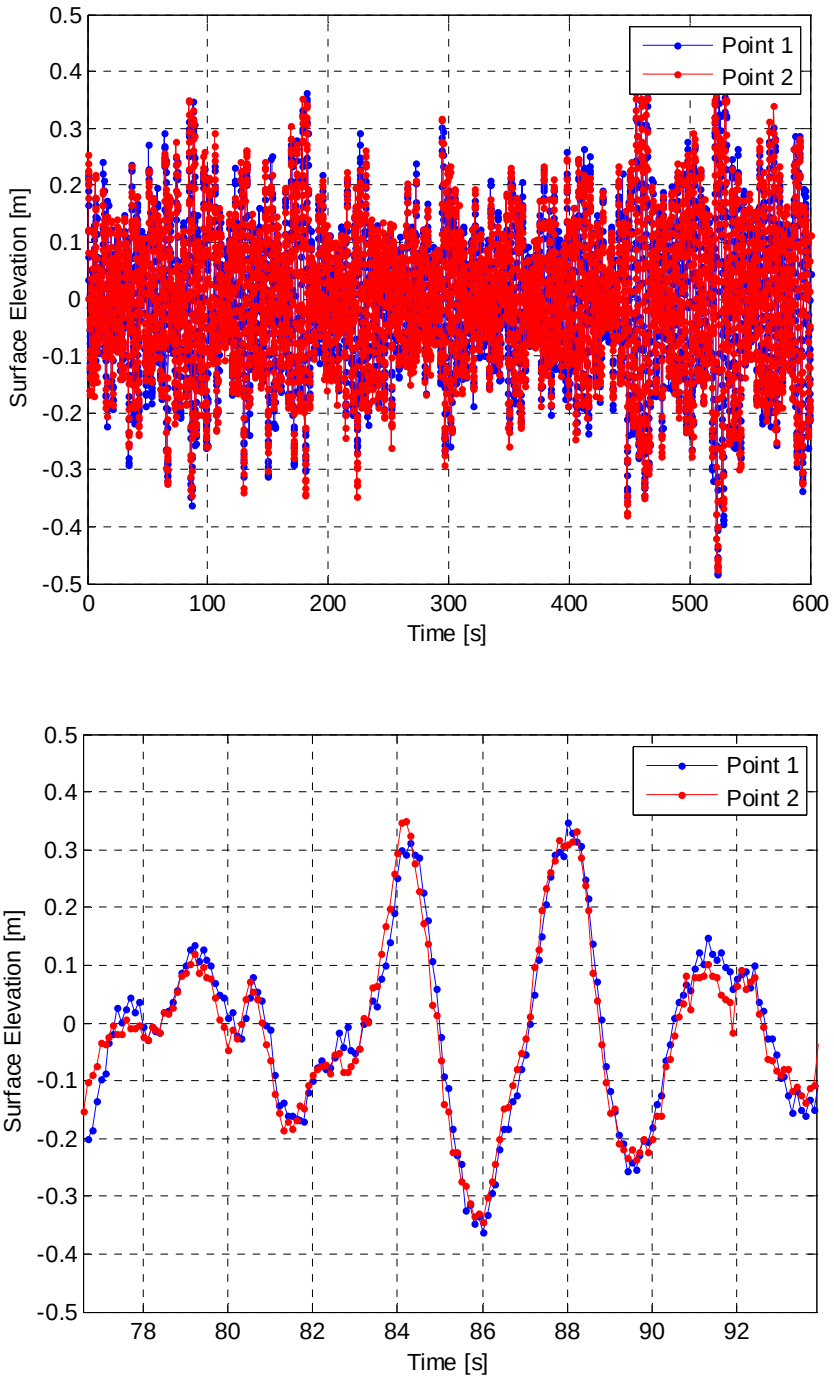

Figure 44 – Experiment 1: (Top) wave surface elevation time series extracted from stereo data at points 1 and 2 located at (x,y)=(4.7 m, 22.2m) and (x,y)=(5.2 m, 22.7m) respectively. (Bottom) Short time series observed at the same points.

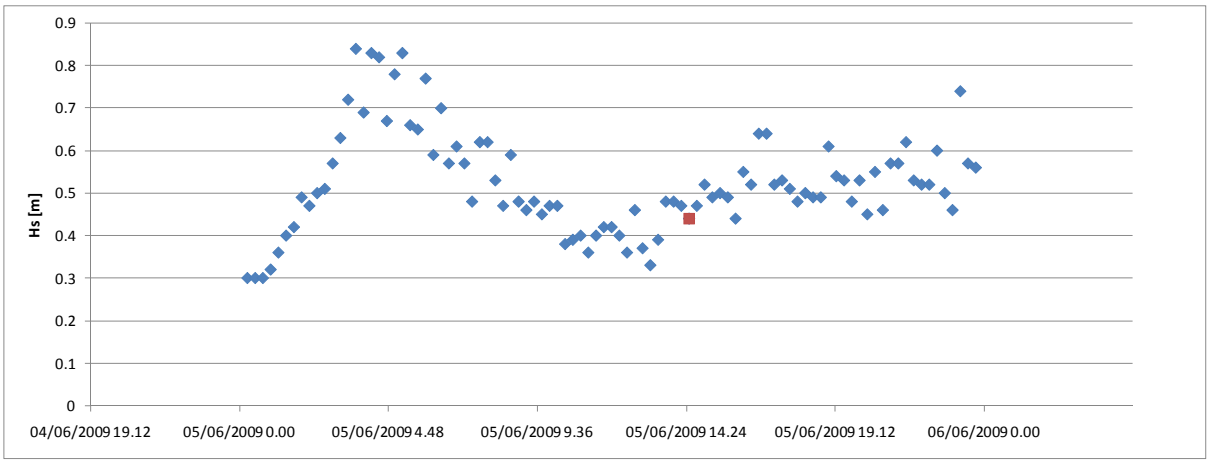

Figure 45 – Experiment 1: Significant wave heights Hs [m] variability at Acqua Alta on June 05, 2009. Red dot denotes time while WASS was operational.

3.2.2. Wave statistics and spectra

Wave elevation time series are extracted from the reconstructed 3D stereo data at point probes of the virtual grid shown in Figure 48. The frequency spectrum S(f) observed at one of these probes is reported in Figure 49. We note a noise floor for frequencies greater than roughly 2.0 Hz. Figure 50 shows the mean directional spectrum S(k_x,k_y) obtained by averaging the 2D Fourier Transform of all the observed spatial snapshots in time. The estimation of the omni-directional spectrum S(k) proceeds by numerically integrating S(k_x,k_y) over all the directions. The resulting mean directional spectrum is shown in Figure 51. In agreement with Zakharov's theory, the spectrum tail decays as $k^{-2.5}$ (Zakharov 1999). In Figure 52 we compared the observed average omnidirectional spectrum with that obtained from the average frequency spectrum, observed at the 12 points of the grid of Figure 48, via the linear dispersion relation.

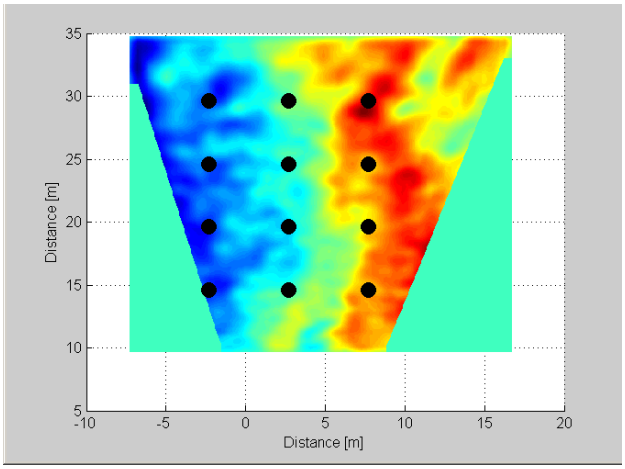

Figure 48 - Experiment 1: Virtual point probe grid for estimation of the average frequency spectrum.

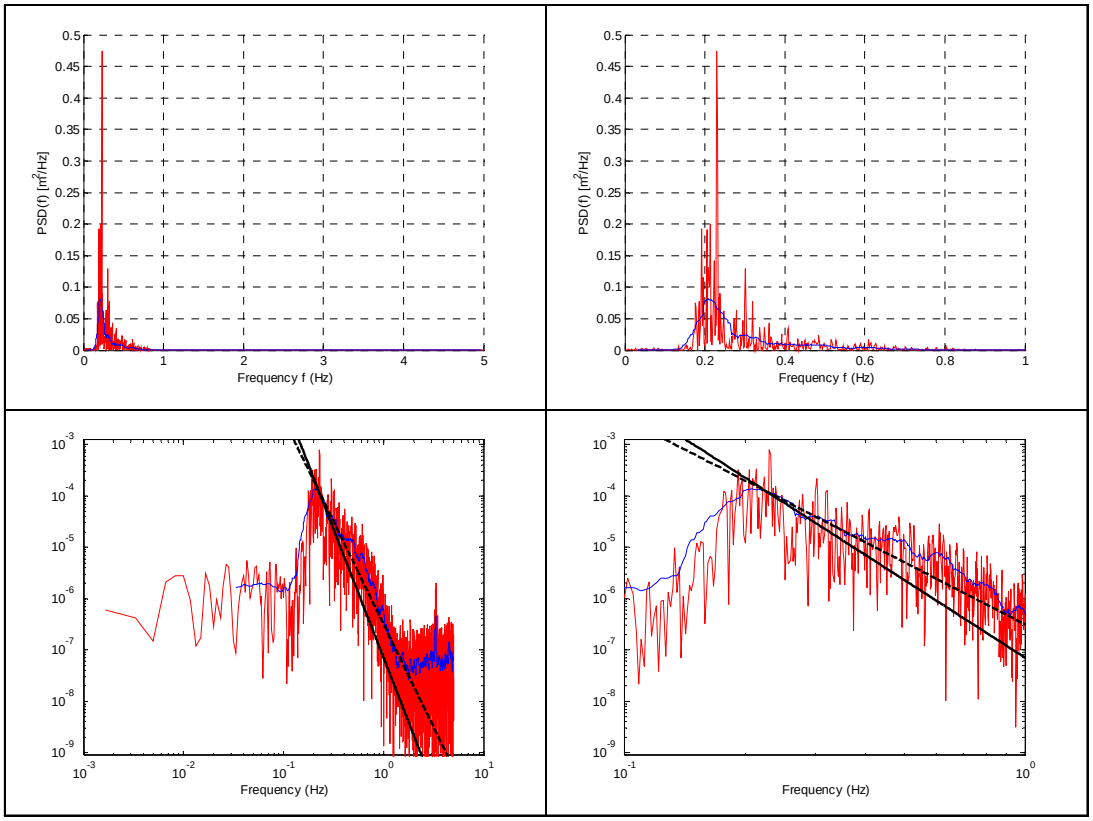

Figure 49 – Experiment 1: Observed frequency spectrum (red) and filtered spectrm (blue) at one of the virtual point probes of Figure 48. Nyquist frequency = 5 Hz. Spectral resolution df = 1.7 x 10^{-3} Hz (equal to 1/Time series duration = 1/600 s). In logarithmical scale, frequency spectrum is compared against f^{-4} (dotted line) and f^{-5} (solid line) spectra.

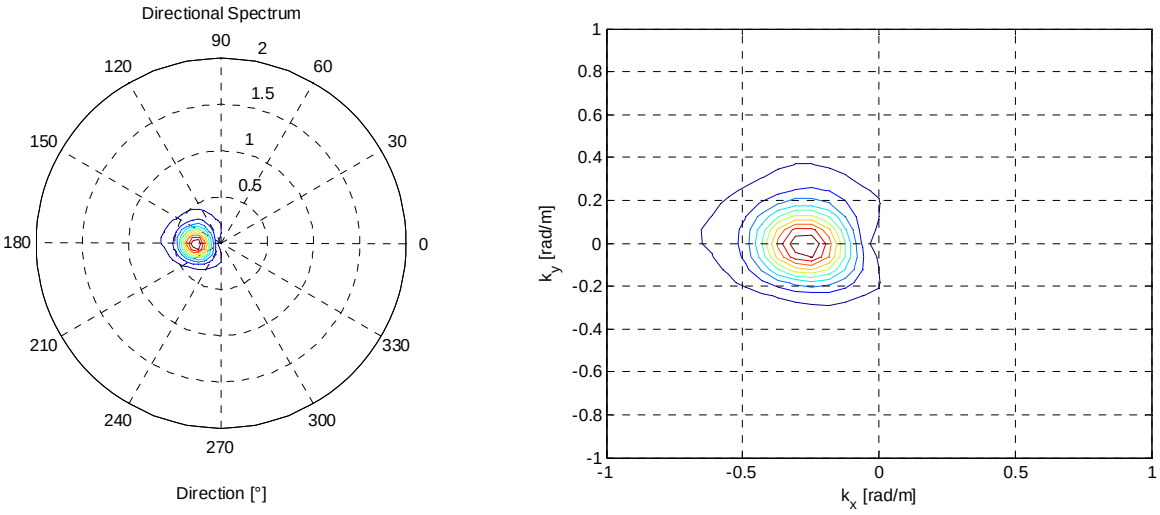

Figure 50 – Experiment 1: Average wavenumber spectrum over the 6000 3D reconstructed sea surface maps. Nyquist wavenumber: $[kx.\ ky]_{max}$ = [62.83 rad/m, 62.83 rad/m]. Spectral Resolution: [kx, ky] = [0.06 rad/m, 0.06 rad/m]. North direction is rotated 46.2° in counterclockwise with respect to the y axis.

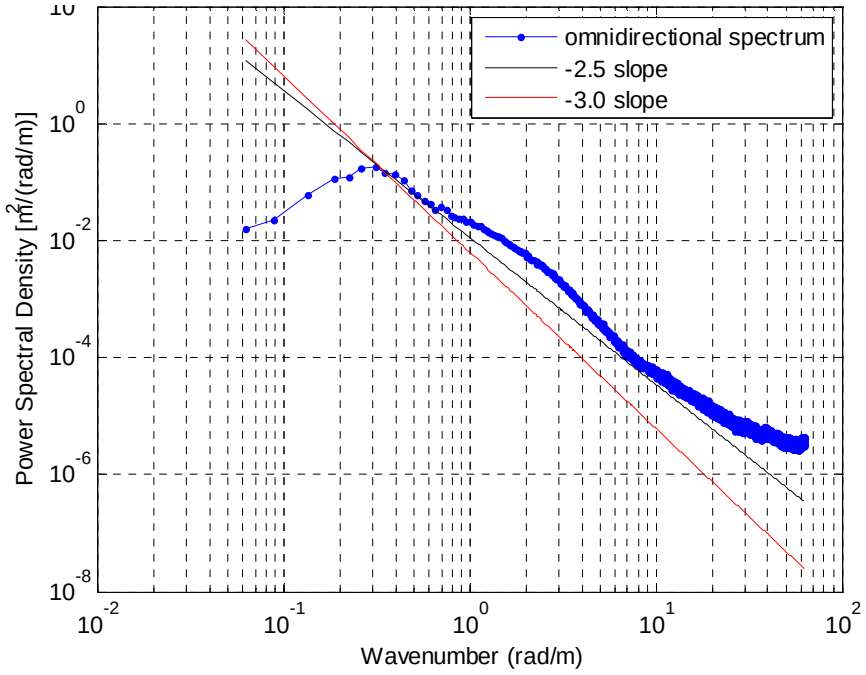

Figure 51 - Experiment 1: Average omnidirectional wavenumber spectrum over the 6000 3D reconstructed sea surface maps. Peak of the Spectrum is at at |k| = 0.309 rad/m, corresponding to a wavelength of 20.3 m.

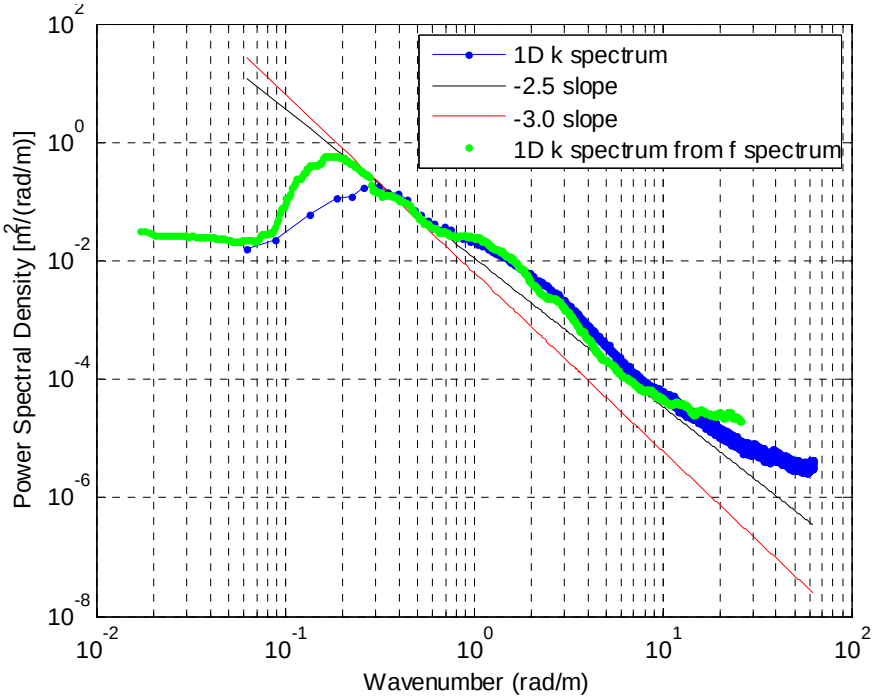

Figure 52 – Experiment 1: Observed average omnidirectional spectrum S(k) (blue) and that obtained from the average frequency spectrum (green) via the linear relation observed from the time series extracted at the points of the virtual probe grid of Figure 48.

3.2.3. Wave Crests over an Area

A total of 735 maps of the sea surface at 0.1 second intervals have been processed. The horizontal resolution of the maps is 0.05 m. To make the processing more manageable, we truncated the data to every fifth point, giving a horizontal resolution of 0.25 m. Figure is a sample contour map of one of the images. The average significant wave height over all good measurement points is 0.450 m. The maximum significant wave height over all of the points was 0.561 m and the minimum significant wave height over all of the points was 0.286 m. The high variability of the significant wave height is expected because of the relatively short record length, even though all of the points are far from independent.

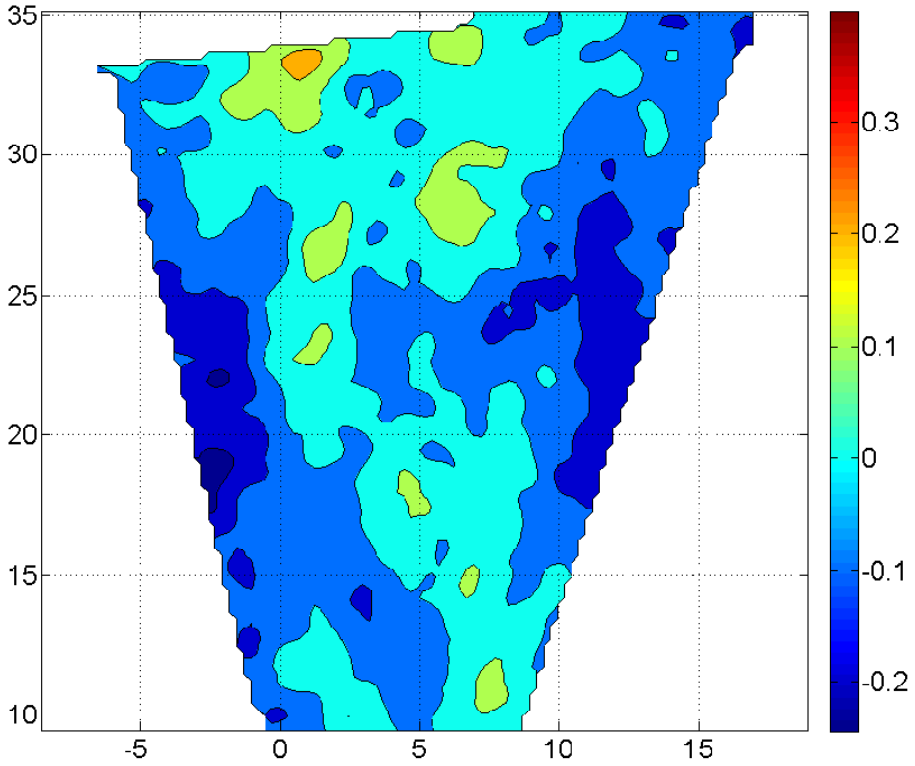

Figure 53 - Experiment 1: sample contour map of the sea surface (units in meters).

Figure shows power spectra from each grid point along with the average spectrum. The spectra were calculated using Welch's method. The peak frequency is at about 0.25 Hz. There appears to be a noise floor that starts between 1 and 2 Hz. In order to eliminate contamination from this noise in the crest height statistics, we low-pass filtered the data at 2 Hz. This step removed very little energy, reducing the average significant wave height from 0.450 m to 0.441 m. The mean wave period is T_1 = 3.49 sec and the zero crossing period is T_Z = 2.91 sec.

The average maximum crest height over all of the good measurement points is 0.317 m. The maximum crest height over all of the good measurement points is 0.482. This gives a very large ratio of 1.52 between the area crest maximum and the point crest maximum. The area covered by good measurements was 389 m2. For simplicity, we simulated linear waves over a 20 m by 20 m square with a spatial resolution of 0.25 m. The input spectrum was a Jonswap spectrum with a peak period of 4.0 seconds, a significant wave height of 0.44 m and a peak enhancement factor of 3. These parameters give a mean wave period T_1 = 3.32 sec and a zero crossing period T_Z = 3.11 sec. Each simulation produced 512 samples at a time step of 1/7.18 sec, giving 73.5 seconds of data. A total of 100 simulations were made.

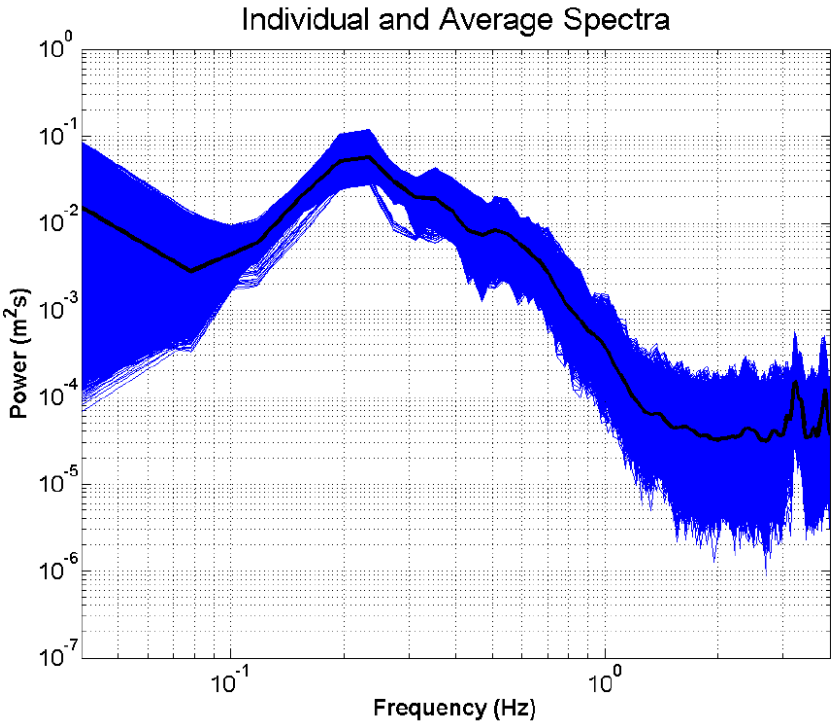

Figure 54 - Experiment 1: wave power spectra (blue curves are individual spectra over thousands of grid points and the heavy black curve is their average).

Figure shows the probability distribution of the ratio between the area crest maximum and the point crest maximum for the simulations. The average ratio was 1.42, which is somewhat lower than the measured ratio. But the distribution of the simulated ratios is very broad, so there is plausible agreement between the simulations and the measurement. Forristall (2006) used simulations along with the theory developed by Piterbarg (1996) and Krogstad et al. (2004) to produce simple formulas for the ratio of area to point maxima. The expected value of the maximum over an area is

$$E(\eta_{\max}) = h_N + 0.5772/h_N \tag{28}$$

where

$$h_N = \left[2\log N + 2\log(2\log N)\right]^{1/2} \tag{29}$$

N is the "equivalent number of waves".

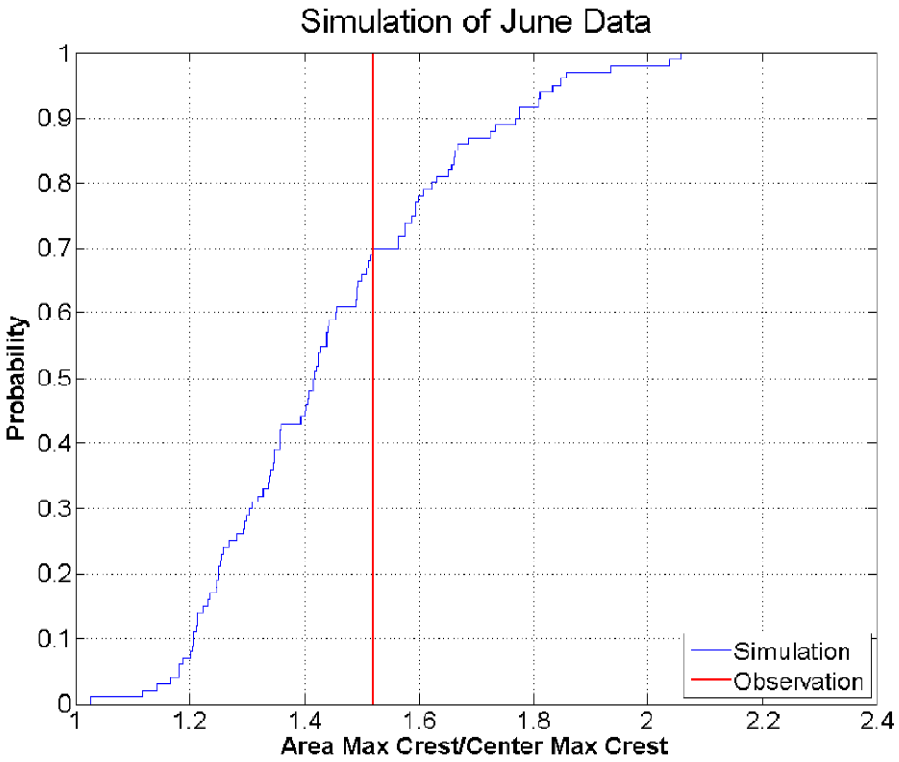

Figure 55 - Experiment 1: the blue line is the empirical distribution function of the ratio between the area maximum crest height and the point maximum crest height. The red line is a the ratio observed at Acqua Alta.

From simulations, Forristall (2006) found that for square areas less than one mean wavelength on a side, the equivalent number of waves is well approximated by

$$N = 2\frac{L}{\lambda_1}\frac{T}{T_z} \tag{30}$$

where L is the square root of the area, T is the time interval, λ_1 is the wave length corresponding to the mean wave period, and T_Z is the zero crossing wave period.

Evaluating previous equations for the parameters of the measured spectrum gives $3.39\sigma = 0.373$ m as the expected maximum crest over a 20 m by 20 m area. The expected maximum at a single point is $2.77\sigma = 0.305$ m. The maximum at a point is somewhat less than the observed average maximum of 0.322 m because the theory is for a linear process. The ratio between the area maximum and the

point maximum is only 1.22, much less than the observed or simulated maxima. The main difference between the simulations and equations (28), (29), and (30) is that equation (30) was based on simulations of waves with a mean period of 8.35 seconds for 1024 seconds, or about 123 waves. The 73.5 seconds of measurements contain only about 21 waves. In the shorter records, there is much more spatial variability of crest heights than temporal variability. To demonstrate this point, we made additional simulations that were 4096 points, or 570 seconds long. The average ratio between area maxima and point maxima for those simulations was 1.29, much closer to the results from equations (28), (29), and (30). The other difference is that the measured area is relatively long compared to the wavelength. Figure , taken from Forristall (2006), shows that the simulations diverge from the curve given by equation (30) when the side of the simulated square is longer than the mean wavelength. The first set (Experiment 1) of '*Acqua Alta*' measurements is consistent with linear simulations of the increase of crest heights over an area.

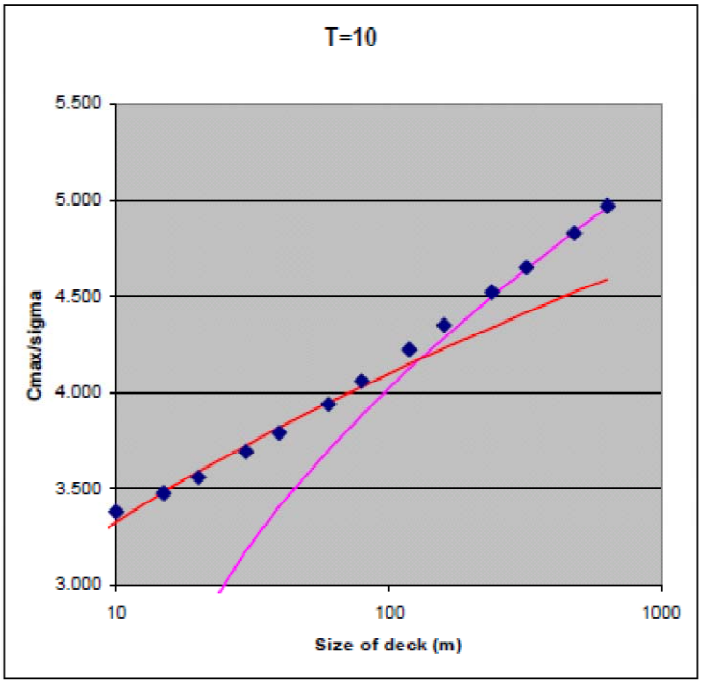

Figure 56 - Expected value of crest heights over an area from simulations of waves with a mean period of 8.35 seconds and a wavelength of 109 m. The red curve comes from equation (30).

3.3. EXPERIMENT 2: 2009 OCTOBER 14, 0755 UTC ÷ 0830 UTC

3.3.1. Stereo cameras setup and 3D reconstruction

A sketch of WASS left and right camera field of view is shown in Figure 57, and an example of stereo pairs (snapshots of the water surface at the same instant of time) is shown in Figure 58. Figure 59 illustrates various images framed by the right camera that provide an idea of the wave conditions during Experiment 2. An example of stereo correspondences (i.e. corresponding pixels of the two cameras of the same point in the world reference system) are shown in Figures 60-61. Here, both the images are corrected for lens aberration and also stereo rectified. Since the imaging set up is discrete in nature, the image coordinates of each pixel can be assumed to suffer from quantization errors of up to ± 1/2 pixel for each camera. The quantization error distribution of the final 3-D points in the x, y and z directions after stereo triangulation and the associated exceedance probability of its absolute value are shown in Figure 62. Because of quantization error, 3-D coordinates are biased. The max and mean quantization errors can be reduced by applying subpixeling techniques (see Figure 63). Figure 64 shows the reconstructed 3D points in the left camera reference system, obtained after triangulation of stereo pairs (corresponding pixels in left and right cameras images), and Figure 65 grids the same 3D points in the world reference system. Successive snapshots of the 3D reconstruction of the water surface in time are shown in Figure 66, and Figure 67 reports time series of the wave displacements extracted at given virtual point probes. Finally, Figure 68 shows the variability of the significant wave height at '*Acqua Alta*' during Experiment 2.

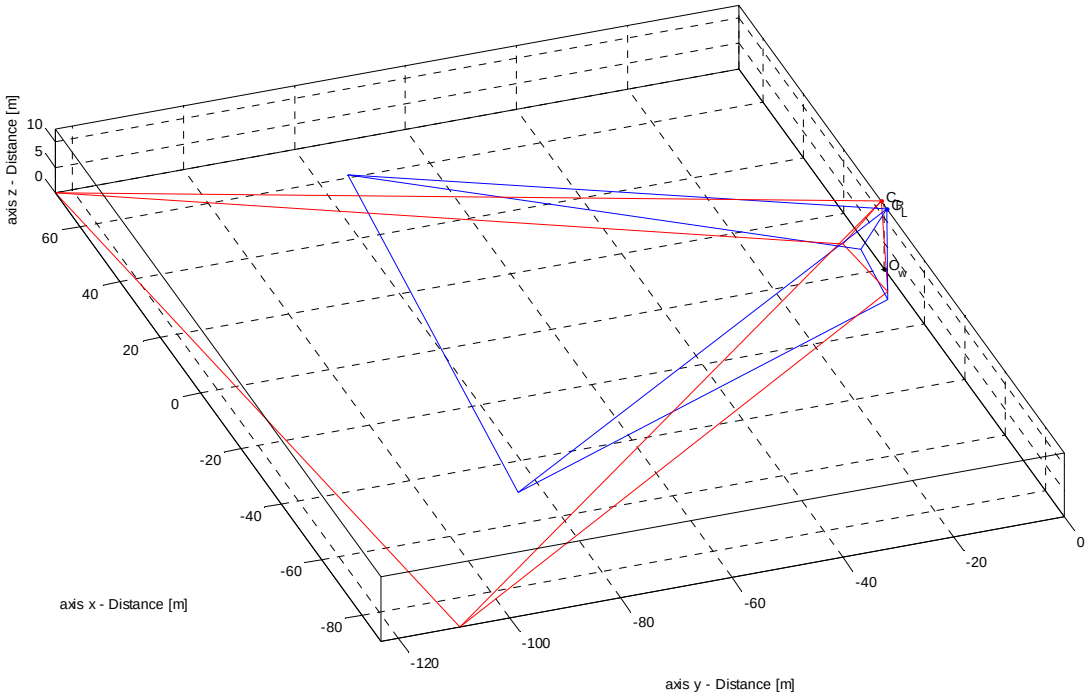

Figure 46 - Sketch of WASS installation for Experiment 1 in October 14, 2009. Fields of View of Left (blue lines) and right (red lines) cameras. Cameras are positioned at approximately 12.5 m above the mean sea level (z = 0).

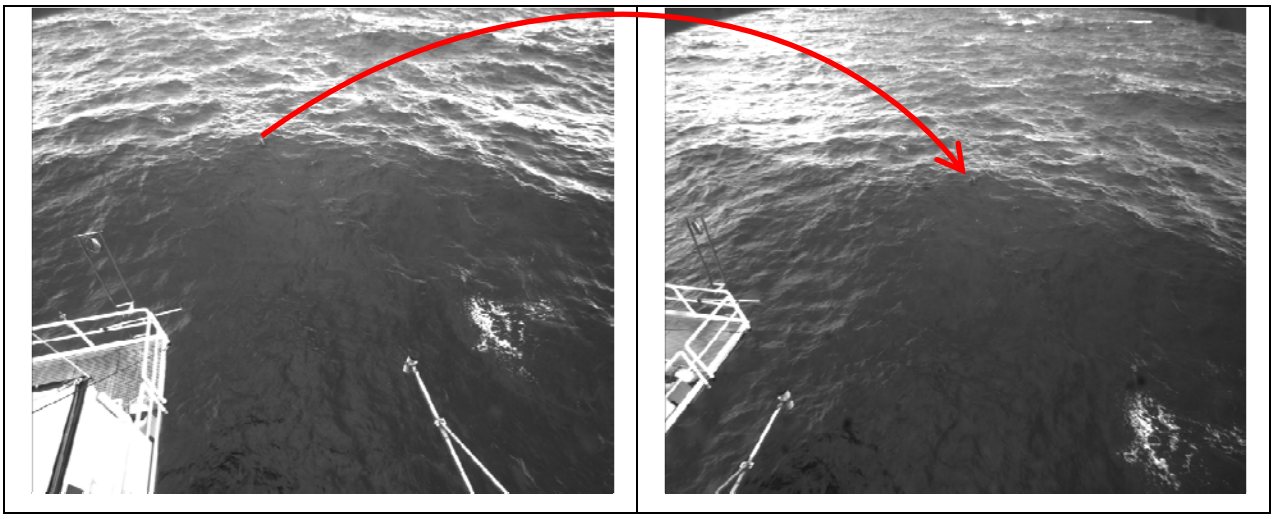

Figure 47 – Experiment 2: example of stereo pair snapshots, left and right camera images before lens aberration correction and stereo rectification. Arrows points at corresponding sea points in the two frames.

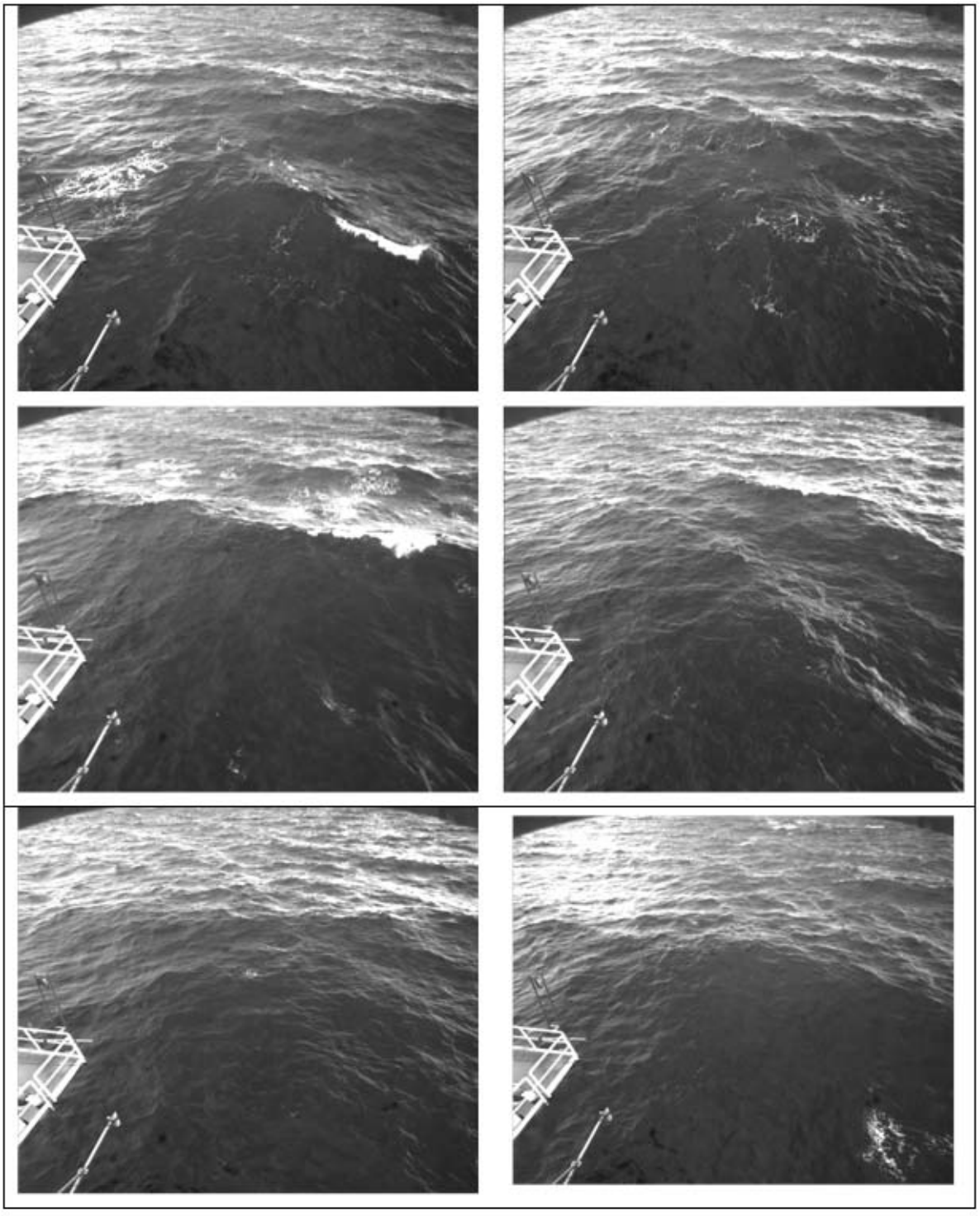

Figure 59 - Experiment 2: example of images framed by right camera during in Oct 14 2009.

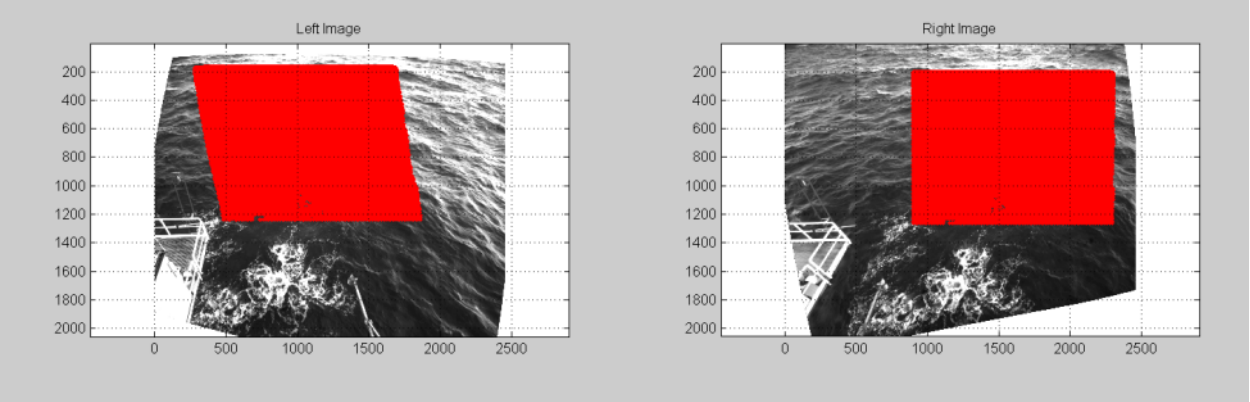

Figure 60 - Experiment 2: example of stereo correspondences. Red points in Left and Right images are corresponding points of the same sea surface pixel. Images are corrected for lens aberration and stereo rectified.

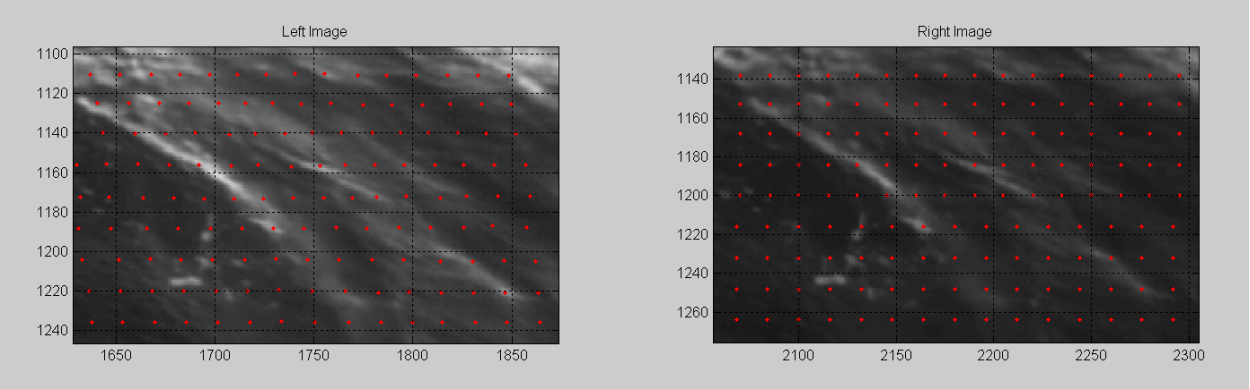

Figure 61 - Experiment 2: example of stereo correspondences. Red points in Left and Right images are corresponding points of the same sea surface 3D point.

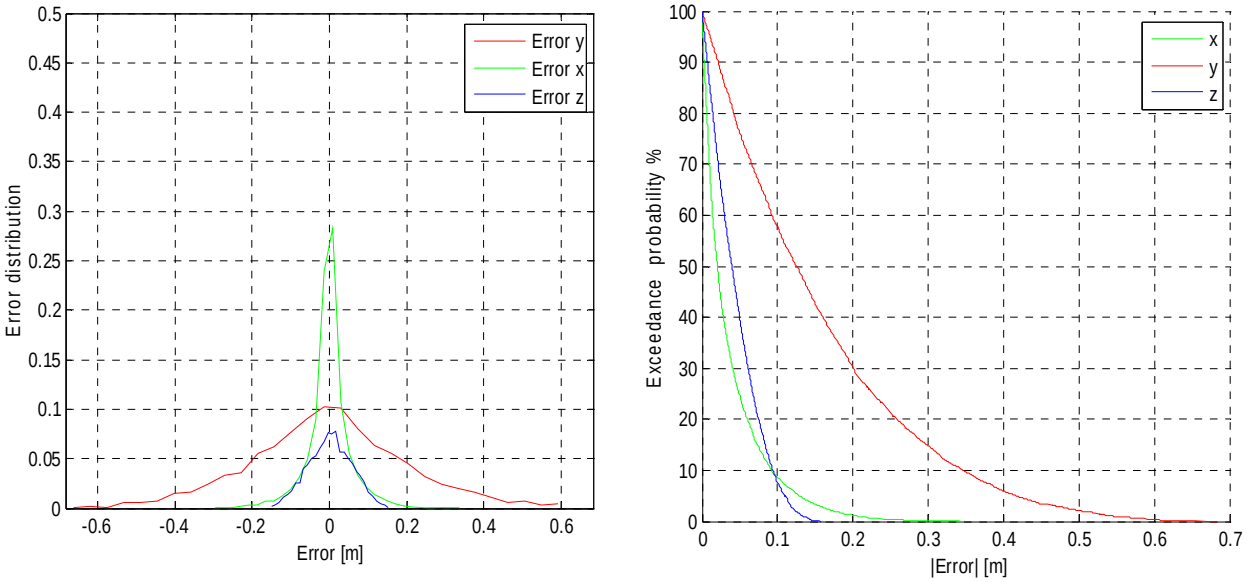

Figure 62 – Experiment 2: (Left) Distribution of quantization errors and (Right) exceedance probability of their absolute values along the x,y, and z axes. Errors refer to pixel-to-pixel triangulation of red pixels of Figure 60 without any subpixel detection. (x,y,z axes as in Figure 57).

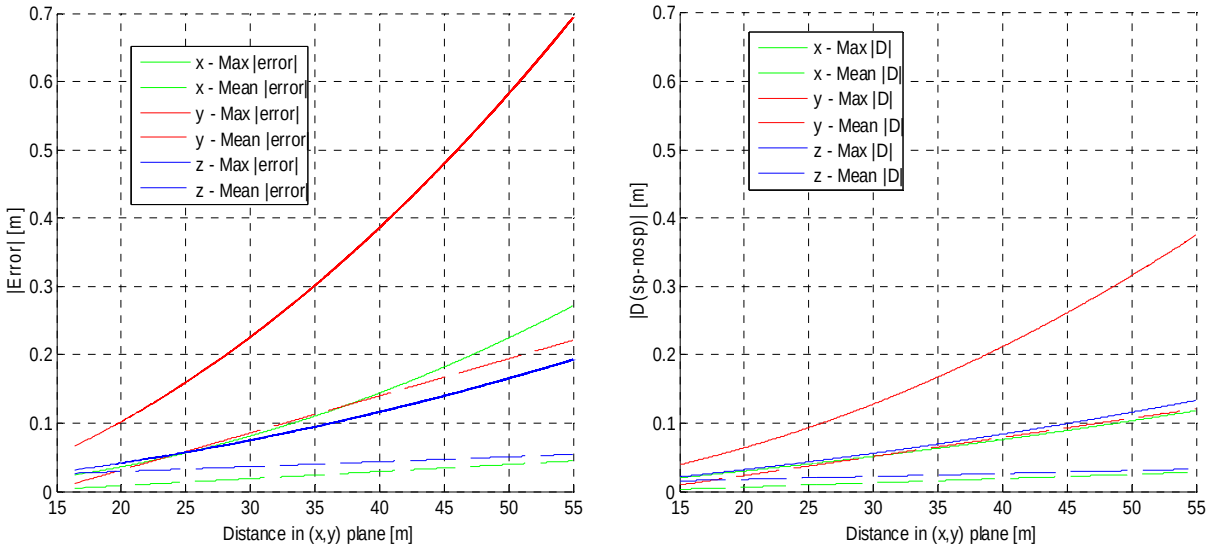

Figure 63 – Experiment 2: (Left) Max and mean absolute quantization errors as function of the horizontal distance from the cameras after stereo triangulation and (Right) after subpixel correction.

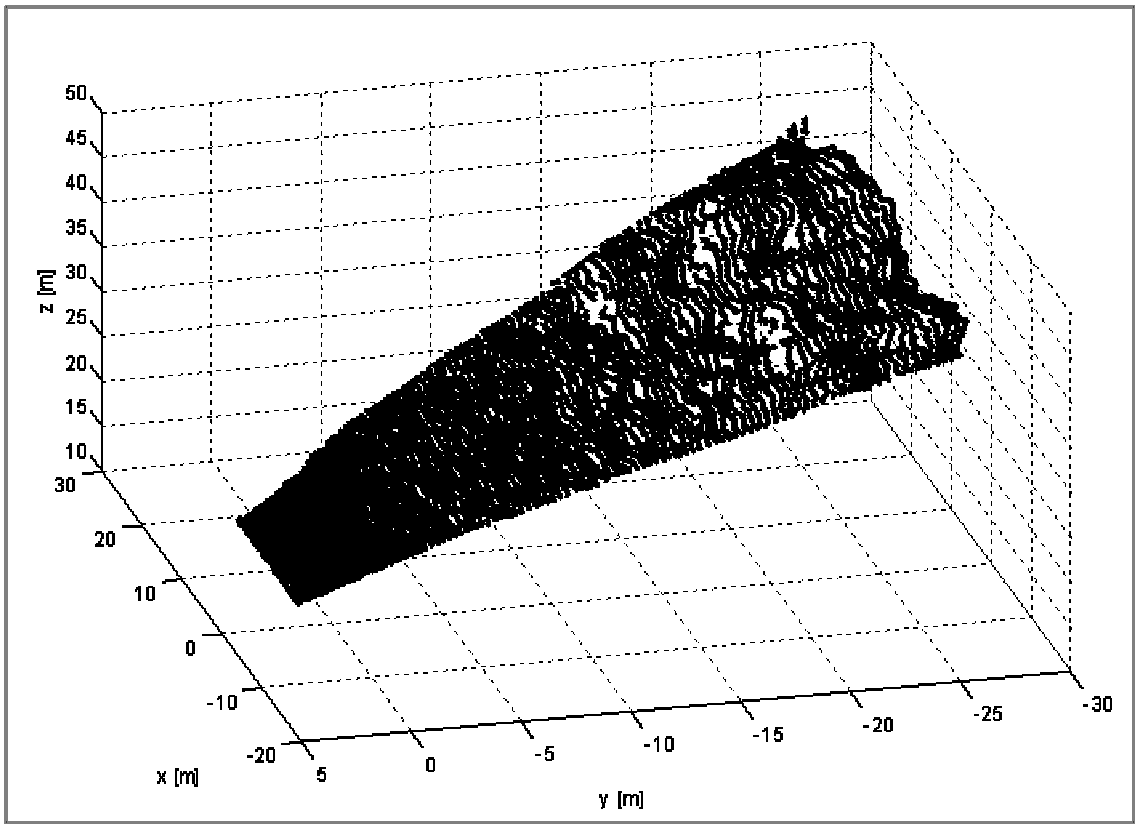

Figure 64 - Experiment 2: 3D points in Left camera reference system. Z is the distance of each 3D point from the CCD principal point.

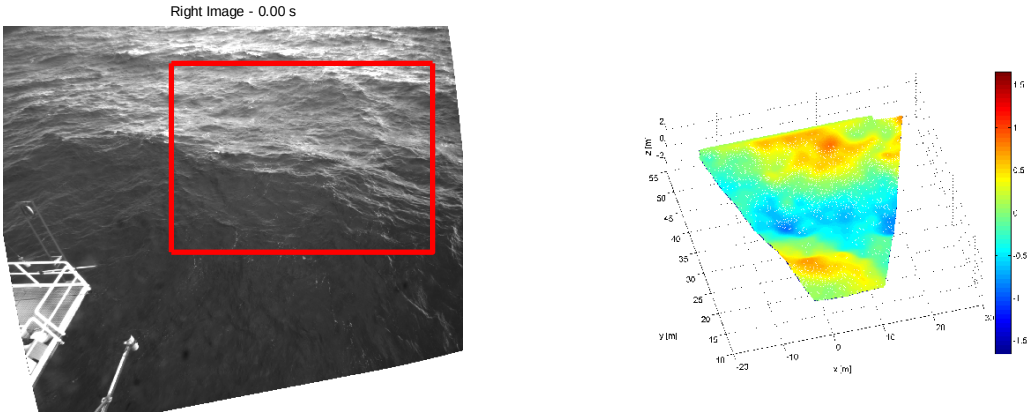

Figure 65 - Experiment 2: (Right panel) 3D points gridded in the world reference system where (x,y) plane is orthogonal to gravity direction z, and (Left Panel) recosntructed area.

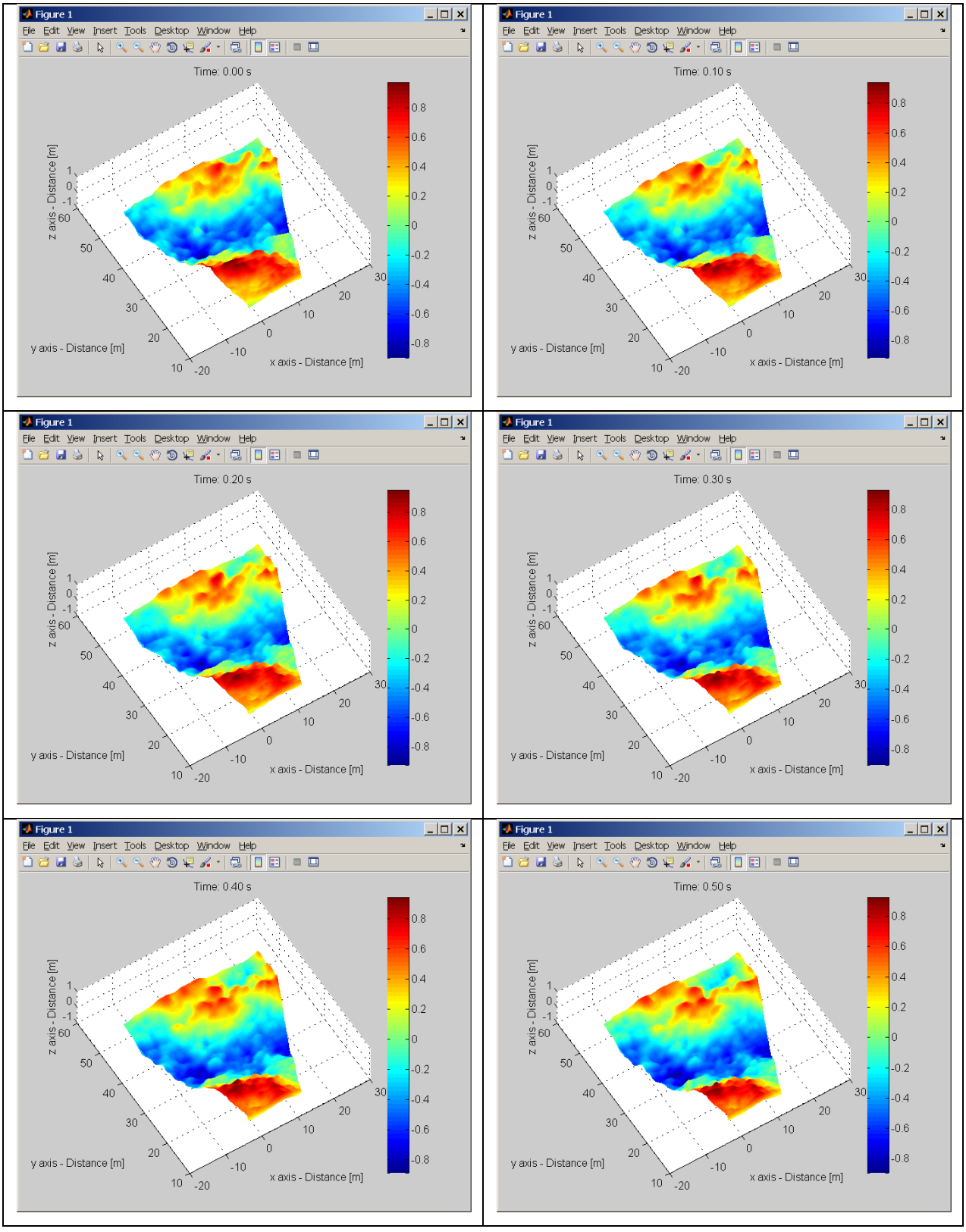

Figure 66 – Experiment 2: example of 3D reconstruction of water surface shape in time. Time distance between consecutive images (from left to right, from top to bottom) is 0.1 s.

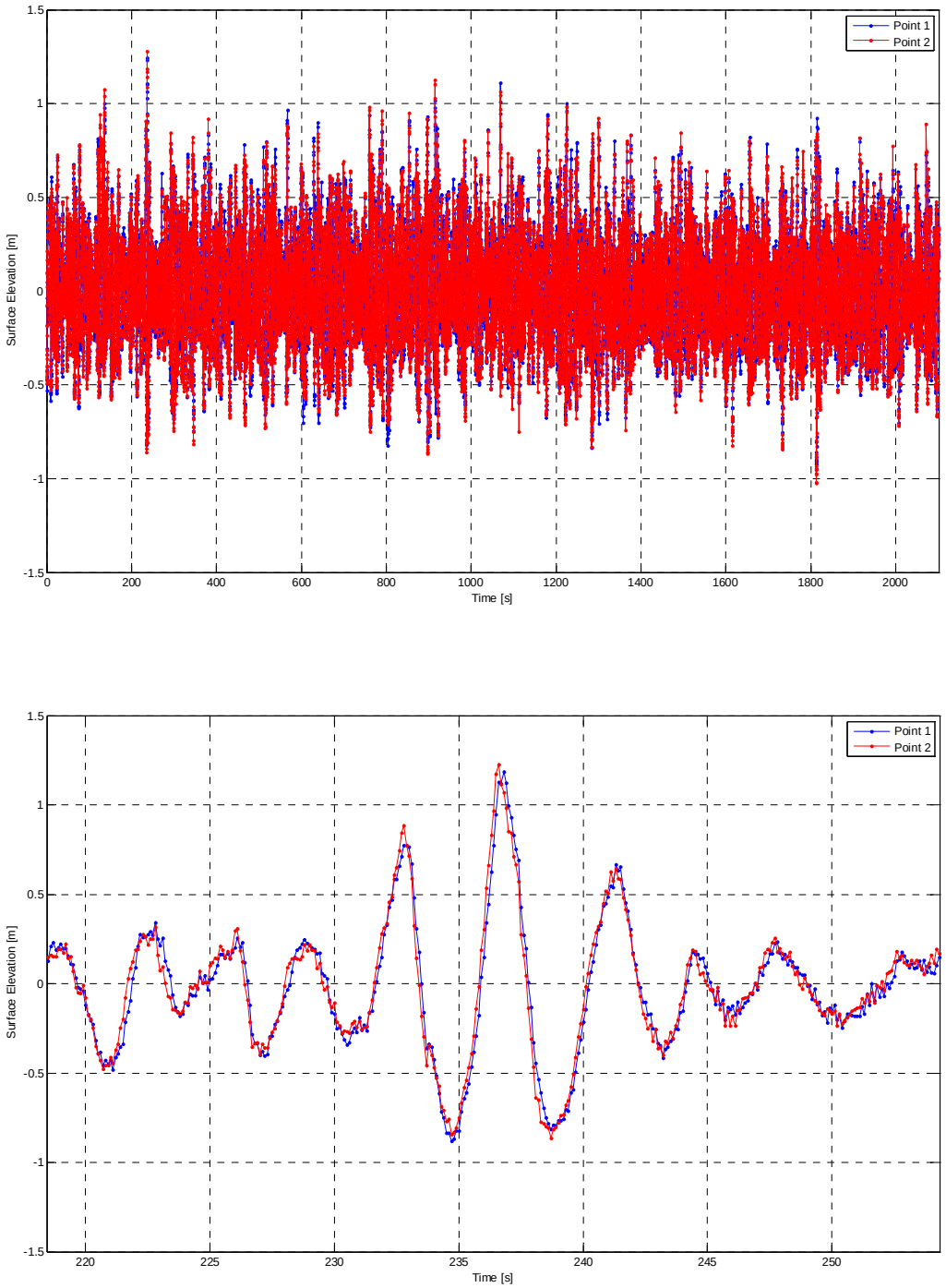

Figure 67 – Experiment 2: (Top) wave surface elevation time series extracted from stereo data at points 1 and 2 located at (x,y)= (5.4 m, 30.5m) and (x,y)= (5.9 m, 31.0m) respectively. (Bottom) Short time series observed at the same points.

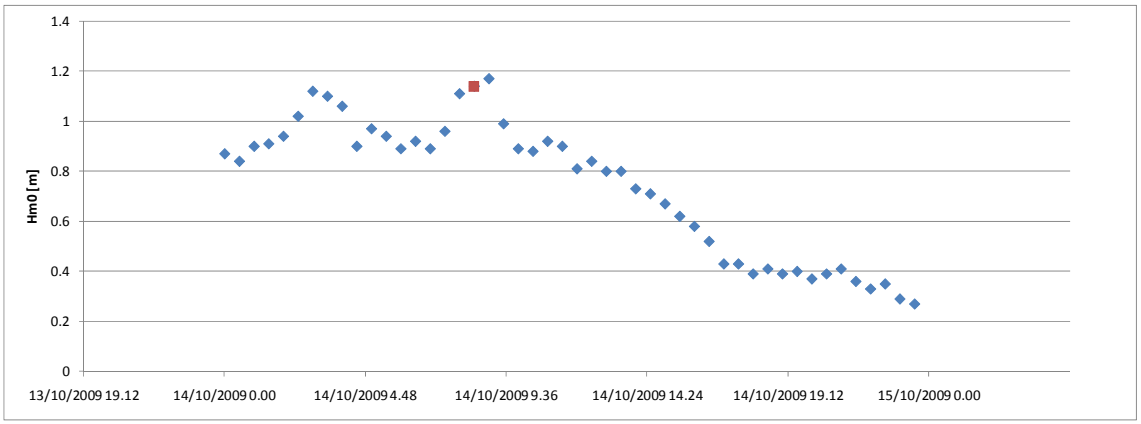

Figure 68 – Experiment 2: Significant wave heights Hm0 [m] variability at Acqua Alta on Octber 14, 2009. Red dot denotes time while WASS was operational.

3.3.2. Wave spectra

A visualization of the four dimensional wave surface $z=\eta(x,y,t)$ defined on a space-time volume V via horizontal and vertical slicing is shown in Figure 69 along with the time series of wave displacements extracted at several points in the domain. Both spectra and statistics of waves are then computed by analyzing the ensemble of the extracted time series with a total number of roughly 7000 waves. The average significant wave height H_s = 1.10 m and the mean wave period T_m=3.62 s. The frequency spectrum S(f) observed at one of these probes is reported in Figure 70. The average frequency spectrum S(f) shown in Figure 71, mean of the observed spectra at all the virtual point probes (see Figure , decays as f^4 in agreement with Zakharov's theory (Zakharov 1999). We noticed noise above f_{max}=1.0 Hz, and thus ignored the energy content above it with variations less than 0.5% in the wave variance. Figure 72 shows the mean directional spectrum S(k_x,k_y) obtained by averaging the 2D Fourier Transform of the 21000 3D reconstructed sea surface maps. The estimation of the omni-directional spectrum S(k) proceeds by numerically integrating S(k_x,k_y) over all the directions. The resulting mean directional spectrum is shown in Figure 73. In agreement with Zakharov's theory, the spectrum tail decays as $k^{-2.5}$ (Zakharov 1999). In Figure 74 we compared the observed average omnidirectional spectrum with that obtained from the average frequency spectrum of Figure 71, via the linear dispersion relation.

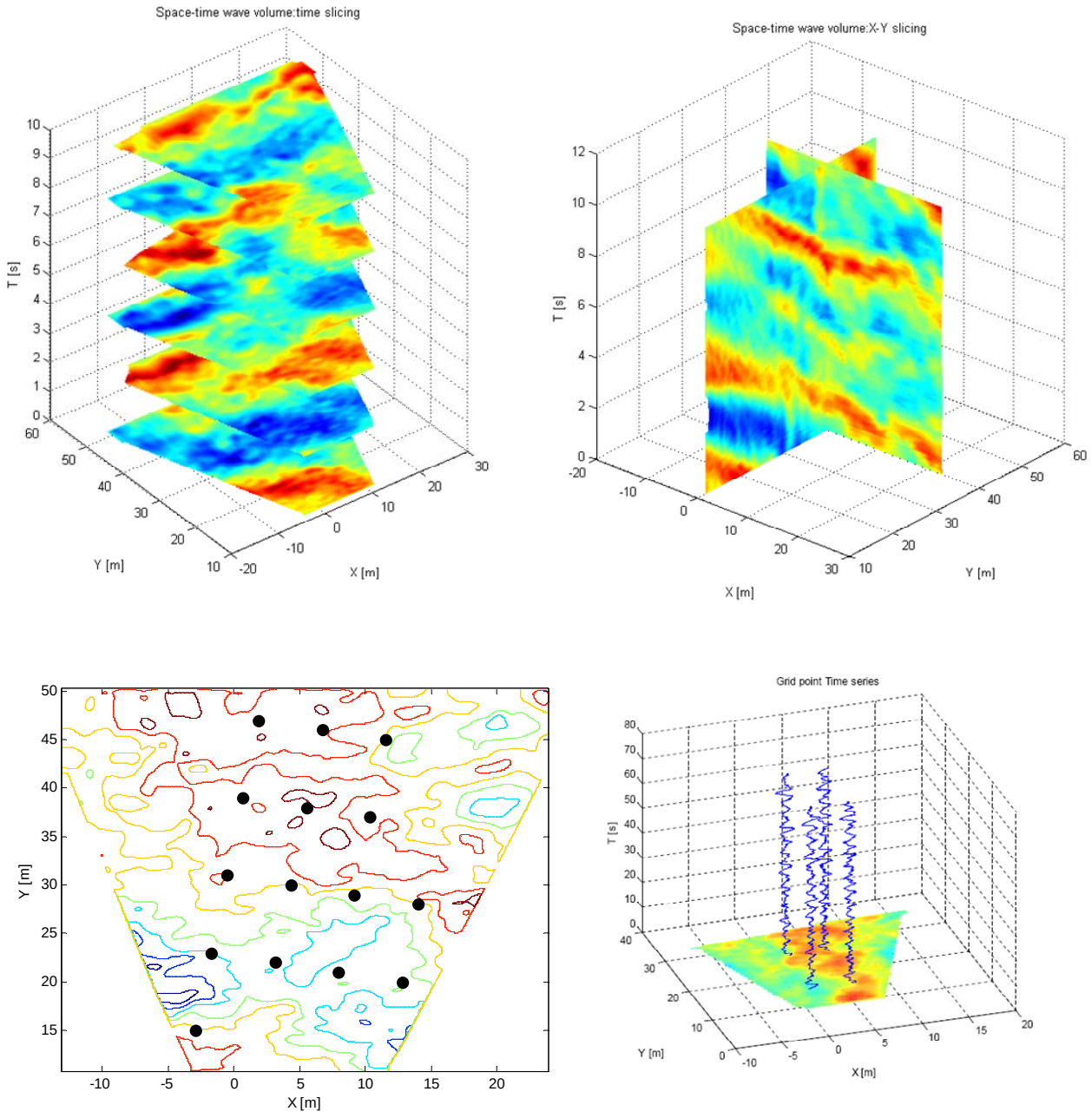

Figure 69 - (Top-left) horizontal slicing of the wave space-time volume V (sequence of snapshots); (Top-right) vertical slicing of V; (Bottom-left) location of the virtual probes and (Bottom-right) extracted time series.

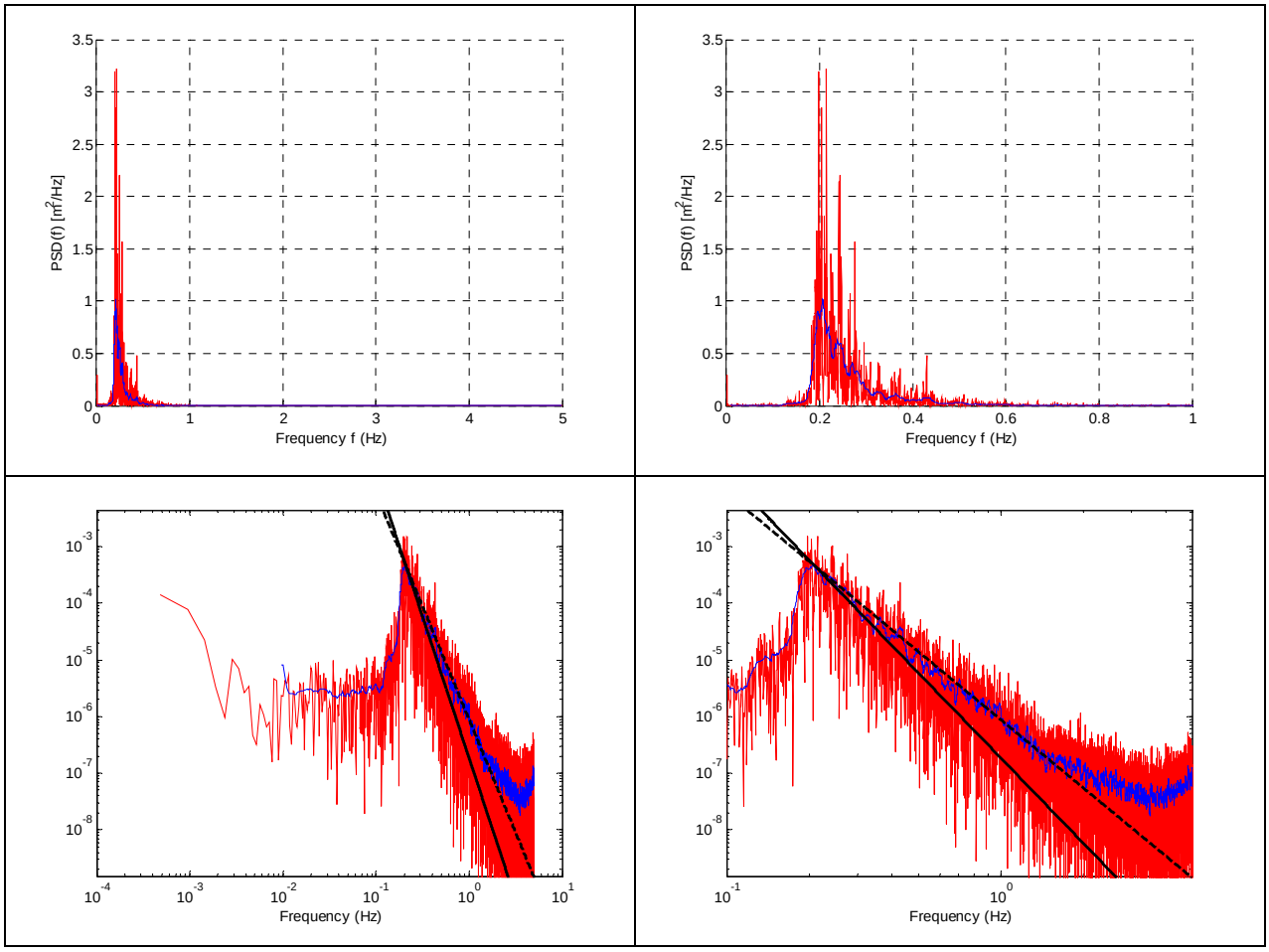

Figure 70 – Experiment 2: Observed frequency spectrum (red) and its filtered spectrum (blue) estimated from time series extracted from the wave space-time volume of Figure 67. Nyquist frequency = 5 Hz. Spectral resolution Df = 4.8 x 10^{-4} Hz (equal to 1/Time series duration = 1/2100 s). Filtered spectrum (in blue) is superimposed. In logarithmical scale, f^{-4} (dotted line) and f^{-5} (solid line) spectra are plotted.

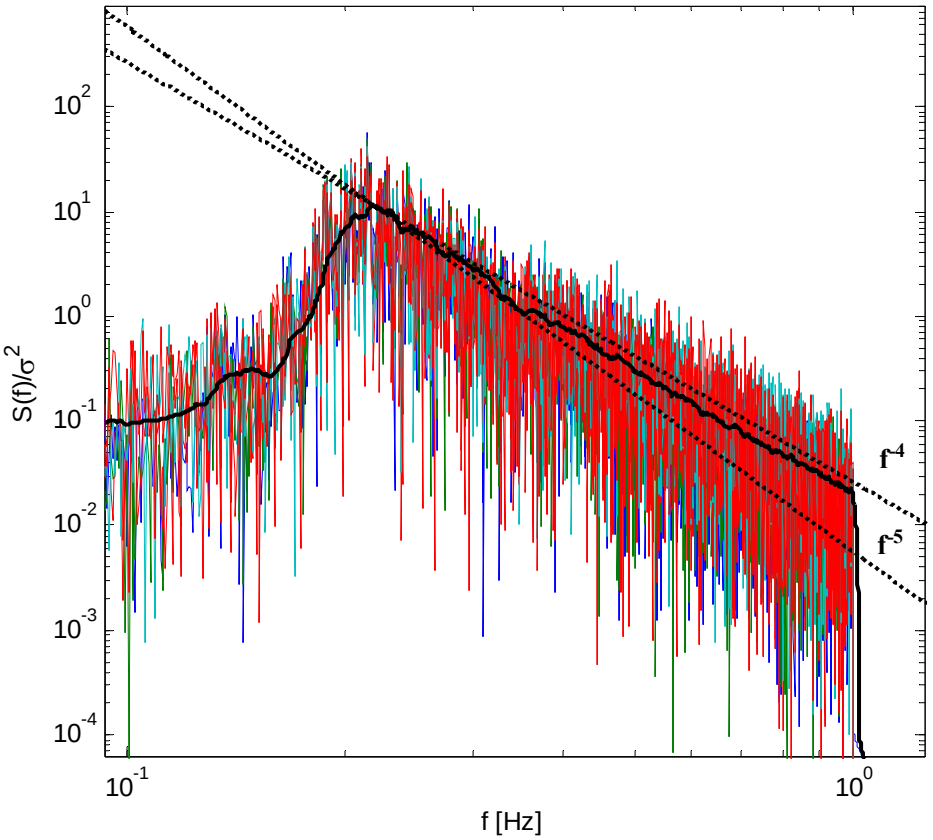

Figure 71 - Experiment 2: average frequency spectrum of the observed spectra at all the virtual probes indicated in figure 69.

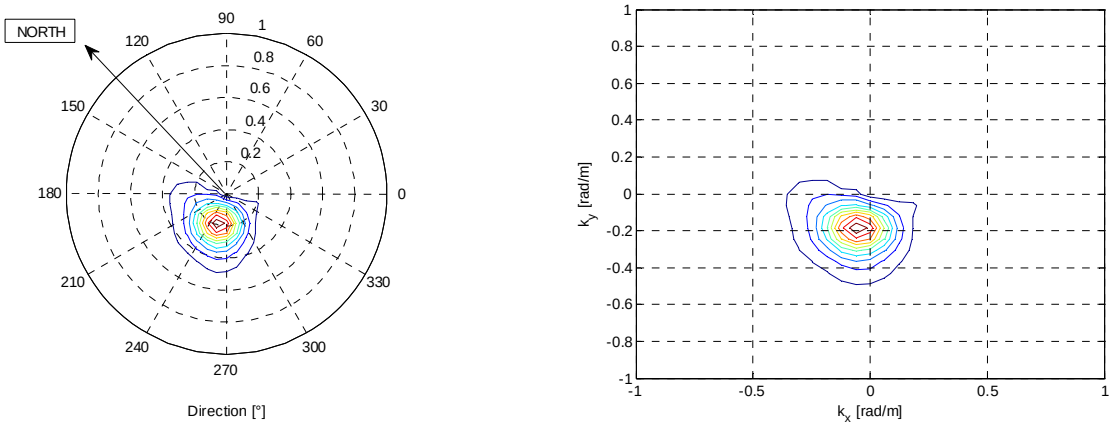

Figure 72 – Experiment 2: Average wavenumber spectrum over 21000 3D reconstructed sea surface maps. Nyquist wavenumber: $[kx.\ ky]_{max}$ = [62.83 rad/m, 62.83 rad/m]. Spectral Resolution: [kx, ky] = [0.06 rad/m, 0.06 rad/m]. North direction is rotated 46.2° in counterclockwise with respect to the y axis.

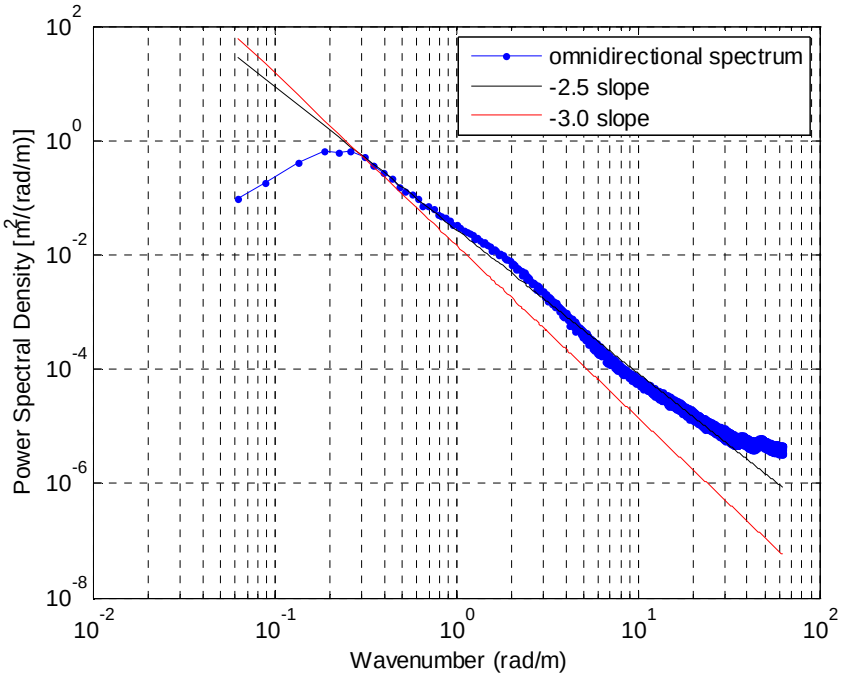

Figure 73 - Experiment 2: 1D (omnidirectional) wavenumber spectrum. Mean Wavenumber Spectrum over 21000 3D sea surface maps. Peak of the Spectrum is at at |k| = 0.186 rad/m, corresponding to wavelength of 33.7 m.

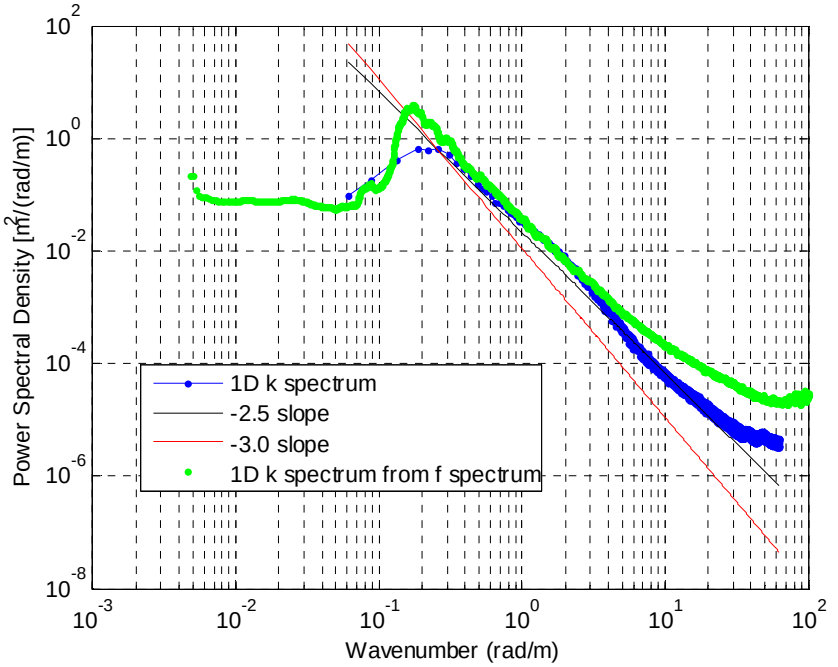

Figure 74 – Experiment 2: Observed average omnidirectional spectrum S(k) (blue) and that obtained from the average frequency spectrum (green) via the linear relation observed from the time series extracted at the points of the virtual probe grid of Figure 69.

3.3.3. Wave Statistics

By collecting the time waves observed at all the virtual probes indicated in Figure , we can now estimate the wave height distribution which is shown in Figure 75. A fair agreement with the Boccotti asymptotic form given by (Boccotti 2000, Tayfun and Fedele 2007)

$$P(H > h) = c\ \exp\left(-\frac{h^2}{4\sigma^2(1+\psi^*)}\right) \tag{31}$$

is observed. Here, the parameters c and ψ^* both depend upon the first minimum of the wave covariance. In particular their mean values over the time series ensemble are $c \approx 1, \psi^* \approx 0.66$.

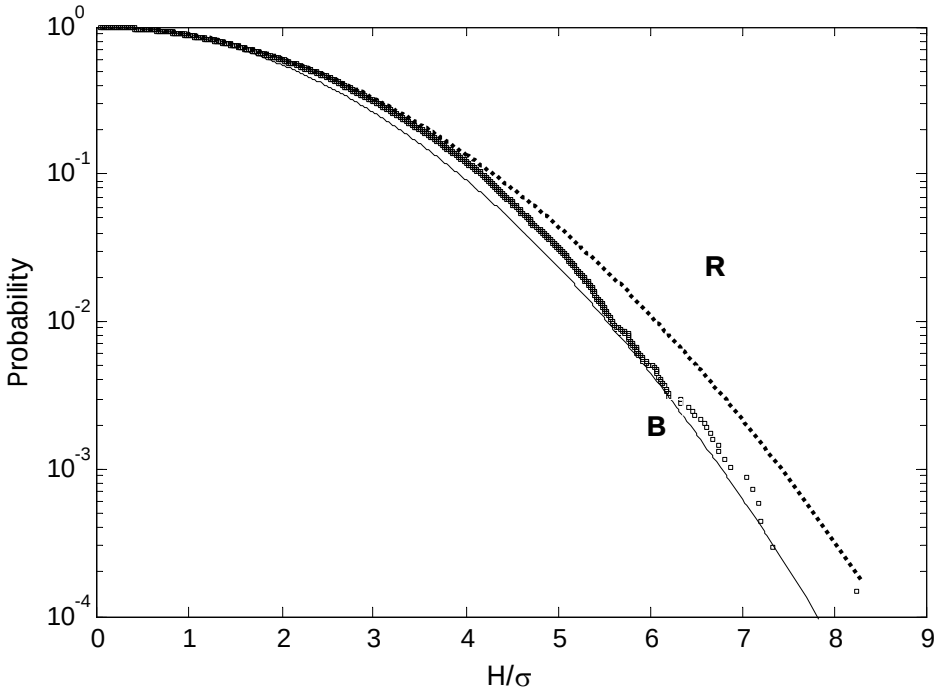

Figure 75 - Experiment 2: Wave height exceedance probability; R=Rayleigh, B=Boccotti.

The observed crest/trough statistics is compared against the Tayfun-Fedele (TF) and Forristall (F) models. The TF distributions for crest (C) and trough (T) heights are given, respectively, by (Tayfun and Fedele 2007a, Fedele 2008)

$$P(C > h) = \exp\left(-\frac{Z_c^2}{2}\right)\left(1+\frac{\Lambda}{64}z^2(z^2-4)\right) \tag{32}$$

$$P(T > h) = \exp\left(-\frac{z^2}{2}(1+0.5\mu z)^2\right)\left(1+\frac{\Lambda}{64}z^2(z^2-4)\right) \tag{33}$$

where $z = h/\sigma$, Z_c is derived from the quadratic equation $z = Z_c + \mu Z_c^2/2$, with μ as a characteristic parameter that measures wave steepness (Tayfun 1986, Fedele and Tayfun 2009) and Λ is a measure of quasi-resonant third order nonlinearities and it depends upon the fourth order cumulants of the wave surface η (Tayfun and Fedele 2007a). For our data set $\Lambda \cong 0$, and second order nonlinearities are dominant. The wave steepness can be estimated directly from data via time averages as $\mu = <\eta^3>$, where $<\bullet>$ denotes expectation. However, these estimators are usually statistically unstable. A stable estimate for μ can be defined from the moments of the wave spectrum as (Fedele and Tayfun 2009)

$$\mu_a = \mu_m(1-\nu+\nu^2) \tag{34}$$

where ν is the spectral bandwidth given by

$$\nu = \sqrt{\frac{m_0 m_2}{m_1^2} - 1}, \tag{35}$$

where $m_j = \int \omega^j S(\omega) d\omega$ are the spectral moments, and μ_m is the steepness for narrowband waves, i.e. as $\nu \to 0$, that is (Tayfun 1986)

$$\mu_m = \sigma \frac{\omega_m^2}{g} \tag{36}$$

with $\omega_m = m_1/m_0$ as the mean up-crossing frequency. The observed values for these parameters are given by $\mu = 0.080$, $\mu_m = 0.090$, $\mu_a = 0.069$, $\nu = 0.52$.

The Forristall model (Forristall 2000) for crest heigths is expressed as

$$P(C > z) = \exp\left(-\left(\frac{z}{4\alpha}\right)^{\beta}\right) \tag{37}$$

Here, for unidirectional (2D) seas Forristall parameters are estimated as

$$\begin{aligned} \alpha_2 &= 0.3536 + 0.2892 S_1 + 0.1060 U_r \\ \beta_2 &= 2 - 2.1597 S_1 + 0.0968 U_r^2 \end{aligned} \tag{38}$$

where

$$S_1 = \frac{2\pi}{g}\frac{H_s}{T_m^2}, \qquad U_r = \frac{H_s}{k_m^2 d^3} \tag{39}$$

The observed values are: $S_1 \approx 0.071$, $U_r \approx 0$ and $\alpha_2 = 0.374$, $\beta_2 = 1.848$. For multidirectional (3D) seas, the same parameters are given by

$$\alpha_3 = 0.3536 + 0.2568\, S_1 + 0.08\, U_r$$
$$\beta_3 = 2 - 1.7912\, S_1 - 0.5302\, U_r + 0.284\, U_r^2 \qquad (40)$$

and from the data set it follows $\alpha_3 = 0.372$, $\beta_3 = 1.874$, respectively. The observed crest exceedance is given in Figure 76. Good is the agreement with both the TF and F models (see Eqs. 33 and 37 respectively). The observed trough statistics fairly agrees with the TF model (34) as well.

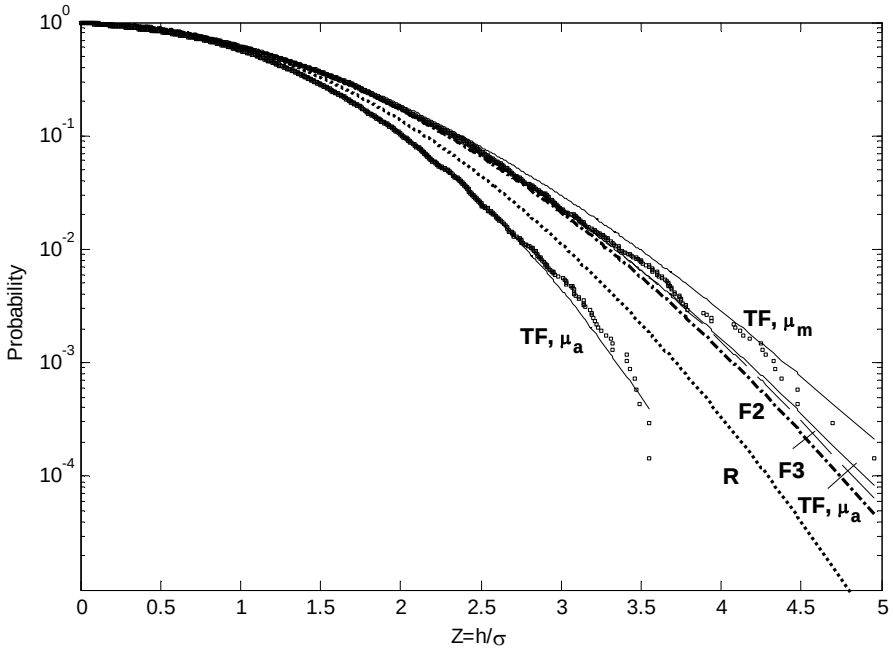

Figure 76 - Experiment 2: Wave crest exceedance probability; R=Rayleigh, TF, μ =Tayfun-Fedele model with steepness μ , F2=2D Forristall, F3=3D Forristall.

For one dimensional data, i.e. time series, the expected maximum wave height $Z(N) = < H_{\max} / \sigma >$ of N observed waves is given by (Tayfun and Fedele 2007a)

$$Z(N) = \sqrt{\log(c_0 N)/c_1} + \frac{\gamma_e}{2\sqrt{c_1 \log(c_0 N)}}, \qquad (41)$$

where $\gamma_e \approx 0.5772$, and $c_0 = 1$, $c_1 = 1/8$ for the Rayleigh model, and

$$c_0 = (1+b)/\sqrt{2b(1-a)}\,,\ c_1 = 0.25/(1-a) \qquad (42)$$

for the Boccotti model with $a = -\psi^*$, $b \approx 1$. Both the Rayleigh (R) and Boccotti (B) models are compared against data in Figure 77. R overestimates the observed expected maximum wave heights as expected because it does not account for bandwidth effects as B does.

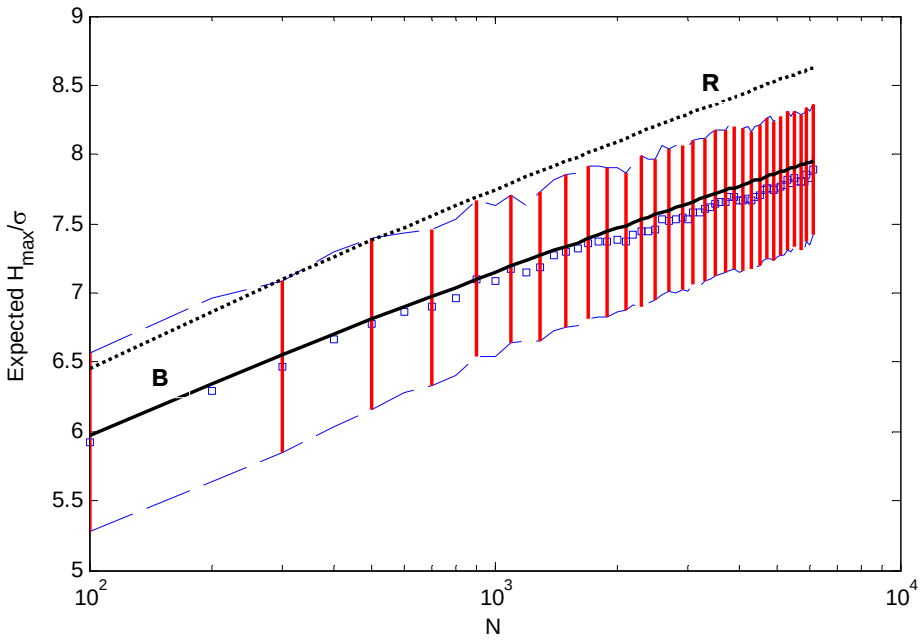

Figure 77 - Experiment 2: Expected maximum crest height: observed average max wave height amplitudes (square dots) and relative stability bands $Z(N) \pm \sigma_N$, σ_N being the associated standard deviation, and theoretical R=Rayleigh, B=Boccotti models, respectively.

The expected maximum crest height $C_T(N) =< C_{\max} / \sigma >$ of N observed waves in one dimensional data is given by the Tayfun model (Tayfun and Fedele 2007a)

$$C_T(N) = h_N + \frac{\mu}{2} h_N^2 + \gamma_e \left(\mu + \frac{1}{h_N} \right), \qquad (43)$$

where h_N satisfies $\exp(-h_N^2/2) = 1/N$, i.e. $h_N = \sqrt{2 \log N}$. Since we have gathered together waves of time series observed at different points (virtual probes shown in Figure 69) over an area, the observed extremes could be larger than those from a time series extracted at only one point in space.

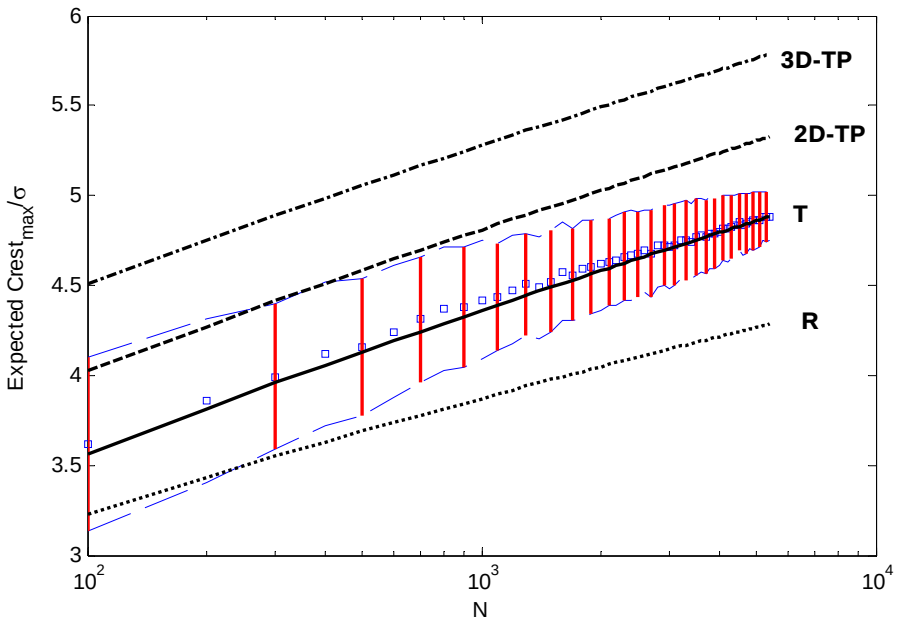

(a)

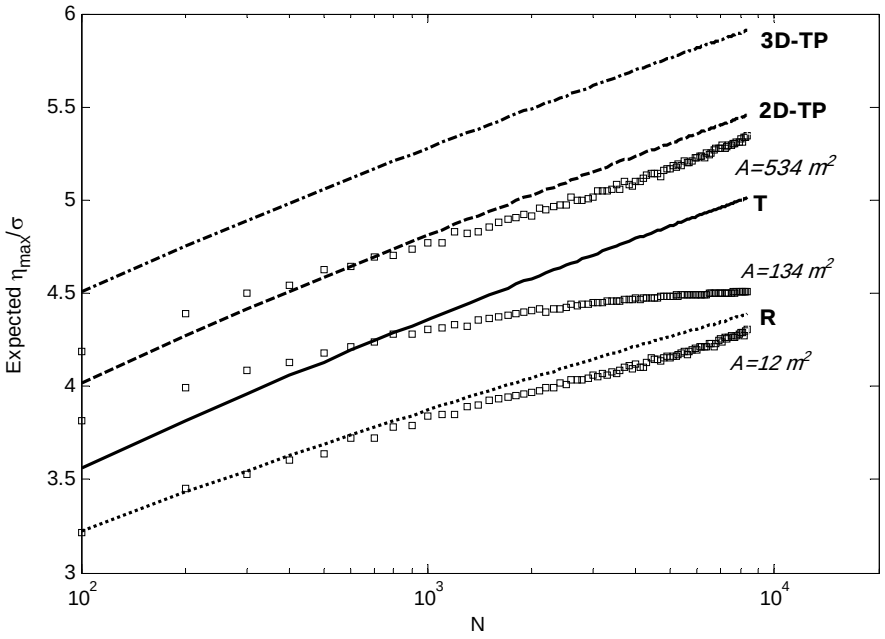

(b)

Figure 78 - Experiment 2: (a) Expected maximum crest height: observed average max crest amplitudes (square dots) and relative stability bands $C(N)\pm\sigma_N$, σ_N being the associated standard deviation, and theoretical R=Rayleigh, T=Tayfun, 2D (3D)-TP=two (three) dimensional Tayfun-Piterbarg models, respectively. (b) Expected maximum of the wave surface as function of the an area A against theoretical models.

Indeed, if we gather together time series from P point-probes, and for each of them we observe N waves, then from (43) it follows that $C_T(N) < C_T(N\,P)$. This is correct as long as waves are short-crested and probes are well separated in space to assure the stochastic independence among measurements at different points in space. To account for spatial effects in our extreme value analysis, we also consider as a reference statistics that of the expected maximum crest height $C_\beta(N)$ of N waves whose parent statistical distribution follows the general law

$$P(h > z) = z_1^\beta \exp(-z_1^2/2), \qquad \beta \geq 1 \tag{44}$$

where the linear amplitude z_1 satisfies the Tayfun quadratic equation (Tayfun 1986)

$$z = z_1 + \frac{\mu}{2} z_1^2 \tag{45}$$

to account for second order nonlinear effects. In this case the expected maximum crest height depends upon the parameter β and it is given by

$$C_\beta(N) = h_N + \frac{\mu}{2} h_N^2 + \gamma_e \frac{1 + \mu\, h_N}{h_N - \beta / h_N}, \tag{46}$$

where h_N satisfies

$$h_N^\beta \exp(-h_N^2/2) = 1/N \tag{47}$$

For $\beta = 0$ the Tayfun model is recovered, as it should be. The two and three dimensional Tayfun-Piterbarg models are obtained for $\beta = 1\ and\ 2$, respectively. Note that

$$C_0(N) < C_1(N) < C_2(N) \tag{48}$$

These three theoretical models are compared against the observed crest heights as shown in Figure 78-a. Even though we have considered an ensemble of wave crests observed at different points in space, the associated expected maximum crest height follows the 1D statistics based on the Tayfun model.

In the following we will investigate the extreme value statistics of the largest amplitude of the wave surface η over a given area A. To do so, consider the sequence of the instantaneous maximum $\xi(t) = \eta_{\max}(t)/\sigma$ of η over the region A sampled at 5 Hz, that is $\{\xi_1, \xi_2, ..., \xi_N\}$. The expected maximum $\xi_{\max}(N)$ is computed according to the Gumbel statistics $C_\beta(N)$ and compared

it against the observed expected maximum amplitude in Figure 78-b. As the area increases, the observations deviate from the 1D Tayfun model approaching the 2D Tayfun-Piterbarg statistics.

The crest-to-trough height H of the largest waves observed at the various different virtual probes do not violate the *Miche-Stokes upper bound* (see Figure 79)

$$\frac{H}{\sigma} \le \frac{2\pi}{7}\frac{\tanh(kd)}{k\sigma} = \frac{L^2}{7L_0\sigma}, \tag{49}$$

where $k = 2\pi / L$, with L as the wavelength of a wave which depends on the water depth via the dispersion relation

$$L = L_0 \tanh\left(2\pi\, d / L\right) \tag{50}$$

L_0 being the deep-water wavelength, i.e. $L_0 = g\,T^2 / 2\pi$, and T the associated wave period.

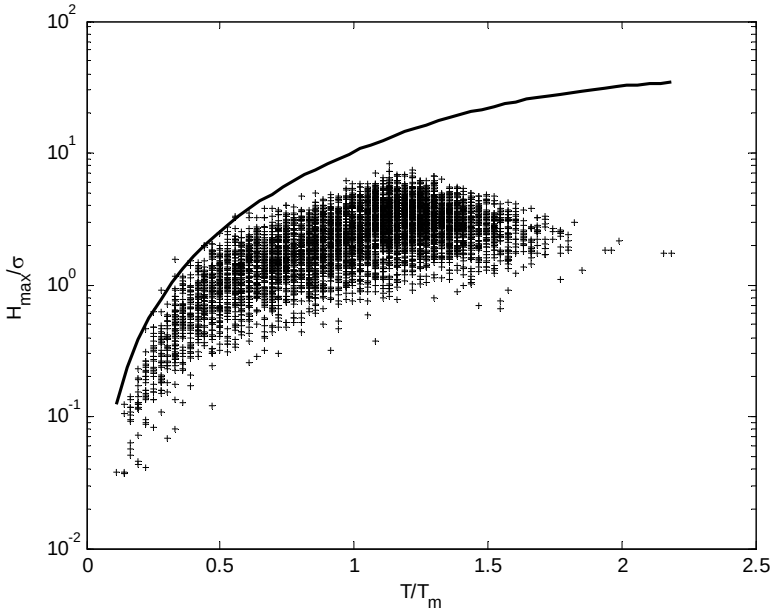

Figure 79 - Experiment 2: Theoretical Miche-Stokes upper bound for the crest-to-trough height H (black line) and observed pairs $\left(T/T_{m,}\, H/\sigma\right)$ (red dots), with σ and T_m as the wave surface standard deviation and mean wave period, respectively.

Consider among the observed waves, those with large crest-to-trough amplitudes $\alpha = H/\sigma >> 1$. The shape of these large waves tends, for $\alpha >> 1$, to the deterministic form

$$<\eta(t)\,|\,\alpha>= \frac{\alpha}{2}\frac{\psi(t)-\psi(t-T^*)}{1-\psi(T^*)} + \frac{\mu\alpha^2}{8}\left\{\left[\frac{\psi(t)-\psi(t-T^*)}{1-\psi(T^*)}\right]^2 - \left[\frac{\hat{\psi}(t)-\hat{\psi}(t-T^*)}{1-\psi(T^*)}\right]^2\right\}, \tag{51}$$

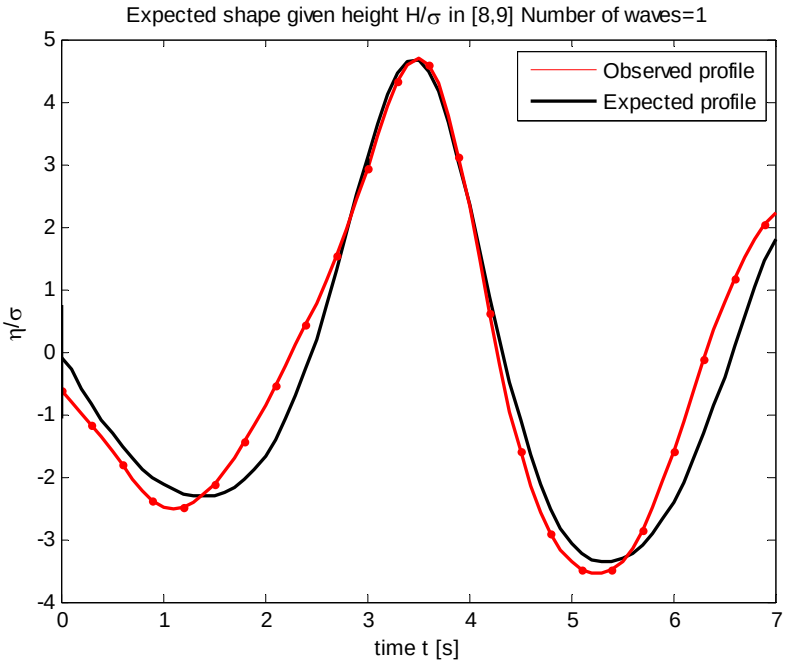

Figure 80 - Experiment 2: Observed shape of large waves (red line) given the crest-to-trough height H in [6σ, 7σ] and respective stability bands, and theoretical expected wave profile of Eq. 51 (black line).

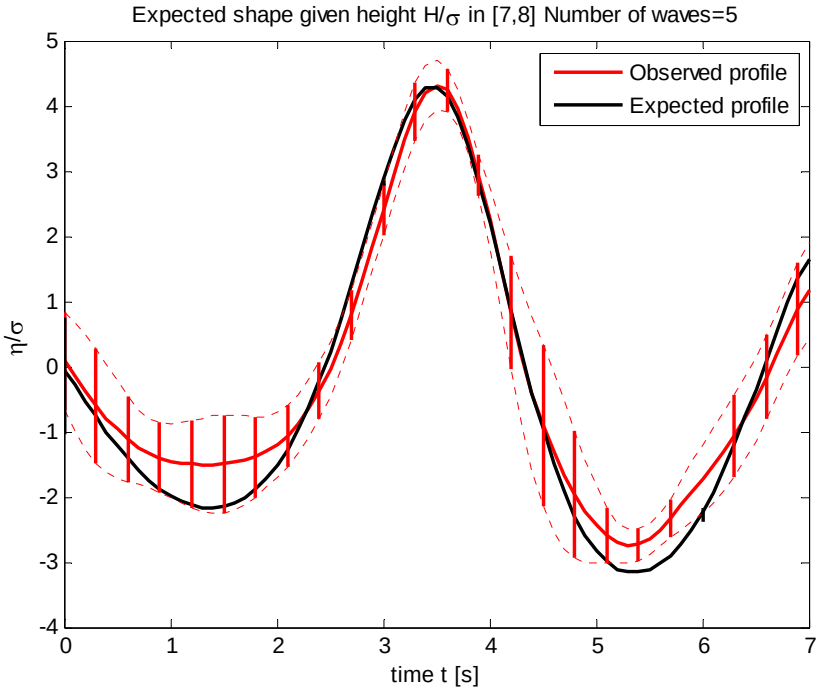

Figure 81 - Experiment 2: Observed shape of large waves (red line) given the crest-to-trough height H in [7σ, 8σ] and respective stability bands, and theoretical expected wave profile of Eq. 51 (black line).

where $\psi(t)$ is the normalized wave covariance given by

$$\psi(t) = \frac{<\eta(\tau)\eta(\tau+t)>}{\sigma^2}, \tag{52}$$

$\hat{\psi}(t)$ its Hilbert transform, and T^* is the abscissa of the first absolute minimum of ψ (Boccotti 2000). Further, if we define C and T as the crest and trough amplitudes of the same wave, given $\alpha >> 1$, the conditional ratios C/T and T/C are given, respectively, by

$$\{C/T \mid H = \alpha\} = \frac{1+2\gamma Z}{1-2\gamma Z} \cdot \frac{1+\mu\alpha(1+2\gamma Z)/4}{1-\mu\alpha(1-2\gamma Z)/4} \tag{53}$$

and

$$\{T/C \mid H = \alpha\} = \frac{1+2\gamma Z}{1-2\gamma Z} \cdot \frac{1-\mu\alpha(1+2\gamma Z)/4}{1+\mu\alpha(1-2\gamma Z)/4} \tag{54}$$

where Z is Gaussian with mean zero and unit variance and

$$\gamma = \frac{1}{\alpha}\sqrt{\frac{1+\psi(T^*)}{2}} \tag{55}$$

For Acqua Alta data we set $\mu = \mu_m = 0.09, \quad \psi(T^*) = -0.66$. Figures 80-81 show a comparison between the observed shape of large waves and the respective theoretical expected wave profiles. The agreement with theory is good. Further, Figures 82-84 show that the observed conditional ratios 53-54 agree well with the associated theoretical expected values. Consider now among the observed waves, those with large crest amplitudes $\xi = h/\sigma >> 1$. Their shape, according to the theory of quasi tends to the form determinism (Lindgren 1970,1972; Boccotti, 2000, Tayfun and Fedele 2007b, Fedele & Tayfun 2009)

$$<\eta(t) \mid \eta(0) = \xi >= \xi_1\psi(t) + \frac{\mu\xi_1^2}{2}(\psi^2(t) - \hat{\psi}^2(t)), \tag{56}$$

where

$$\xi = \xi_1 + \frac{\mu\xi_1^2}{2} \tag{57}$$

Figure 85 shows a comparison between the observed shape of waves with large crests and the respective theoretical expected wave profiles. The agreement with theory is good.

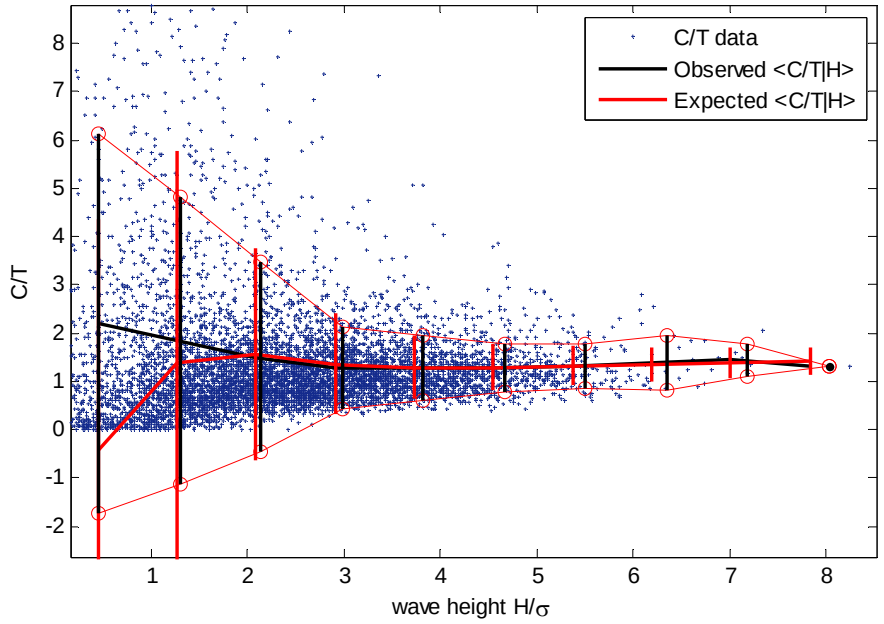

Figure 82 - Experiment 2: Observed crest-to-trough ratio (red line) given the crest-to-trough height H and respective stability bands, and the theoretical expected conditional ratio of Eq. 53 (black line) .

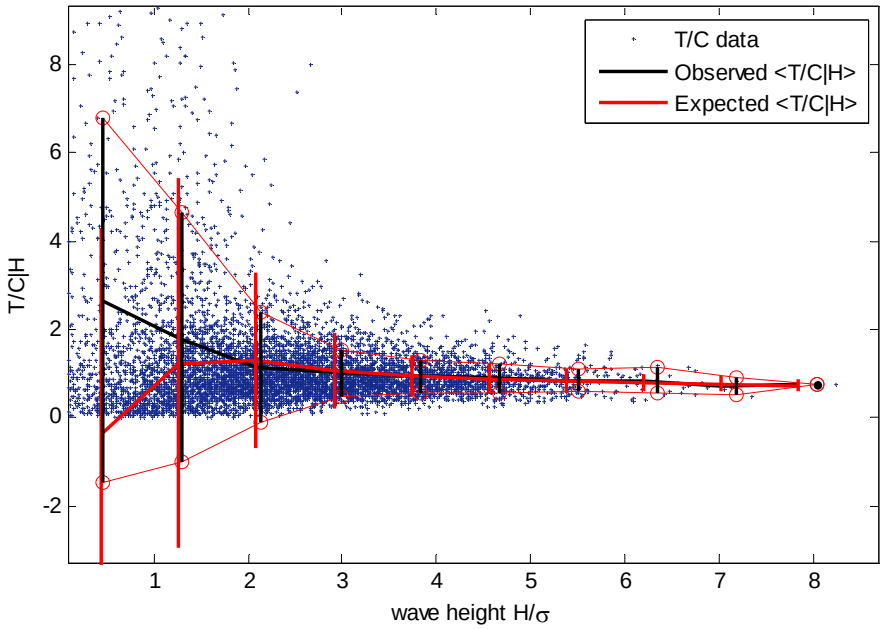

Figure 83 - Experiment 2: Observed trough-to-ratio (red line) given the crest-to-trough height H and respective stability bands, and the theoretical expected conditional ratio of Eq. 54 (black line) .

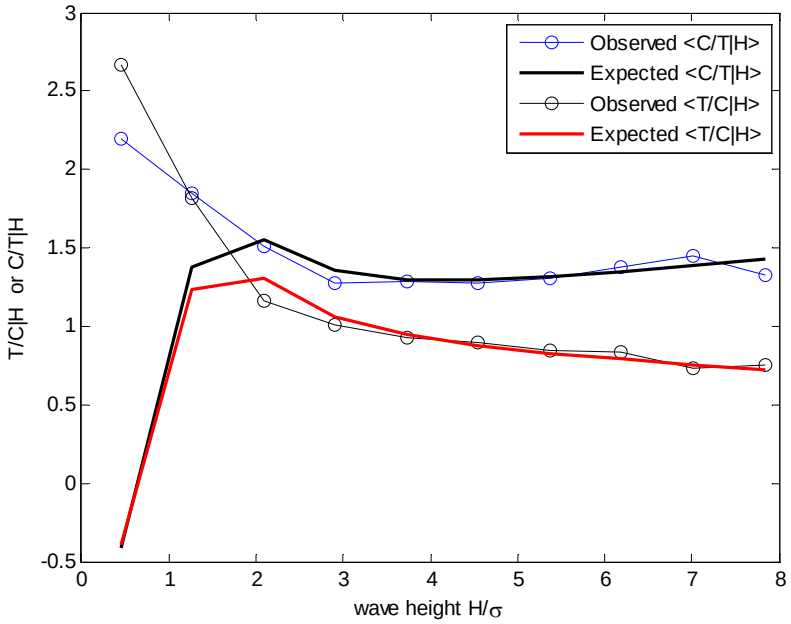

Figure 84 - Experiment 2: Observed conditional averages of C/T (blue dotted line) and of T/C (black dotted line) given the crest-to-trough height H and the associated theoretical expected values (red and blue tick lines, respectively).

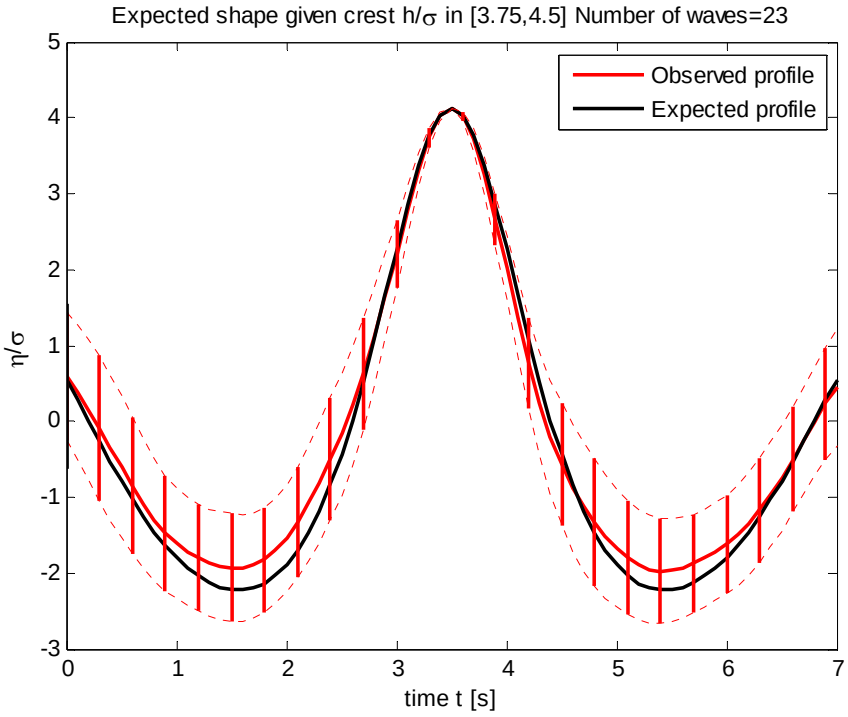

Figure 85 - Experiment 2: Observed shape of large waves (red line) given the crest amplitude h in [3.75σ, 4.5σ] and respective stability bands, and theoretical expected wave profile (black line).

3.3.1. Wave Crests over an Area

A total of 16736 maps (i.e. 1673.6 s of 3D data) of the sea surface at 0.1 second intervals have been processed. The horizontal resolution of the maps is 0.05 m. To make the processing more manageable, we truncated the data to every fifth point, giving a horizontal resolution of 0.25 m. This process resulted in 15579 good grid points. The average significant wave height was 1.14 m. The mean wave period is T_1 = 3.96 sec and the zero crossing period is T_Z = 3.33 sec.

Figure 86 shows the average power spectrum over the truncated grid points. The high frequency tail of the spectrum follows an f^{-4} slope from near the peak to 1 Hz. Above 1 Hz, the measured spectrum deviates from the expected tail behavior, probably because of noise. In order to eliminate contamination from this noise in the crest height statistics, we made two low-pass versions of the data, filtered 1 Hz and 2 Hz.

Figure 87 compares the distribution of measured significant wave heights with the distribution resulting from 100 linear simulations of the average measured directional spectrum. The simulated distribution actually spreads over a larger range than the measured distribution.

Figure 88 shows the maximum crest height recorded at each of the 15579 grid points, after the 1 Hz low pass filter

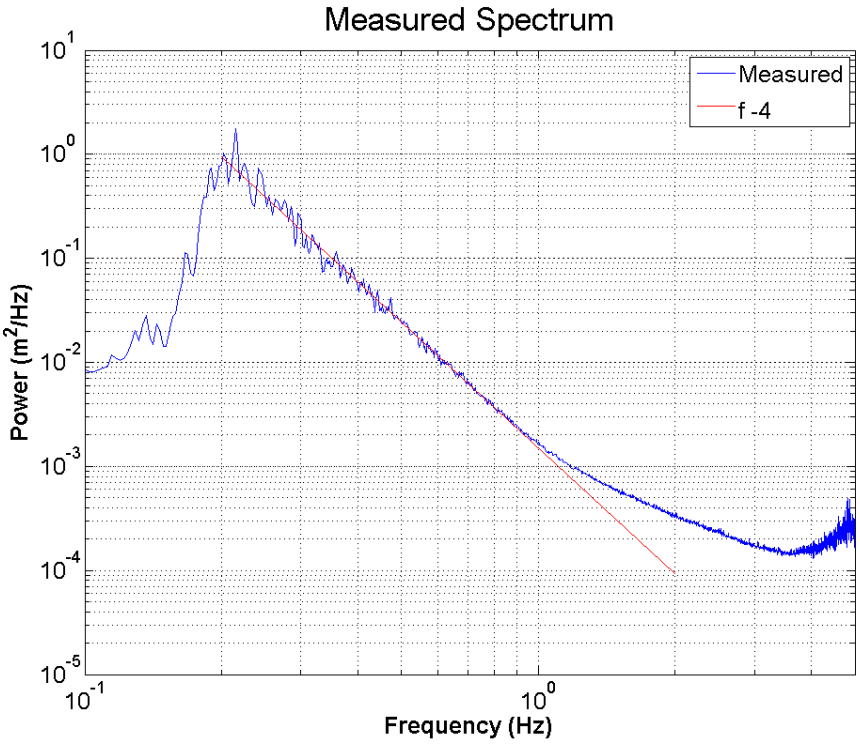

Figure 86 - Experiment 2: Average power spectrum.

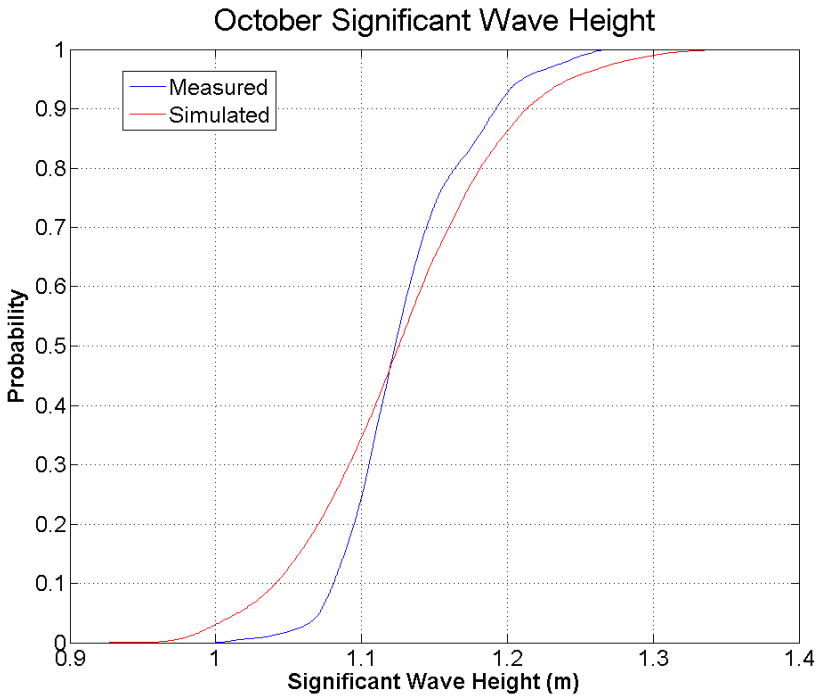

Figure 87 - Experiment 2: Probability distribution of significant wave heights over the measured area.

Area	Location	Number Points	Area (m^2)
All	Whole Grid	15,579	966
A	X>5 & Y>33	3952	247
B	X<5 & Y>33	3770	229
C	X>5 & Y<33	3811	238
D	X<5 & Y<33	4096	253

Table 14 - Experiment 2. Area divisions for crest height calculations in Table 15.

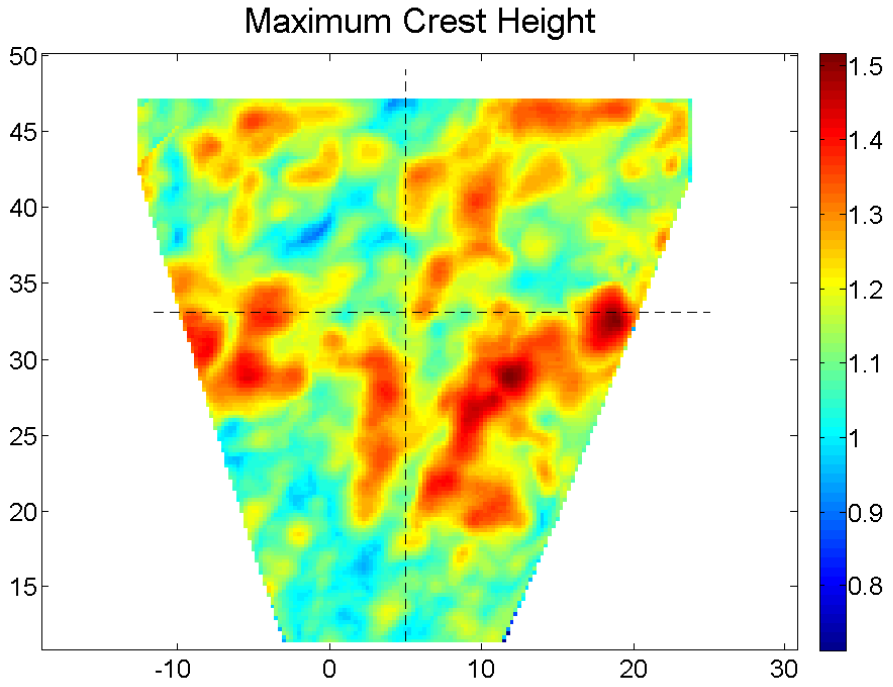

Figure 88 - Experiment 2: Maximum crest heights over the measurement area. Areas A, B, C, and D are approximately ¼ of the whole area and their boundaries (dashed lines) are listed in Table (Data filtered at 1 Hz).

Table 14 compares the mean of the maximum crest heights over the area with the maximum of the maximum crest heights over the area for several divisions of the data. The areas in column 1 are described in Table . "All" means the entire area with good measurements. Areas A, B, C, and D are approximately ¼ of the whole area. Their boundaries are listed in Table and shown as the dashed lines in Figure 88. The entire filtered time series is 1638.4 sec long. Time 1 is the first 409.6 sec of the record and Times 2 – 4 are the succeeding 409.6 sec divisions of the data.

The mean in column 3 is the average over grid points in each area of the maximum crest heights recorded during the time interval. The maximum in column 4 is the maximum crest height over all the grid points during the time interval. The ratio in column 5 is the ratio between columns 4 and 3. There is considerable variability between the ratios for different time intervals and different quadrants. We can however observe that the ratios are larger for the entire area than for the quadrants and larger for the short time intervals than for the entire record.

Area	Time	Mean(Max)	Max(Max)	**Ratio**
All	All	1.178	1.515	1.286
All	1	1.086	1.515	1.395
All	2	1.067	1.507	1.412
All	3	1.066	1.470	1.379
All	4	0.956	1.343	1.410
A	All	1.191	1.472	1.237
B	All	1.147	1.370	1.195
C	All	1.219	1.515	1.243
D	All	1.157	1.431	1.237
A	1	1.109	1.362	1.228
B	1	1.003	1.290	1.286
C	1	1.150	1.515	1.318
D	1	1.078	1.393	1.292
A	2	1.041	1.472	1.415
B	2	1.094	1.370	1.252
C	2	1.024	1.507	1.471
D	2	1.042	1.431	1.373
A	3	1.101	1.370	1.244
B	3	1.046	1.282	1.225
C	3	1.133	1.470	1.298
D	3	1.047	1.422	1.358
A	4	1.034	1.264	1.223
B	4	0.910	1.329	1.461
C	4	0.963	1.348	1.400
D	4	0.886	1.238	1.398

Table 14 - Experiment 2: Mean and maximum crest heights over the measured area for data low pass filtered at 1 Hz.

Table 15 compares the mean and maximum crest height for the measurements low pass filtered at 2 Hz. The means, maxima, and ratios are all higher than for the 1 Hz filtered measurements.

We made linear simulations based on the measured power spectrum and directional spreading function. Forristall (2006) showed that linear simulations produced the same ratios as second order simulations and are much faster. Each simulation produced 4096 samples at 10 Hz for each measurement grid point. A total of 100 simulations were made.

Area	Time	Mean(Max)	Max(Max)	Ratio
All	All	1.243	1.739	**1.399**
All	1	1.135	1.539	**1.355**
All	2	1.119	1.739	**1.554**
All	3	1.117	1.585	**1.419**
All	4	1.005	1.491	**1.484**
A	All	1.268	1.739	**1.371**
B	All	1.215	1.539	**1.267**
C	All	1.272	1.621	**1.275**
D	All	1.204	1.513	**1.257**
A	1	1.176	1.474	**1.253**
B	1	1.057	1.539	**1.455**
C	1	1.188	1.527	**1.286**
D	1	1.101	1.454	**1.321**
A	2	1.103	1.739	**1.576**
B	2	1.150	1.448	**1.259**
C	2	1.061	1.621	**1.529**
D	2	1.090	1.512	**1.387**
A	3	1.165	1.503	**1.290**
B	3	1.097	1.373	**1.252**
C	3	1.175	1.585	**1.349**
D	3	1.086	1.513	**1.393**
A	4	1.098	1.327	**1.209**
B	4	0.970	1.491	**1.539**
C	4	0.994	1.476	**1.485**
D	**4**	**0.916**	**1.365**	**1.490**

Table 15 - Experiment 2. Mean and maximum crest heights over the measured area for data low pass filtered at 2 Hz.

Means and maxima over different areas and time intervals were then found in the same way as for the measured data. Ratios between the mean maximum and the maximum over the entire area were averaged over the number of simulations. Table 16 lists the ratios for the 1 Hz filtered spectrum and Table 17 lists the ratios for the 2 Hz filtered spectrum. There is much less variability in the simulations than in the measurements. The same general features are evident. The ratios are higher for the larger area, for shorter time intervals, and for the 2 Hz filtered spectrum.

Area	Time (sec)	Ratio
All	1638.4	**1.326**
All	409.6	**1.390**
A	1638.4	**1.249**
B	1638.4	**1.229**
C	1638.4	**1.234**
D	1638.4	**1.248**
A	409.6	**1.296**
B	409.6	**1.277**
C	409.6	**1.277**
D	**409.6**	**1.292**

Table 16 - Experiment 2. Ratios between maximum and mean crest heights over simulated areas for the 1 Hz filtered spectrum.

Area	Time (sec)	Ratio
All	1638.4	**1.347**
All	409.6	**1.413**
A	1638.4	**1.273**
B	1638.4	**1.250**
C	1638.4	**1.253**
D	1638.4	**1.269**
A	409.6	**1.318**
B	409.6	**1.301**
C	409.6	**1.299**
D	409.6	**1.316**

Table 17 - Experiment 2. Ratios between maximum and mean crest heights over simulated areas for the 2 Hz filtered spectrum.

Piterbarg (1996) developed a mathematical theory for the maximum of a Gaussian distribution over an *n*-dimensional space and Krogstad et al. (2004) applied the theory to ocean waves. The expected value of the maximum over an area is

$$E(\eta_{\max}) = h_N + 0.5772 / h_N \tag{58}$$

where

$$h_N = \left[2\log N + 2\log(2\log N)\right]^{1/2} \tag{59}$$

N is the "equivalent number of waves". From simulations, Forristall (2006) found that for square areas less than one mean wavelength on a side, the equivalent number of waves is well approximated by

$$N = 2\frac{L}{\lambda_1}\frac{T}{T_z} \tag{60}$$

where L is the square root of the area, T is the time interval, λ_1 is the wave length corresponding to the mean wave period, and T_Z is the zero crossing wave period.

Evaluating equations (58), (59), and (60) for the parameters of the measured spectrum gives the ratios listed in Table 18. These ratios are smaller than those from the measurements or simulations.

Area	Time (sec)	Ratio
All	1638.4	**1.236**
All	409.6	**1.274**
A	1638.4	**1.189**
B	1638.4	**1.186**
C	1638.4	**1.187**
D	1638.4	**1.190**
A	409.6	**1.214**
B	409.6	**1.210**
C	409.6	**1.212**
D	**409.6**	**1.215**

Table 18 - Experiment 2. Ratios between maximum and mean crest heights over simulated areas calculated from equations (58), (59), and (60).

Table 19 and Table 20 compare the ratios of the maximum crest height over an area to the mean of the maxima at each grid point for the measurements simulations and simplified theory. Table 7 is for the data and spectrum low pass filtered at 1 Hz and Table 20 is for the data and spectrum low pass filtered at 2 Hz. The ratios from each 409.6 sec time interval should be the same on average. The ratios for the four quadrants should also be the same on average because they are nearly the same size. Therefore the ratios for the four time intervals and fours quadrants were averaged for these tables.

Area	Time (sec)	Measured	Simulated	Theory
All	1638.4	1.286	1.326	**1.236**
All	409.6	1.399	1.390	**1.274**
Quadrant	1638.4	1.237	1.240	**1.188**
Quadrant	**409.6**	**1.328**	**1.286**	**1.213**

Table 19 - Experiment 2. Comparison of measured, simulated and theoretical ratios of crest height over an area to the mean of the maxima at each grid point for the 1 Hz filtered data.

Area	Time (sec)	Measured	Simulated	Theory
All	1638.4	1.399	1.347	**1.236**
All	409.6	1.453	1.413	**1.274**
Quadrant	1638.4	1.292	1.261	**1.188**
Quadrant	**409.6**	**1.379**	**1.309**	**1.213**

Table 20 - Experiment 2. Comparison of measured, simulated and theoretical ratios of crest height over an area to the mean of the maxima at each grid point for the 2 Hz filtered data.

The simulated ratios agree very well with the measured ratios for the data filtered at 1 Hz. Some are slightly lower and some are higher, as would be expected from statistical variability. The simulated ratios are slightly lower than the measured ratios for the data filtered at 2 Hz. We believe this difference is because the measurements include some noise in the range between 1 Hz and 2 Hz, as illustrated in the spectrum in Figure .

The theoretical ratios are lower than the measured or simulated ratios. The fundamental theory expressed in equations (58) and (59) is quite sound. The problem is to find the equivalent number of waves for the spectrum and area of interest. Equation (60) was developed empirically from simulations of a Jonswap spectrum over a square area. The measured area is not square and the

mean wave direction is at about a 45° angle to the Y-axis. In addition, Equation (60) was found to work best for square areas with side lengths less than the mean wave length. For the whole measured grid, the equivalent side length is about 31 m while the mean wave length is about 24 m. We conclude that linear simulations can accurately predict the maximum crest height over an area. On the other hand, empirical Equation (60) may not be accurate for cases that differ from a Jonswap spectrum over a relatively small square area.

3.4. EXPERIMENT 3: 2010 MARCH 09, 1120 UTC ÷ 1150 UTC

3.4.1. Stereo cameras setup and 3D reconstruction

A sketch of WASS left and right camera field of view is shown in Figure 89, and an example of stereo pairs (snapshots of the water surface at the same instant of time) is shown in Figure 90. Figures 91-92 illustrate various images framed by the right camera that provide an idea of the wave conditions during Experiment 3. An example of stereo correspondences (i.e. corresponding pixels in left and right cameras of the same point in the world reference system) are shown in Figures 93-94. Here, both the images are corrected for lens aberration and also stereo rectified. Since the imaging set up is discrete in nature, the image coordinates of each pixel can be assumed to suffer from quantization errors of up to ± 1/2 pixel for each camera. The quantization error distribution of the final 3-D points in the x, y and z directions after stereo triangulation and the associated exceedance probability of its absolute value are shown in Figure 95. The max and mean quantization errors are shown in Figure 96. Figure 97 shows the reconstructed 3D points in the left camera reference system, obtained after triangulation of stereo pairs (corresponding pixels in left and right cameras images). Successive snapshots of the 3D reconstruction of the water surface in time are shown in Figure 98, and Figure 99 reports time series of the wave displacements extracted at given virtual point probes. Finally, Figure 100 shows the variability of the significant wave height at Acqua Alta during Experiment 3.

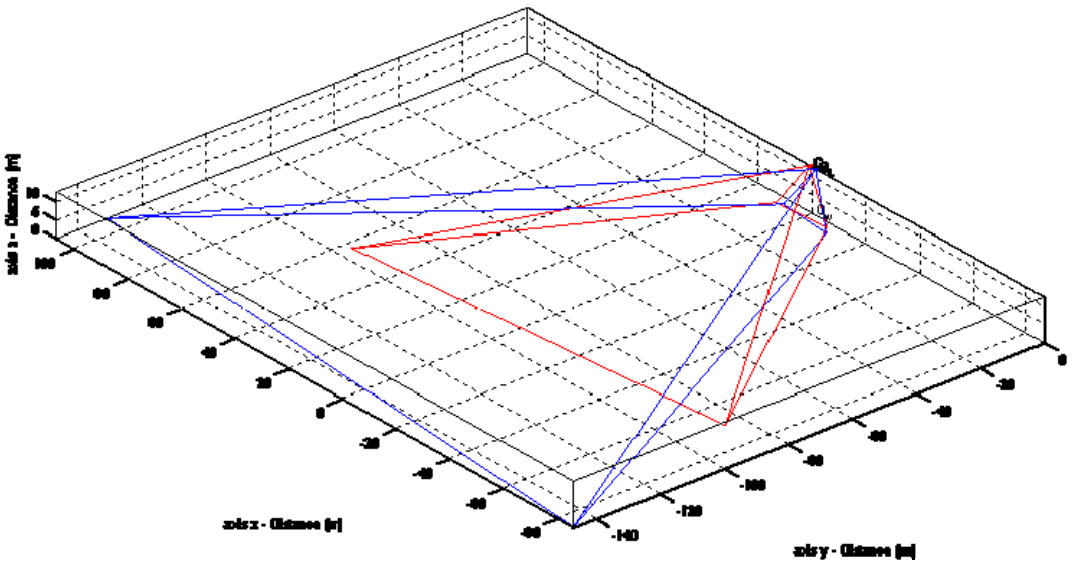

Figure 89 - Sketch of WASS installation for Experiment 3 in march 09, 2010. Fields of View of Left (blue lines) and right (red lines) cameras. Cameras are positioned at approximately 12.5 m above the mean sea level (z = 0).

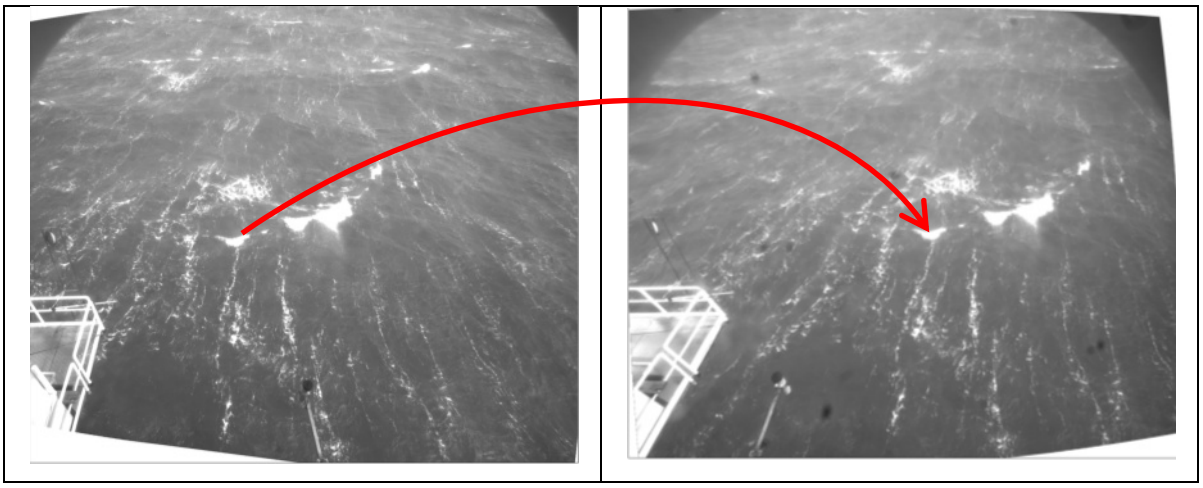

Figure 90 – Experiment 3: example of stereo pair snapshots, left and right camera images before lens aberration correction and stereo rectification. Arrows points at corresponding sea points in the two frames

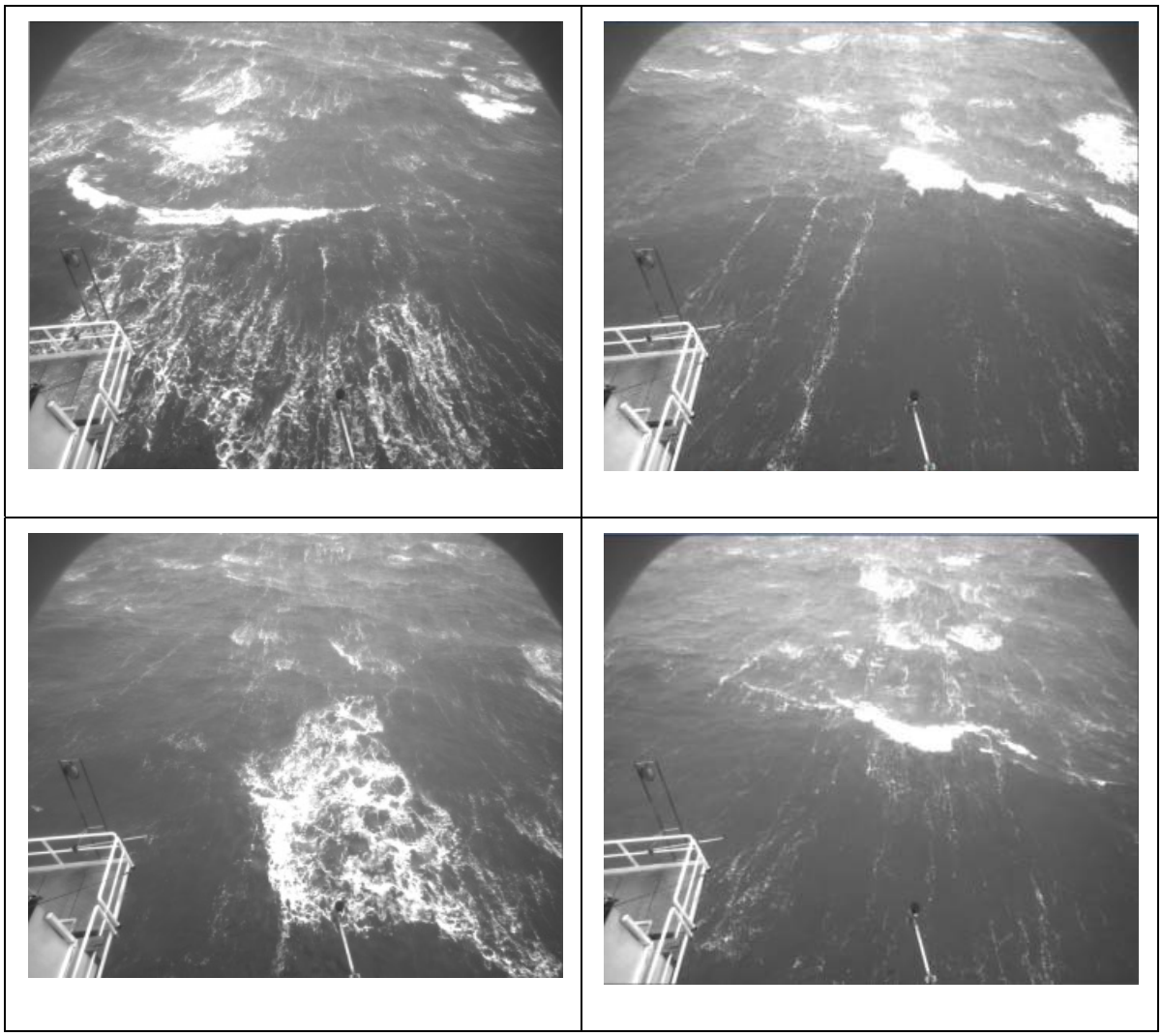

Figure 91 - Experiment 3: example of images framed by right camera.

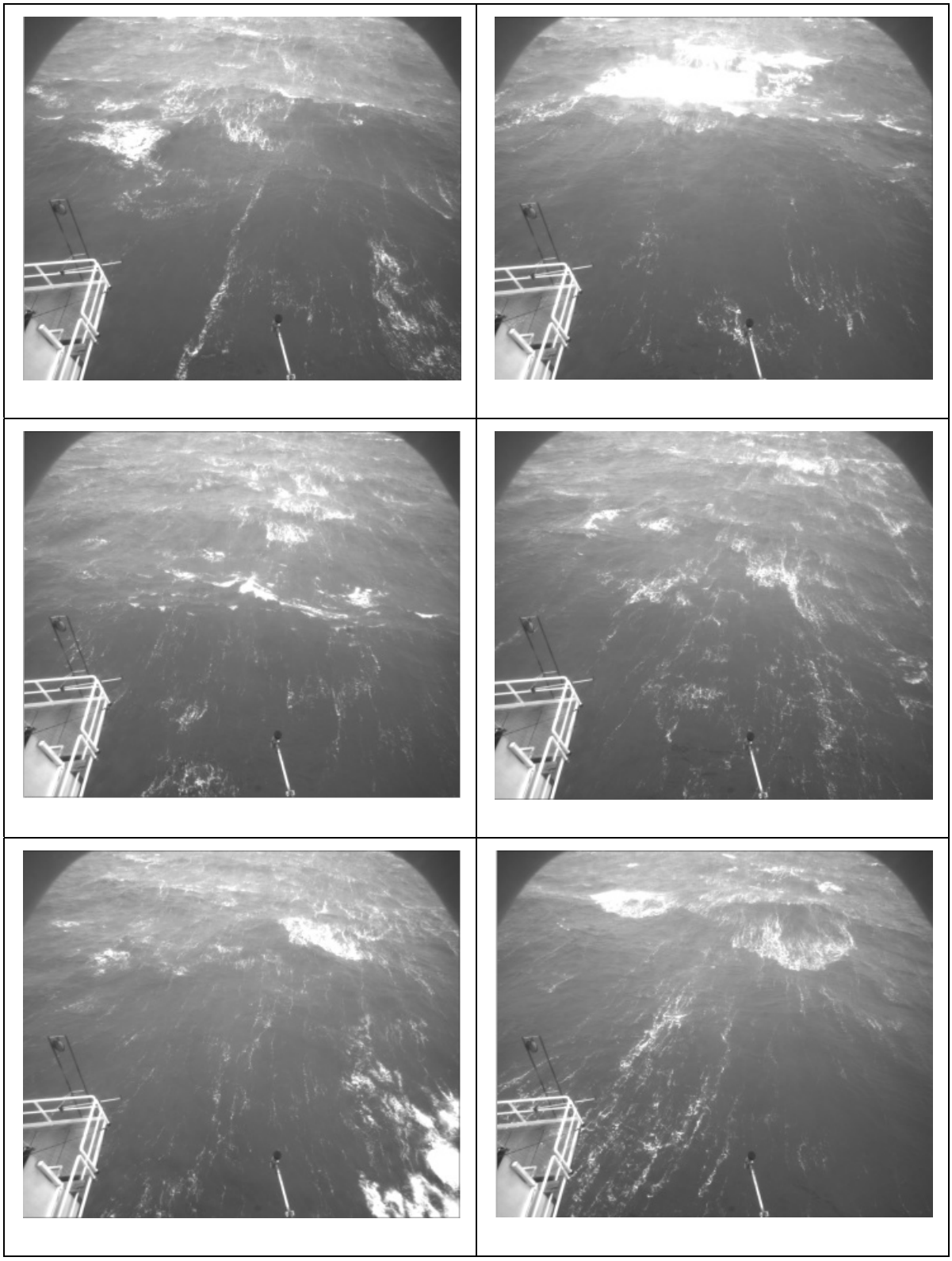

Figure 92 - Experiment 3: example of images framed by right camera.

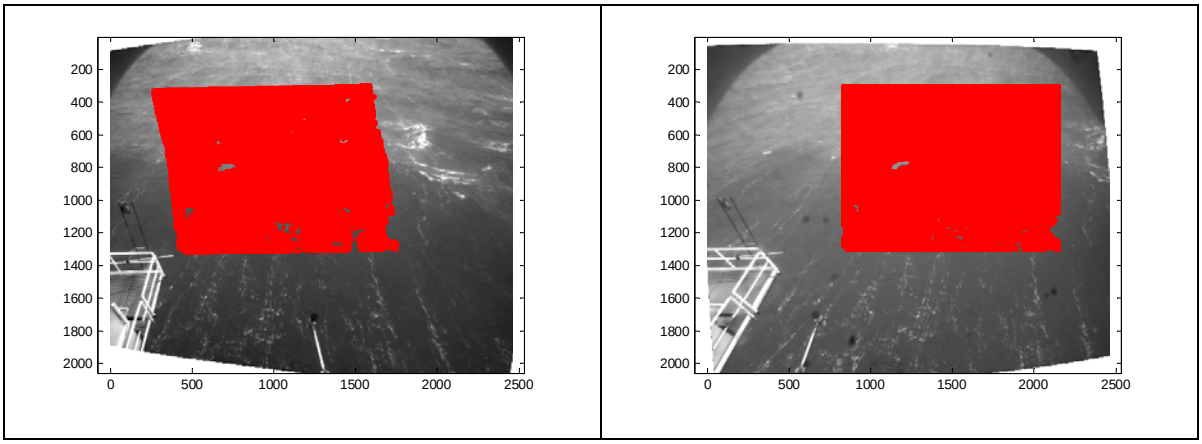

Figure 93 – Experiment 3: example of stereo correspondences. Red points in Left and Right images are corresponding points of the same sea surface pixel. Images are corrected for lens aberration and stereo rectified.

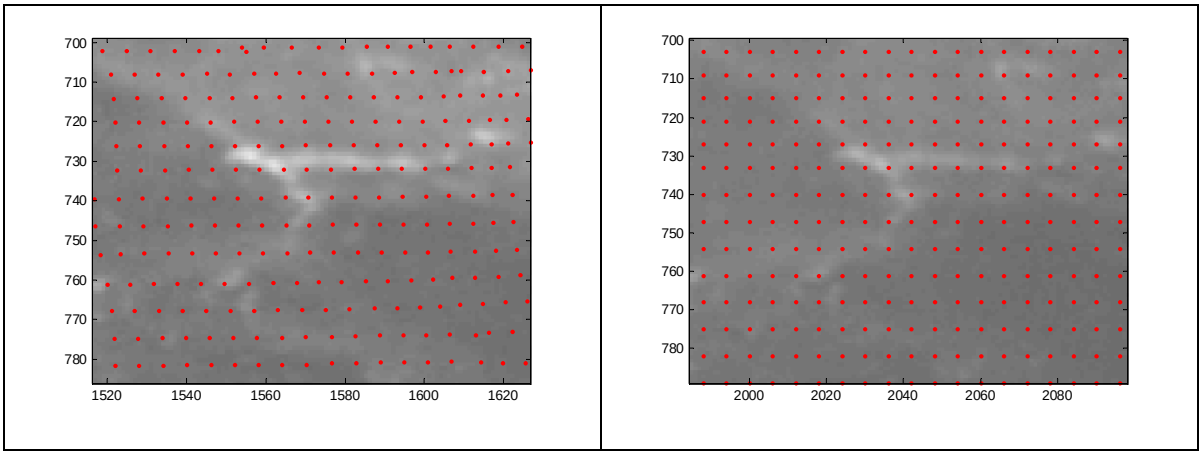

Figure 94 - Experiment 3: example of stereo correspondences. Red points in Left and Right images are corresponding points of the same sea surface 3D point.

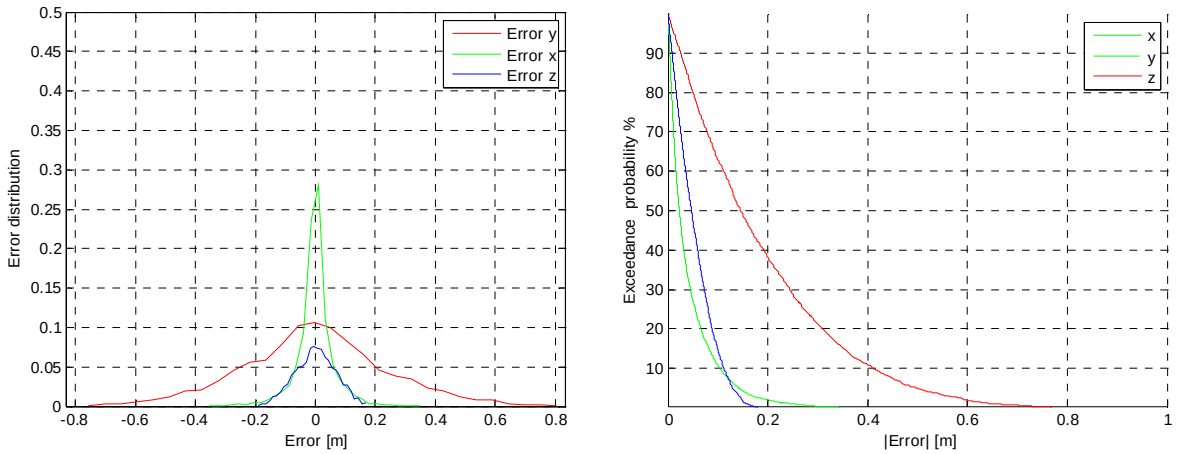

Figure 95 - Experiment 3: (Left) Distribution of quantization errors and (Right) exceedance probability of their absolute values along the x,y, and z axes. Errors refer to pixel-to-pixel triangulation of red pixels of Figure 93 without any subpixel detection. (x,y,z axes as in Figure 89).

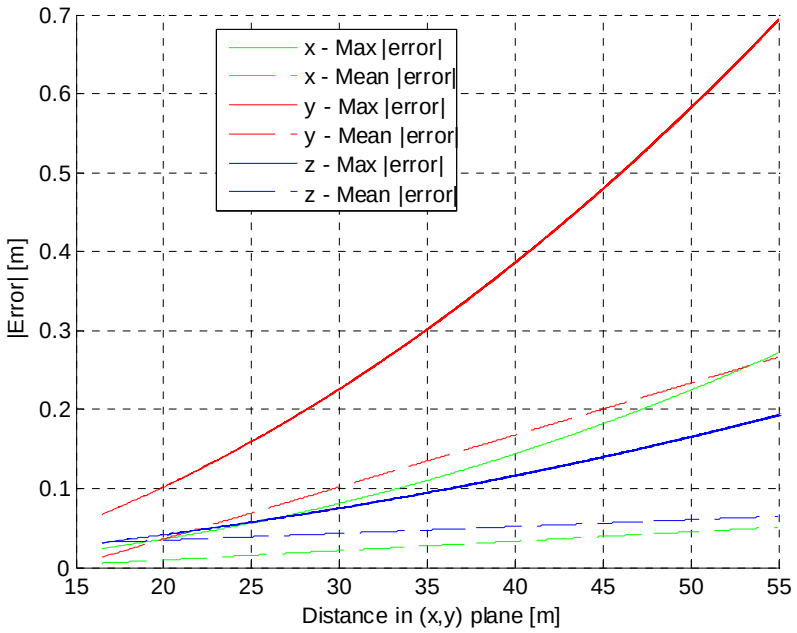

Figure 96 – Experiment 3: Max and mean absolute quantization errors as function of the horizontal distance from the cameras after stereo triangulation (x,y, z axes as in Figure 89).

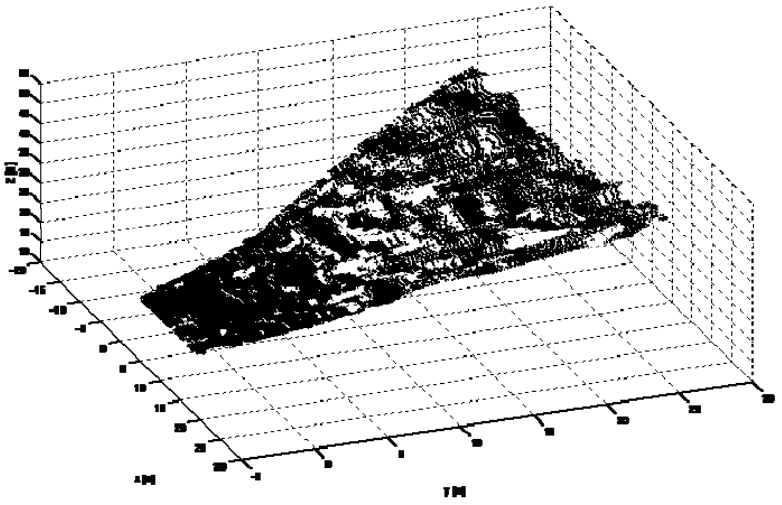

Figure 97 - Experiment 3: 3D points in Left camera reference system. Z is the distance of each 3D point from the CCD principal point.

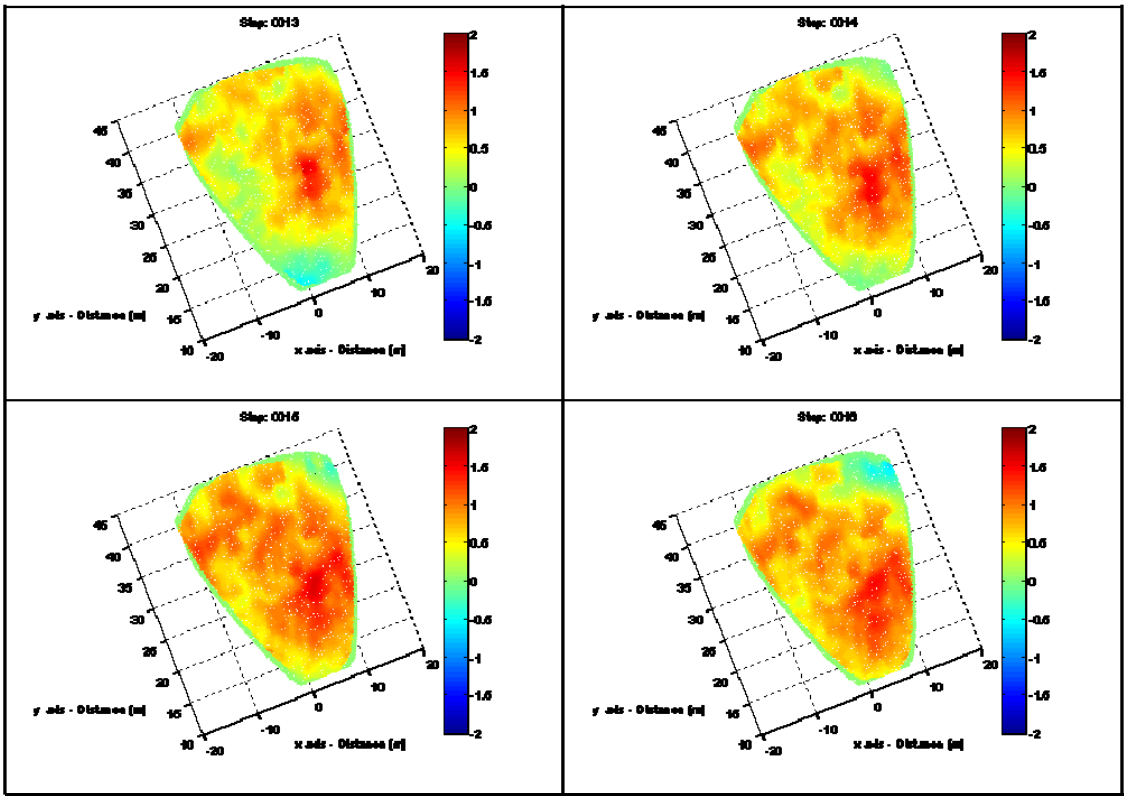

Figure 98 – Experiment 3: example of 3D reconstruction of the water surface shape in time. Time distance between consecutive images (from left to right, from top to bottom) is 0.2 s.

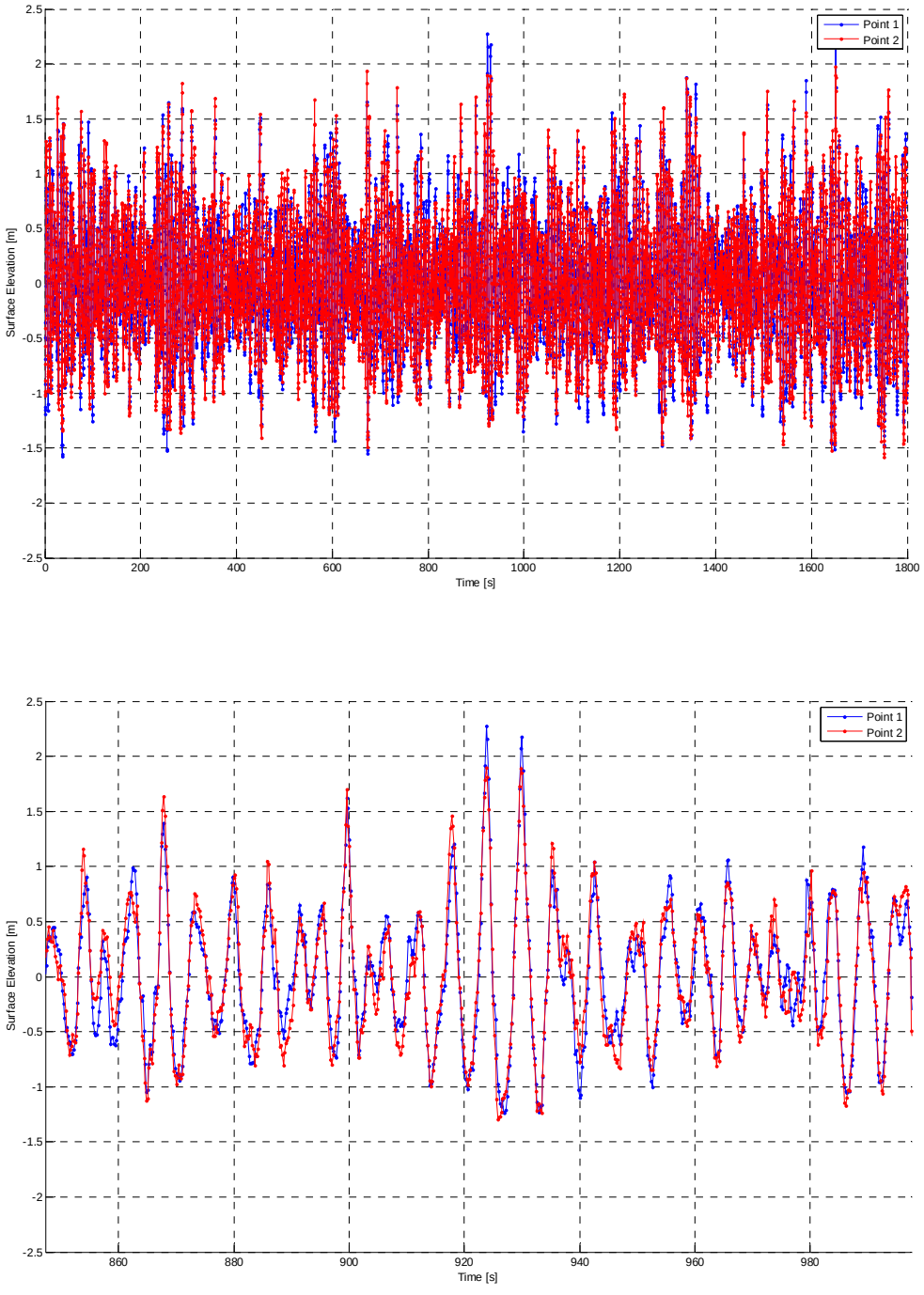

Figure 99 – Experiment 3: (Top) wave surface elevation time series extracted from stereo data at points 1 and 2 located at (x,y)=(3.0 m, 28.1m) and (x,y)=(5.0 m, 28.1m) respectively. (Bottom) Short time series observed at the same points.

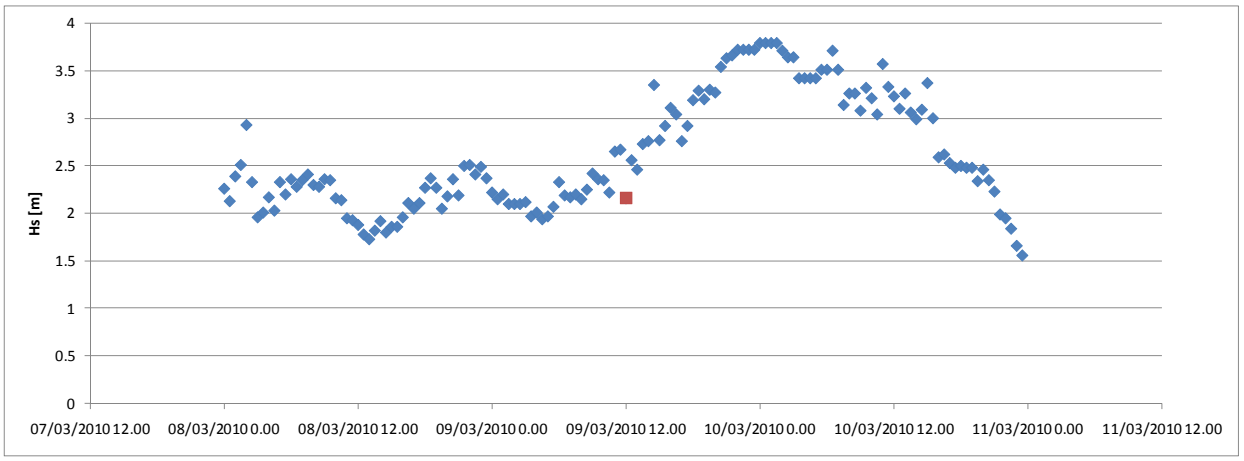

Figure 100 – Experiment 3: Significant wave heights Hs [m] variability at Acqua Alta on June 05, 2009. Red dot denotes time while WASS was operational.

3.4.2. Wave spectra

Consider the time series extracted at several points in the 3D domain as shown in Figure 101. The statistics of wave and crest heights can be computed by analyzing the ensemble of the extracted time series for a total number of roughly 6000 waves. The average significant wave height H_s = 2.13 m, and the mean wave period is T_m=4.81 s.

White capping was observed in processed video data. The average spectrum S(f), mean of the observed spectra at the virtual point probes of Figure , decays as f^4 in agreement with Zakharov's theory (Zakharov 1999). We noticed noise above f_{max}=1.0 Hz, and thus ignored the energy content above it with variations less than 0.4% in the wave variance.

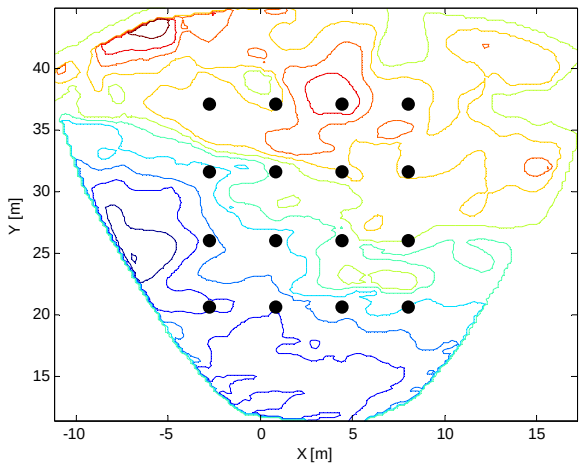

Figure 101 – Experiment 3: Location of the virtual probes used to calculate wave elevation spectra.

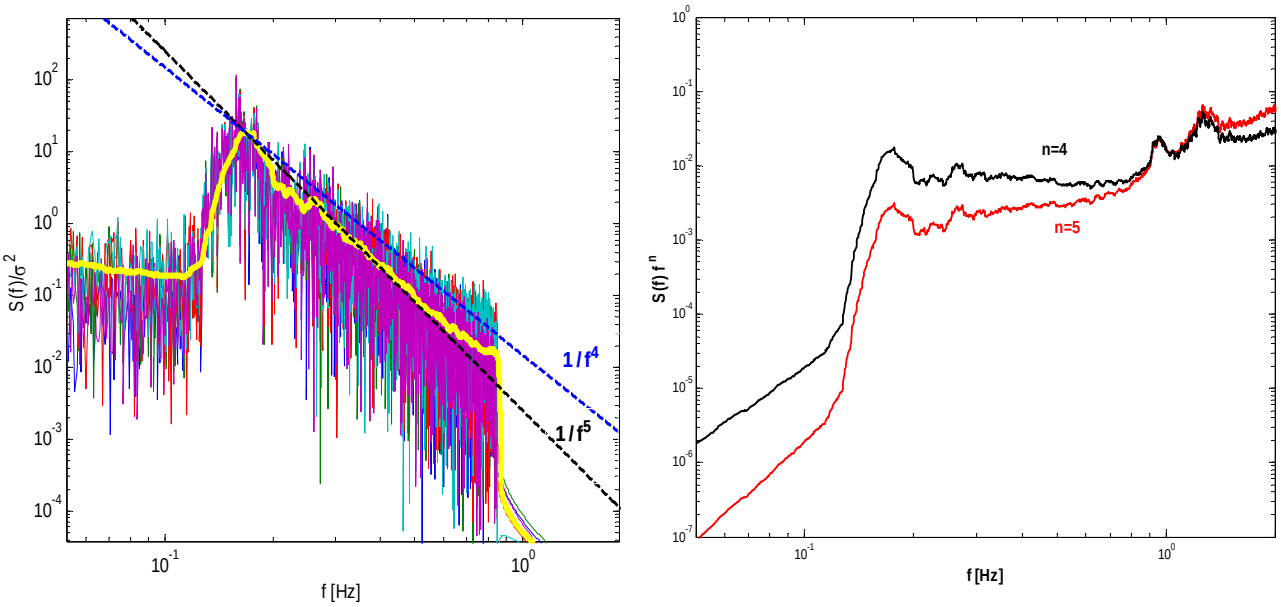

Figure 102 - Experiment 3. (Left) Average frequency spectrum of the observed spectra at all the virtual probes of Figure and (Right) average saturation spectra $S(f)f^n$ for n=4,5. Nyquist frequency = 2.5 Hz. Spectral resolution Df = 5.6 x 10^{-4} Hz (equal to 1/Time series duration = 1/1800 s).

The estimation of the omnidirectional spectrum $S(k)$ proceeds by averaging all the instantaneous directional spectra $S(k_x,k_y)$ of the wave surface observed over the rectangular area indicated in Figure 103.

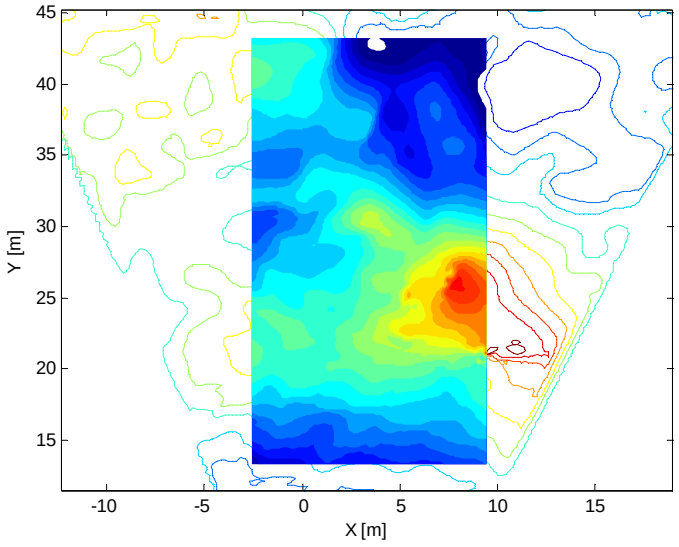

Figure 103 - Experiment 3. Selected region for directional spectra computations.

The resulting average directional spectrum is shown in Figure 104. By numerical integration over all the directions, we obtain the omni S(k) which is shown in Figure 105. In agreement with Zakahrov's theory, the spectrum tail decays as $k^{-2.5}$ (Zakharov 1999).

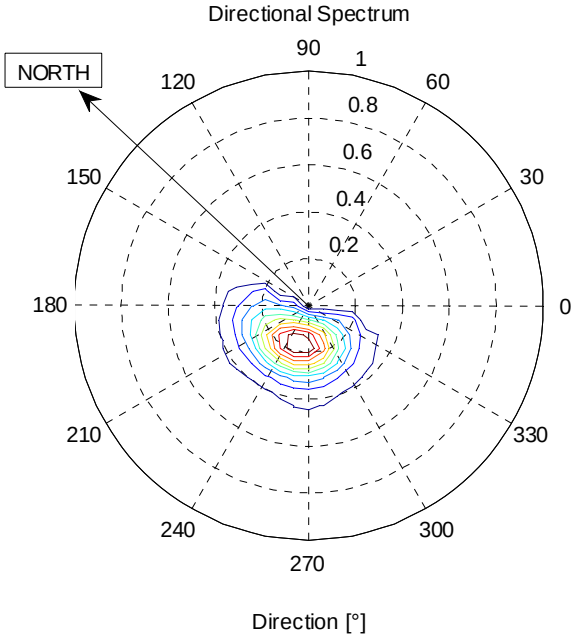

Figure 104 – Experiment 3: 2D wavenumber spectra from Fourier transform. Mean wavenumber spectrum over 9000 3D sea surface maps. Nyquist wavenumber: [k_x. k_y]max = [15.71 rad/m, 15.71 rad/m]. Spectral Resolution: [k_x. k_y] = [0.5 rad/m, 0.2 rad/m]. North direction at 46.4° counterclockwise with respect to y axis.

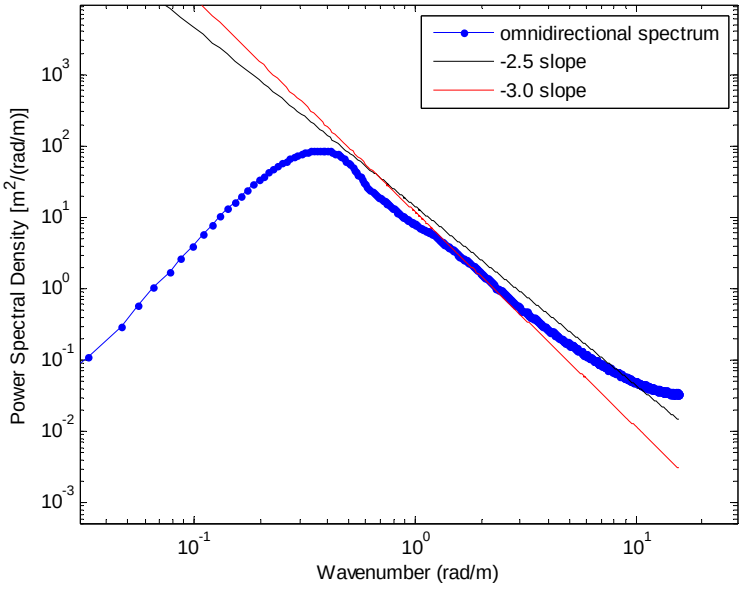

Figure 105 - Experiment 3: 1D (Omnidirectional) wavenumber spectrum. Mean Wavenumber Spectrum over 9000 3D sea surface maps. A tukeywin 2D window was used to suppress side-lobe leakage.

We can also compute the full three dimensional (3D) spectrum S(k_x,k_y,f) by Fourier transforming the entire three dimensional wave surface data both in space and time. A slice at k_x = 0 of the full 3D spectrum is shown in Figure 106.

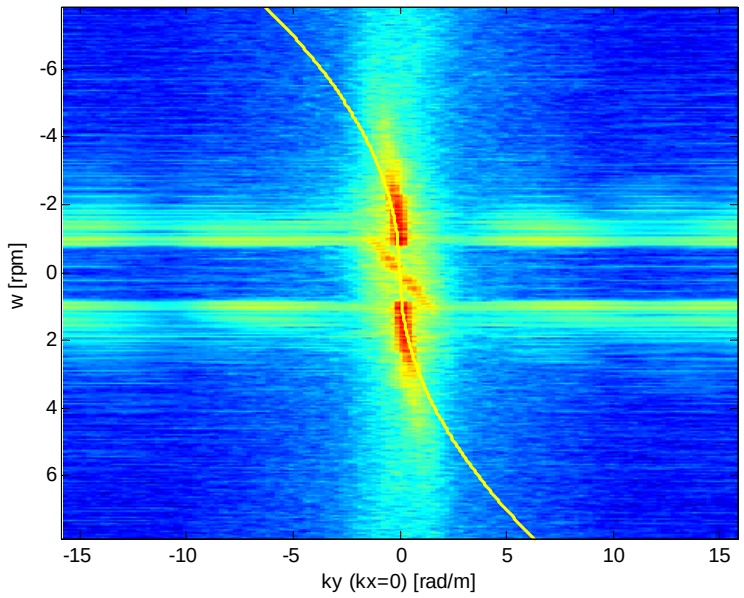

Figure 106 – Experiment 3: Slice at k_x = 0 of the full 3D spectrum S(k_x, k_y,f) in logarithmic scale and linear dispersion relation curve (yellow line).

3.4.3. Wave statistics

By collecting the waves observed at all the virtual probes of Figure 101, we can estimate the wave height distribution which is shown in Figure 107. A fair agreement with the Boccotti model (Boccotti 2000, Tayfun and Fedele 2007) given in Eq. 31 is observed. The mean values over the ensemble of Boccotti parameters are $c \approx 1$, $\psi^* \approx 0.694$. The deviations from Boccotti's model are due to the stochastic dependence of the time series extracted at the virtual probes which are too close compared to the mean wavelength.

The observed crest exceedance is given in Figure . Good is the agreement with the Tayfun-Fedele models (see Eqs. 32-33) and the Forristall model of Eq. 37 (Forristall 2000). The spectral bandwidth is $\nu = 0.38$ and $\mu = 0.067$, $\mu_m = 0.093$, $\mu_a = 0.071$.

The expected maximum wave height $Z(N) =< H_{\max} / \sigma >$ of N observed waves is compared against the Rayleigh and Boccotti models (see Eq. 41) in Figure 109.

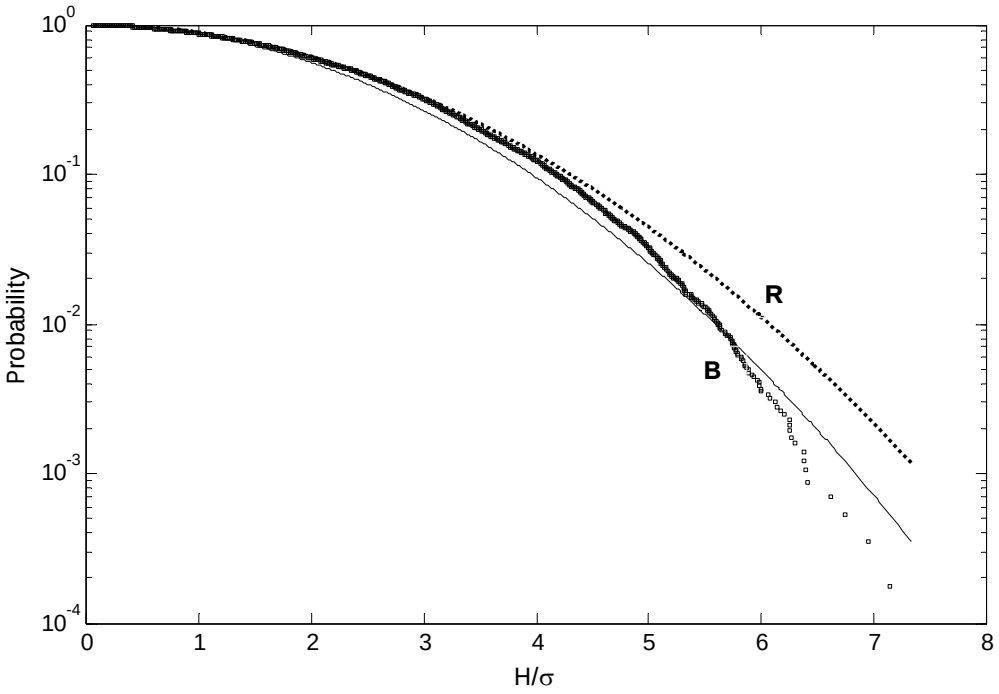

Figure 107 - Experiment 3: Wave height exceedance probability; R=Rayleigh, B=Boccotti.

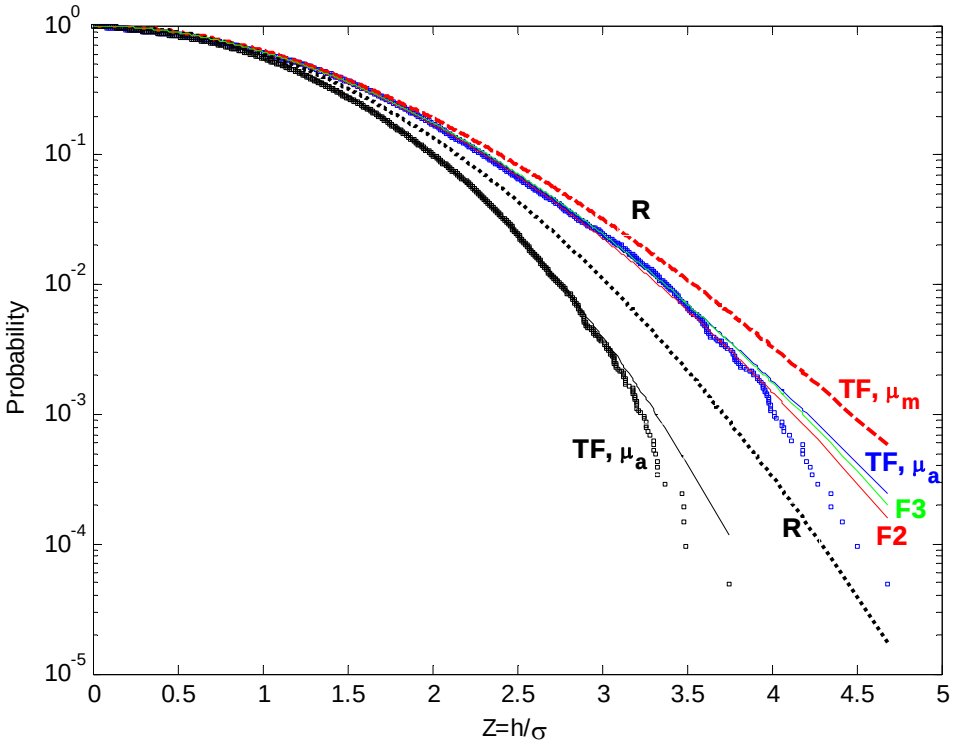

Figure 108 - Experiment 3: Wave crest exceedance probability; R=Rayleigh, TF=Tayfun-Fedele, F2=2d Forristall, F3=3d Forristall.

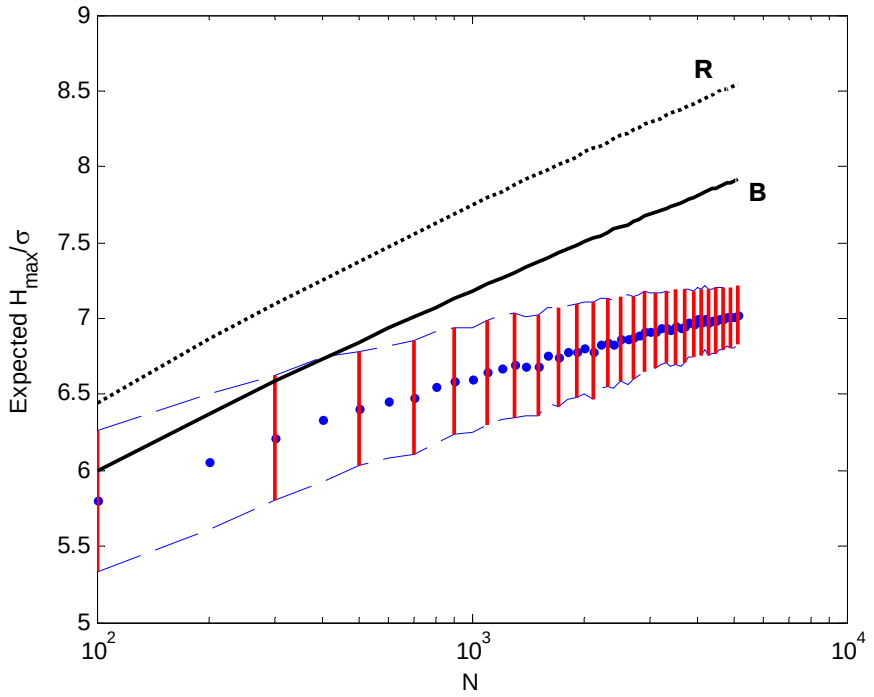

Figure 109 - Experiment 3: Expected maximum wave height: observed average max wave height amplitudes (square dots) and relative stability bands $Z(N)\pm\sigma_N$, σ_N being the associated standard deviation, and theoretical R=Rayleigh, B=Boccotti models, respectively.

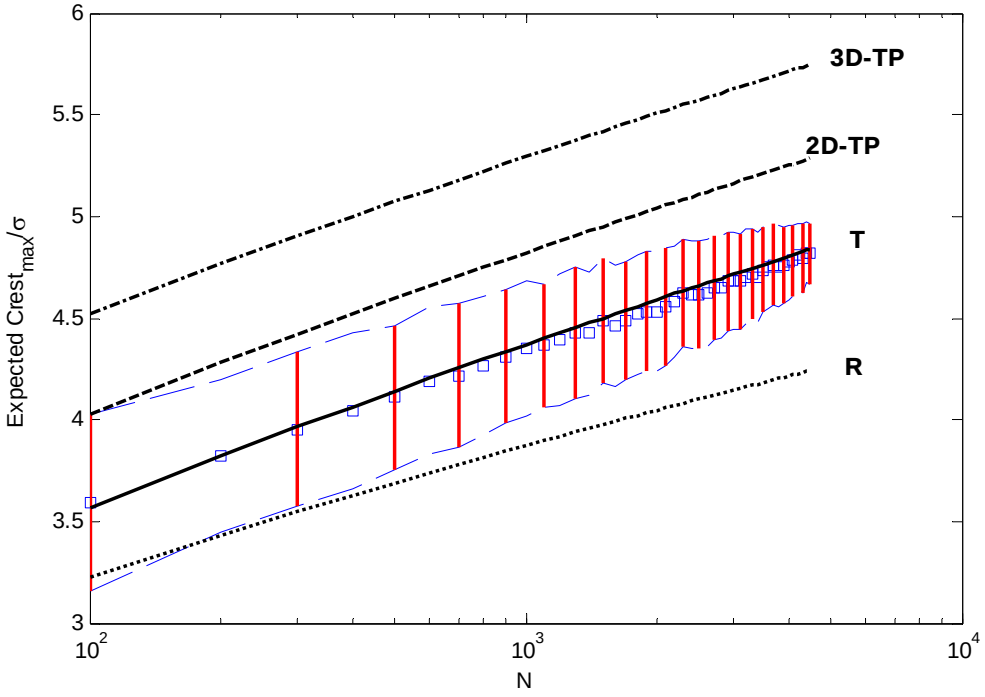

Figure 110 - Experiment 3: Expected maximum crest height: observed average max crest amplitudes (square dots) and relative stability bands $C(N)\pm\sigma_N$, σ_N being the associated standard deviation, and theoretical R=Rayleigh, T=Tayfun, 2D (3D)-TP=two (three) dimensional Tayfun-Piterbarg models, respectively.

Consider the expected maximum crest height $C_T(N) =< C_{\max} / \sigma >$ of N waves observed at the virtual probes of Figure 101. The 1D Tayfun model of Eq. 43 as well as the expected maximum crest height $C_\beta(N)$ of Eq. 46 for $\beta = 1$ (2D Tayfun-Piterbarg model) and $\beta = 2$ (3D Tayfun-Piterbarg model) are compared against the observed crest heights as shown in Figure 110. The crest-to-trough height H of the largest waves observed at the various different virtual probes do not violate the *Miche-Stokes upper bound* of Eq. 49 as shown Figure 111.

The profile of observed waves with the large crest-to-trough amplitudes $\alpha = H/\sigma >> 1$ agree well with the Boccotti theoretical expected profile of Eq. 51 as shown in Figure 112-113.

Further, Figure 114-116 show that the observed conditional ratios $\{C/T \,|\, H = \alpha\}$ *and* $\{T/C \,|\, H = \alpha\}$ agree fairly well with the theoretical expected values given in Eqs. 53-54 ($\mu = \mu_m = 0.0933$, $\psi(T^*) = -0.694$). Finally, Figure 117 shows a comparison between the observed shape of waves with large crest amplitude $\xi = h/\sigma >> 1$ and the respective theoretical expected wave profile given by Eq. 56. The agreement with theory is good.

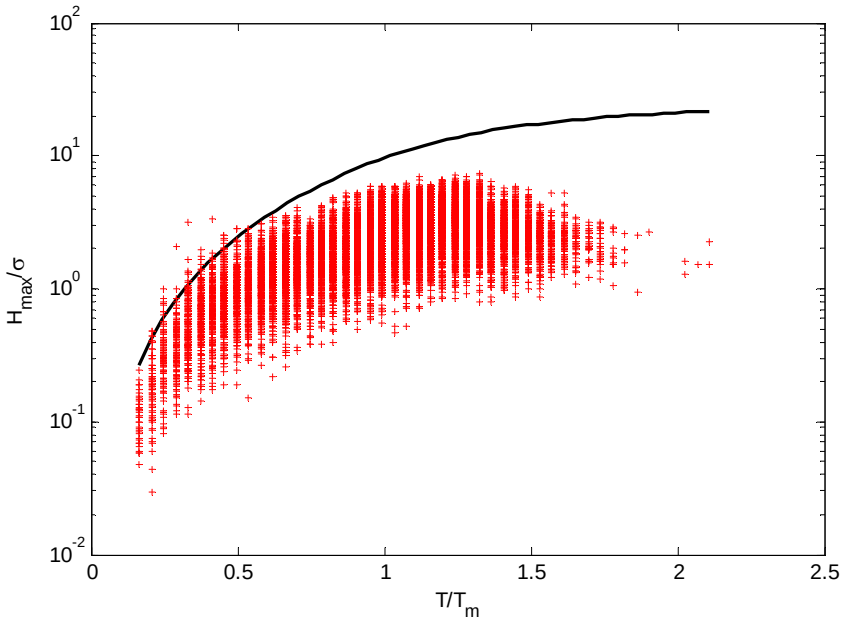

Figure 111 - Experiment 3: Theoretical Miche-Stokes upper bound for the crest-to-trough height H (black line) and observed pairs $(T/T_{m,}\, H/\sigma)$ (red dots), with σ and T_m as the wave surface standard deviation and mean wave period, respectively.

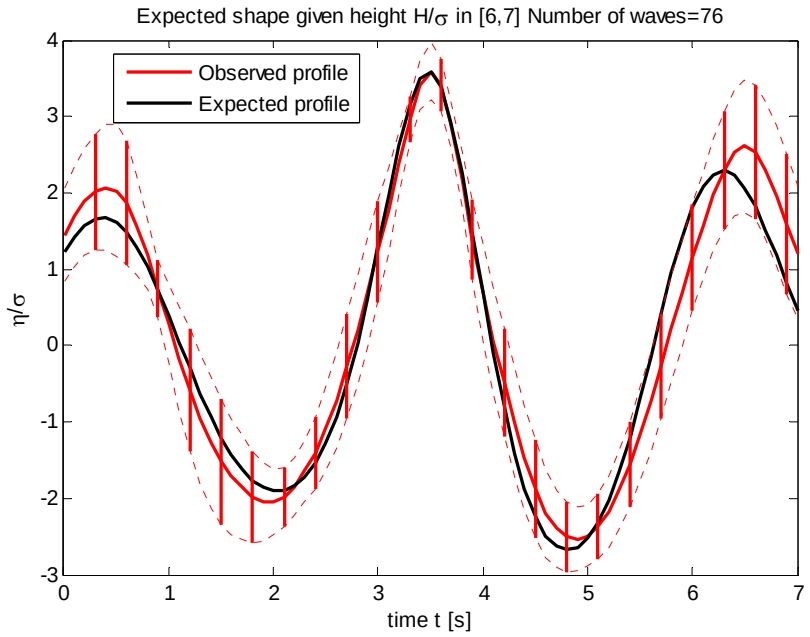

Figure 112 - Experiment 3: Observed shape of large waves (red line) given the crest-to-trough height H in [6σ, 7σ] and respective stability bands, and theoretical expected wave profile (black line).

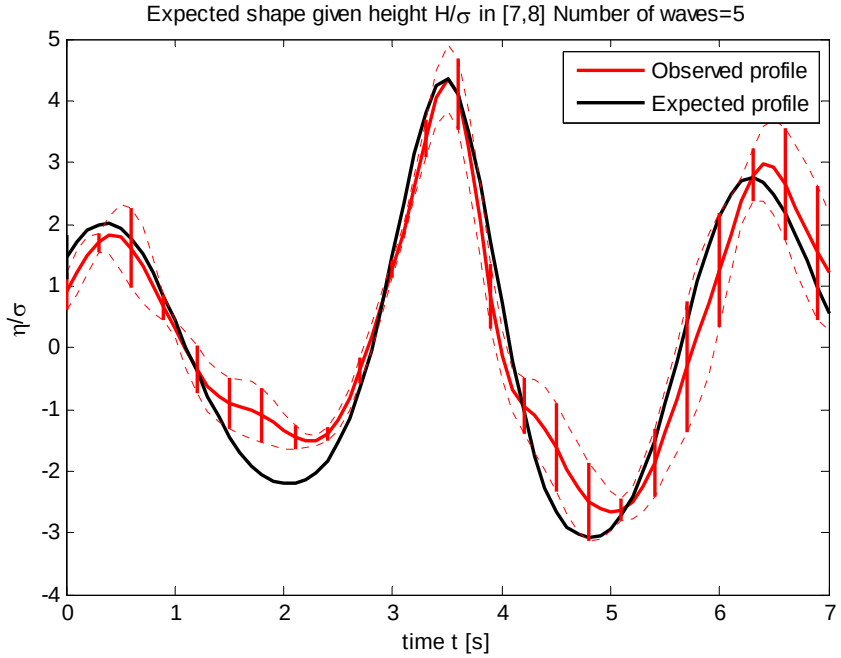

Figure 113 - Experiment 3: Observed shape of large waves (red line) given the crest-to-trough height H in [7σ, 8σ] and respective stability bands, and theoretical expected wave profile (black line).

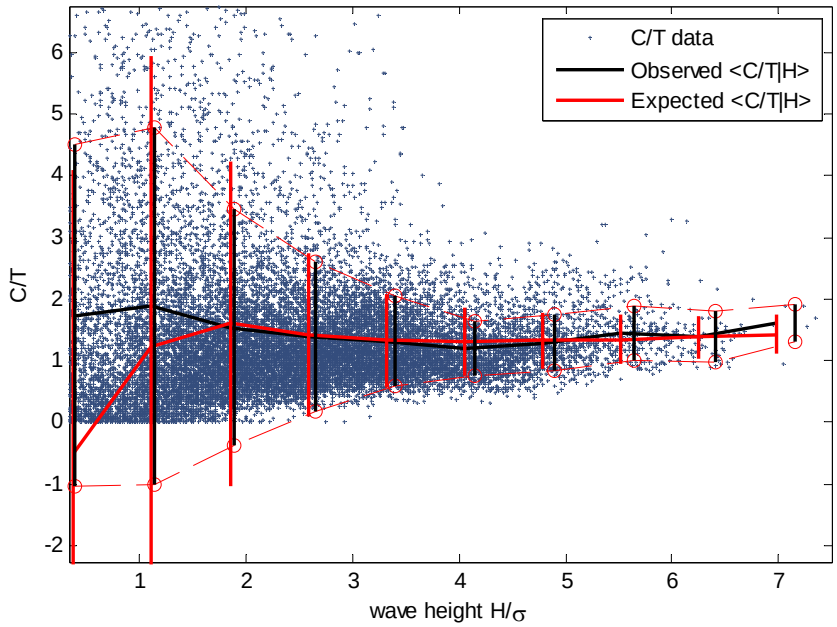

Figure 114 - Experiment 3: Observed crest-to-trough ratio (red line) given the crest-to-trough height H and respective stability bands, and the theoretical expected conditional ratio (black line) .

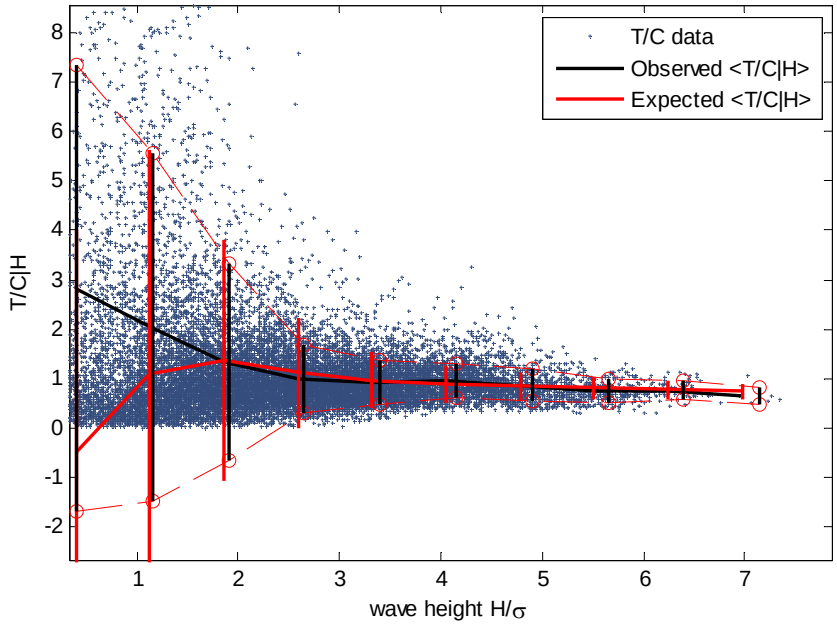

Figure 115 - Experiment 3: Observed trough-to-ratio (red line) given the crest-to-trough height H and respective stability bands, and the theoretical expected conditional ratio (black line) .

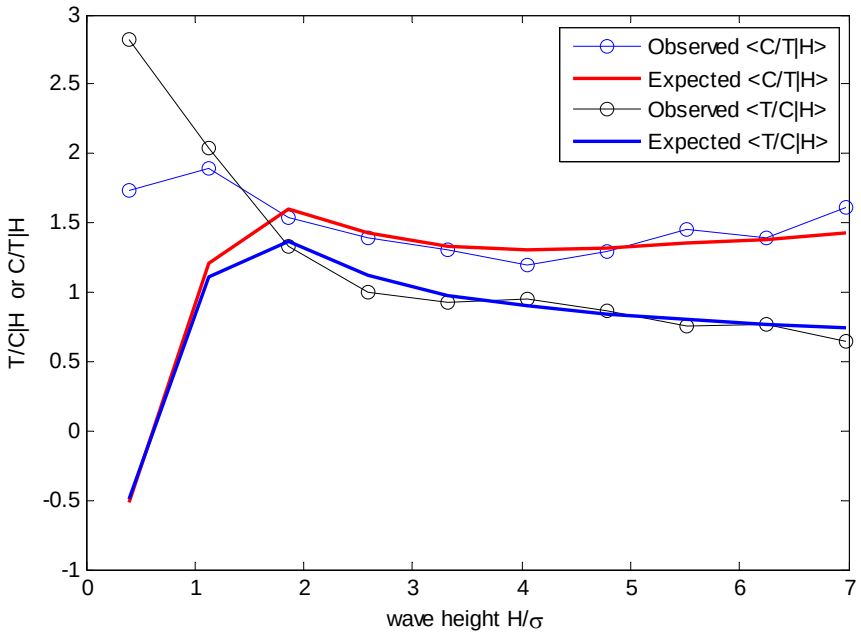

Figure 116 - Experiment 3: Observed conditional averages of C/T (blue dotted line) and of T/C (black dotted line) given the crest-to-trough height H and the associated theoretical expected values (red and blue tick lines, respectively)

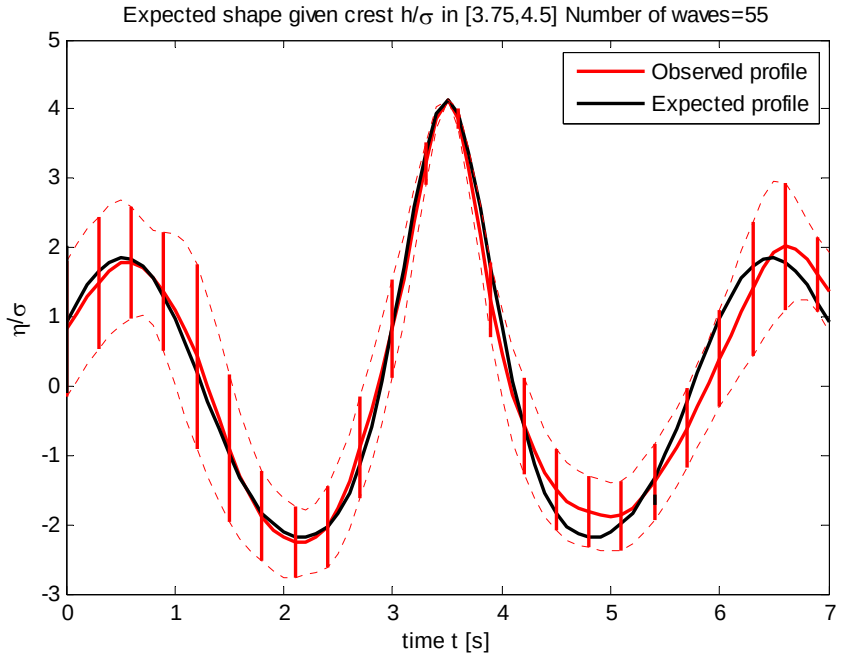

Figure 117 - Experiment 3: Observed shape of large waves (red line) given the crest amplitude h in [3.75σ, 4.50σ] and respective stability bands, and theoretical expected wave profile (black line).

3.4.4. Spatial Analysis

3.4.4.1.Euler Characteristics

Consider a 2D snapshot $\eta(x,y)$ of the wave surface at a given time *t* over a given region *S* as shown in Figure 118. The black region shown in the same figure is the excursion set

$$U_{\eta,h} = \{(x,y) \in S : \eta(x,y) > h\} \tag{61}$$

that is, the portion of the region *S* over which η is above the dimensionless threshold $h = 1.7\sigma$, σ being the standard deviation. The Euler characteristic *EC* is defined as the difference between the number connected components (CC) and holes (H) of the given set, viz.

$$EC = \#Connected\ \ Components - \#Holes \tag{62}$$

For the geometry of Figure 118, the *EC* is equal to four since we only have four connected components and no holes. Note that the *EC* of an excursion set depends very strongly on *h*. If this is low, then *EC* counts the number of holes in the given set. If the threshold is high (see Figure 118), then all the holes tend to disappear and the *EC* counts the number of connected components, or local maxima of the wave surface at a given time.

For weakly non-linear wave surfaces defined over a region *S* of area $A_S = L_x L_y$, the expected value of the *EC* is given by (Adler 1981, Worsley 1995, Adler and Taylor 2007)

$$< EC(\xi) >= EC_{area}(\xi_1) + EC_{boundary}(\xi_1) + \Pr\{Z > \xi_1\} \tag{63}$$

where

$$EC_{area}(\xi) = N_S\, \xi_1 \exp\left(-\xi_1^2/2\right), \qquad EC_{boundary}(\xi) = N_P \exp\left(-\xi_1^2/2\right), \tag{64}$$

Here, $<\bullet>$ denotes expectation, $\xi = h/\sigma$ is the normalized threshold amplitude which satisfies

$$\xi = \xi_1 + \frac{\mu}{2}\,\xi_1^2, \tag{65}$$

and *Z* is Gaussian with zero mean and unit variance. Further,

$$N_S = \sqrt{2\pi}\,\frac{L_x L_y}{\bar{L}_x \bar{L}_y}\sqrt{1-\alpha_{xy}^2}, \qquad N_P = \frac{L_x}{\bar{L}_x} + \frac{L_y}{\bar{L}_y} \tag{66}$$

are the average number of 'waves' over the area S and along the perimeter P, respectively, and $\overline{L}_x$ and $\overline{L}_y$ are the mean wavelength along two orthogonal directions x and y, respectively. These can be expressed solely in terms of the moments of the directional spectrum $S(k_x, k_y)$ as (Baxevani and Richlik 2004)

$$\overline{L_x} = 2\pi\sqrt{\frac{m_{00}}{m_{20}}}, \quad \overline{L_y} = 2\pi\sqrt{\frac{m_{00}}{m_{02}}}, \quad \alpha_{xy} = \frac{m_{11}}{\sqrt{m_{20}m_{02}}}, \tag{67}$$

where

$$m_{ij} = \int\int k_x^i k_y^j S(k_x, k_y)\, dk_x dk_y. \tag{68}$$

The $EC_{boundary}$ term in (63) will be referred to as a boundary correction because it is important when the excursion set touches the boundary/perimeter of the area S (Worsley 1995).

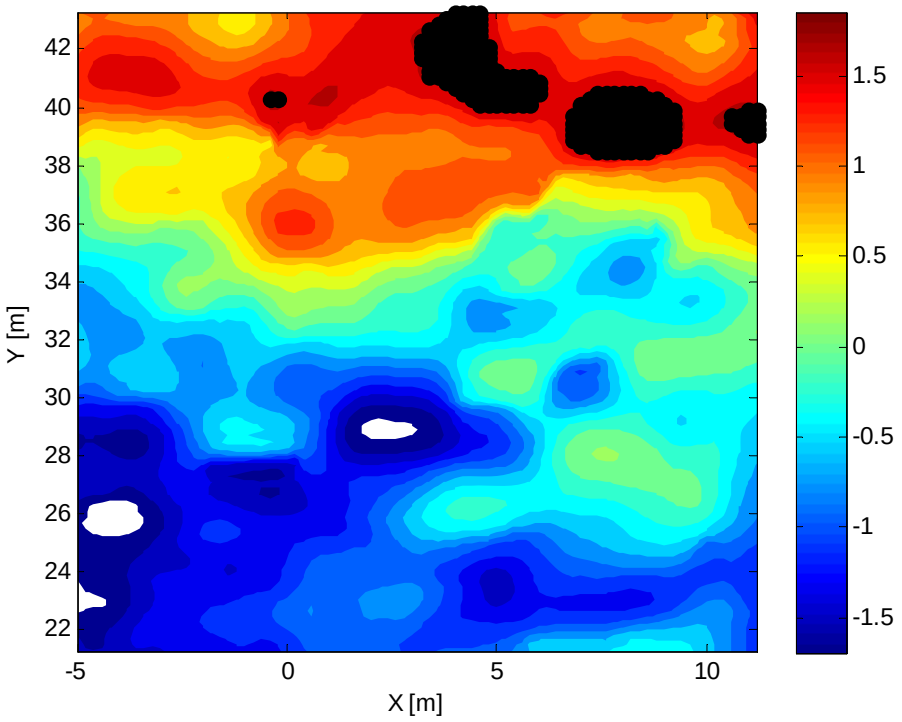

Figure 118 - Experiment 3: Excursion set (black region) of the normalized wave surface η/σ, that is the portion of domain over which η is above the threshold 1.7σ. Note that, as the threshold increases the excursion set is the union of isolated regions delimiting the local maxima of the wave surface.

Adler (1981) and Adler and Taylor (2007) have shown that the probability that the global maximum of a random field η exceeds a threshold h is well approximated by the expected EC of the excursion set $U_{\eta,h}$, provided the threshold is high. Indeed, as the threshold h increases, the holes in the excursion set $U_{\eta,h}$ disappear until each of its connected components includes just one local maximum, and the EC counts the number of local maxima. For very large thresholds, the EC equals 1 if the global maximum exceeds the threshold and 0 if it is below. Thus, the $EC(U_{\eta,h})$ of large excursion sets is a binary random variable with states 0 and 1, and for $h>>1$

$$\Pr(\eta_{\max} > \xi) = \Pr\left[EC(U_{\eta,h}) = 1\right] = < EC(\xi) > \tag{69}$$

Piterbarg (1995) also derived the same asymptotic formula by studying large Gaussian maxima over an infinite area, as $A_S \to \infty$.

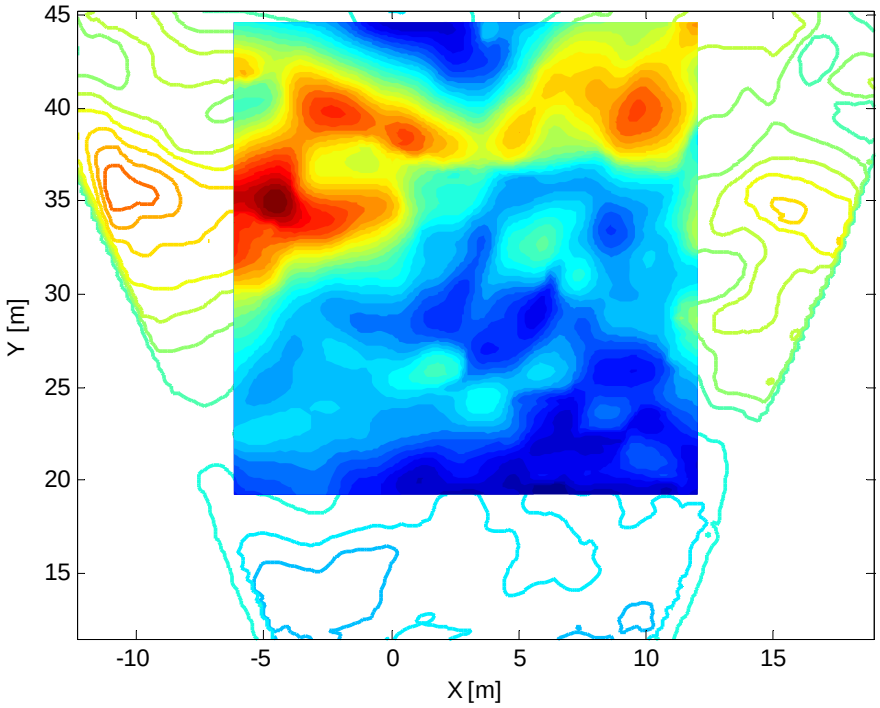

Figure 119 - Experiment 3: Large area S for EC computations.

3.4.4.2.Applications

Consider the area *S* shown in Figure 119. We will compute the EC for each snapshot (9000 in total) of the observed wave surface and then compute the expected EC value and the associated standard deviation. To do so, an estimate of the instantaneous mean wavelengths $\overline{L}_x$ and $\overline{L}_y$ in time is computed and plotted in figure 120. From these, the average number of waves N_S and N_P over the area S and along its perimeter P, respectively, follow as shown in Figure 121. Note that N_P is comparable to N_S since the area is relatively small compared to the squared mean wavelength. Thus, the global maximum $\eta_{\max} = \max(\eta)/\sigma$ of the wave surface may also occur on the boundary and its expected value over the area *S* stems from a Gumbel statistics as

$$<\eta_{\max}>= h_N + \frac{\mu}{2} h_N^2 + \gamma \frac{1+\mu h_N}{h_N - \dfrac{N_S}{N_S h_N + N_P}} \tag{70}$$

where $\gamma \approx 0.5772$ and h_N satisfies

$$\left(N_S\, h_N + N_P\right)\exp\left(-h_N^2/2\right) = 1 \tag{71}$$

If $N_P = 0$, the Tayfun-Piterbarg model proposed by Krogstad et al. (2004) is recovered. Figure 122 reports the time variation of the estimated expected maximum $<\eta_{\max}>$ computed both with and without boundary corrections ($N_P = 0$). For comparison, we also plotted the observed maximum height over the area S and the maximum height expected along the boundary of S. Figure 123 shows the observed average EC and the respective stability bands. Good agreement with their theoretical expectations is found when the boundary corrections $EC_{boundary}$ are accounted for. Further, from figure 124 it is clear that the exceedance probability of the maximum wave surface represented by the EC curve deviates from both the Rayleigh and Tayfun-Fedele models. These deviations tend to reduce as the area become smaller as shown in figures 126-127 which report the observed EC for the smaller area shown in Figure 125. The expected number of waves for this case are shown in Figure 128 and the estimated expected maximum $<\eta_{\max}>$ is compared against the observed areal maximum in Figure 129. We observe that $<\eta_{\max}>$ reduces as the area *S* reduces in size (see also Figure 130).

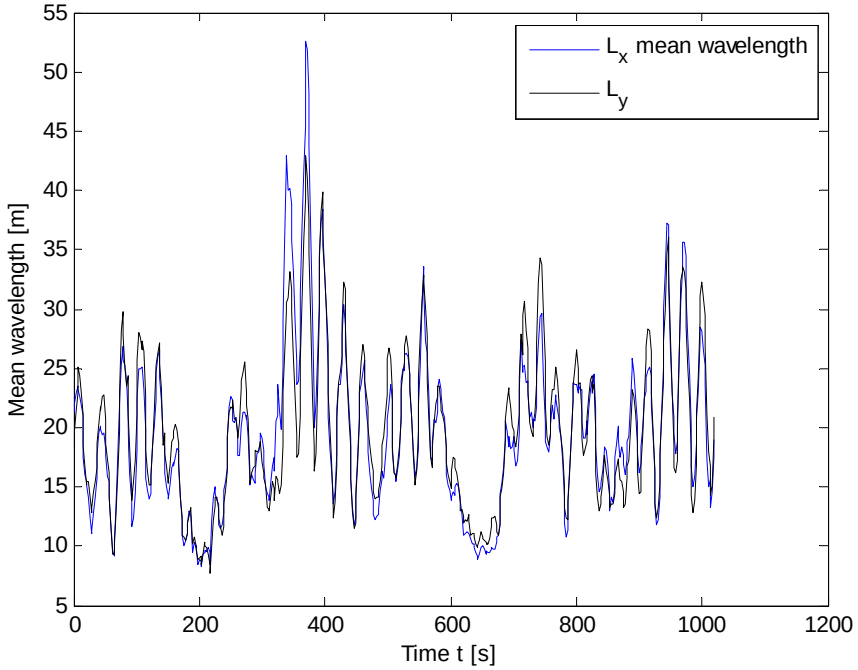

Figure 120 - Experiment 3: Observed mean wavelengths $\overline{L}_x$ (blue line) and $\overline{L}_y$ (black line) for the large area S of Figure 119.

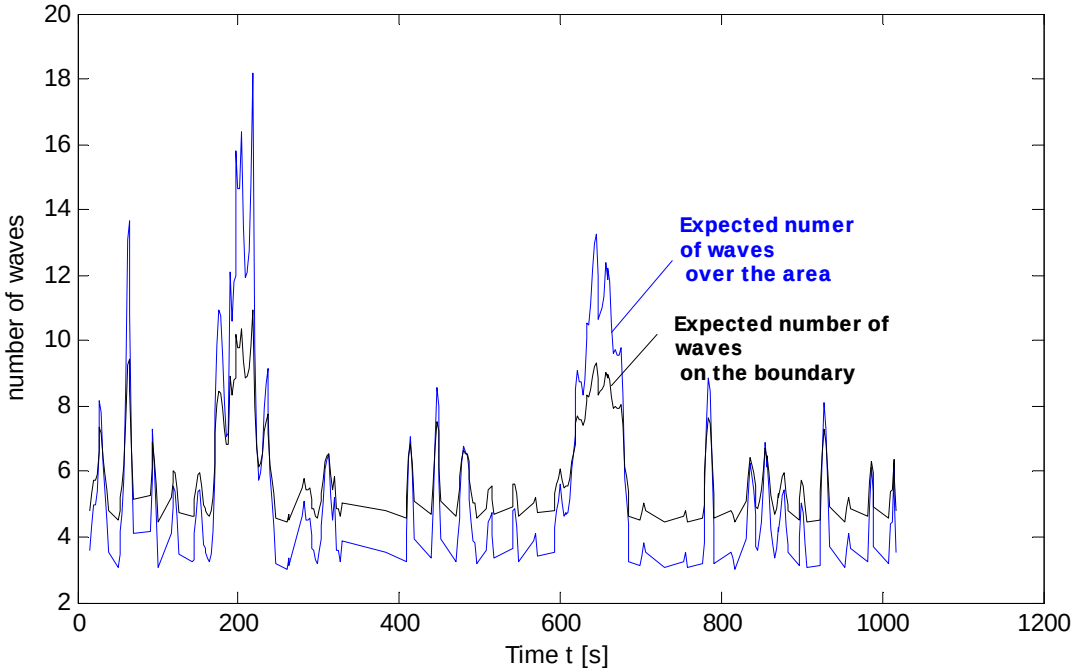

Figure 121-Experiment 3: Expected number of waves over the area S (see Figure 117) and along the perimeter P.

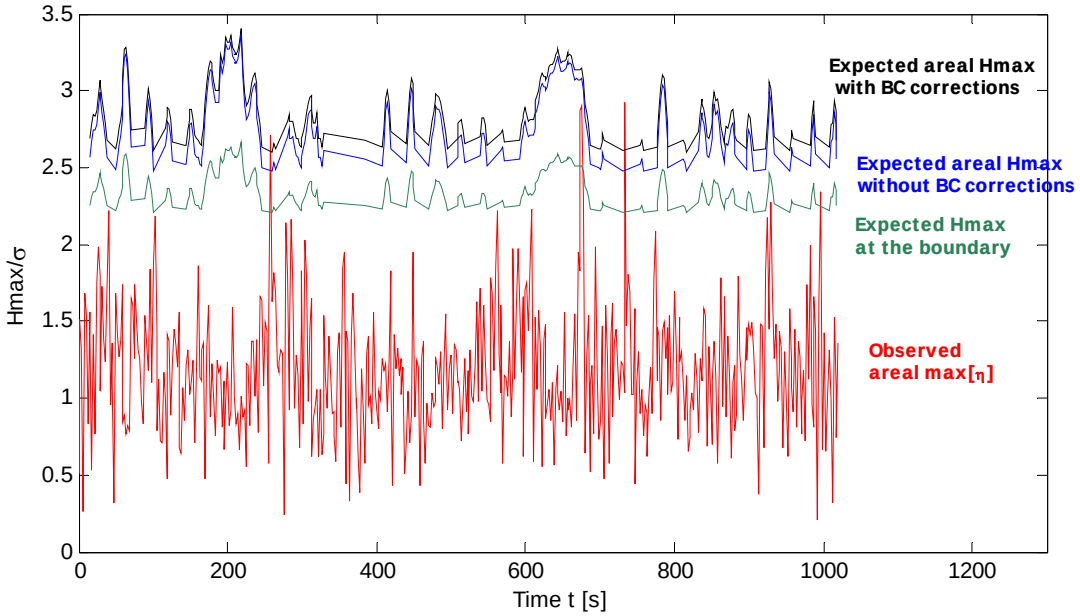

Figure 122 - Experiment 3: Time variation of the expected maximum wave surface over the large area S of Figure 119 computed with and without boundary corrections, the expected maximum along the boundary of S and the observed maximum over the area from data.

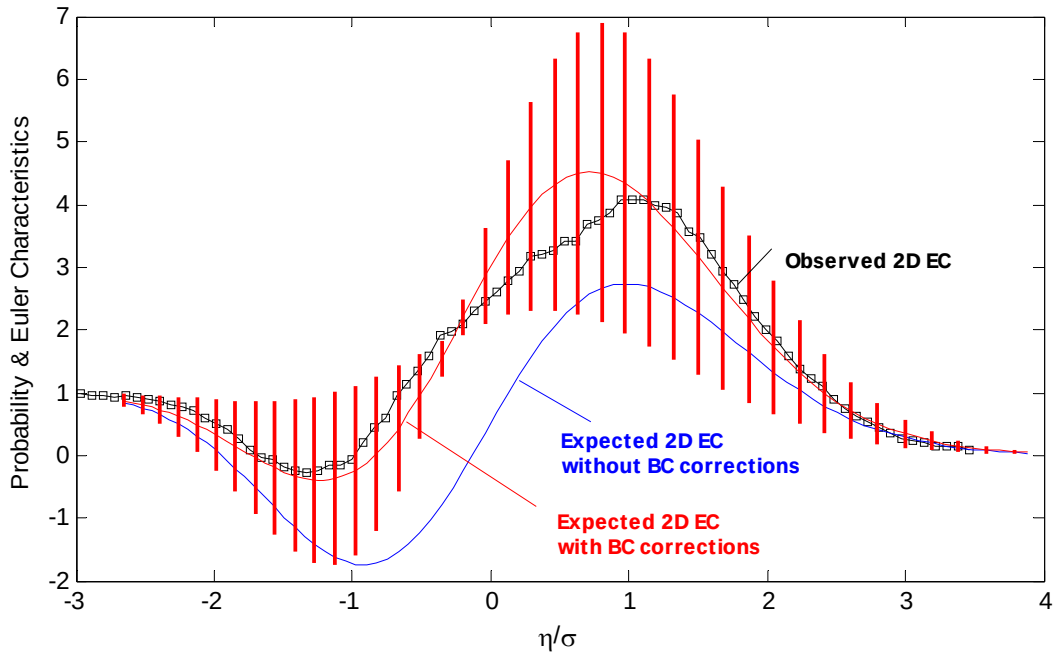

Figure 123 - Experiment 3: Observed Euler Characteristics and theoretical expected values over the large area S of Figure 119.

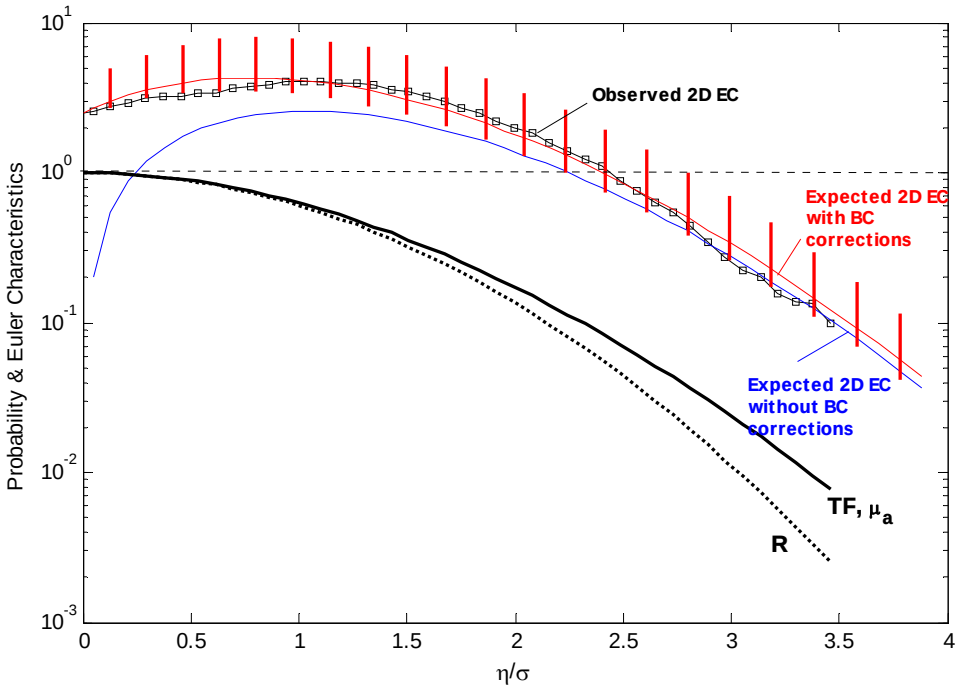

Figure 124 - Experiment 3: Observed Euler Characteristics and theoretical expected values compared to the R=Rayleigh and TF=Tayfun-Fedele models, respectively (large area S of Figure 119).

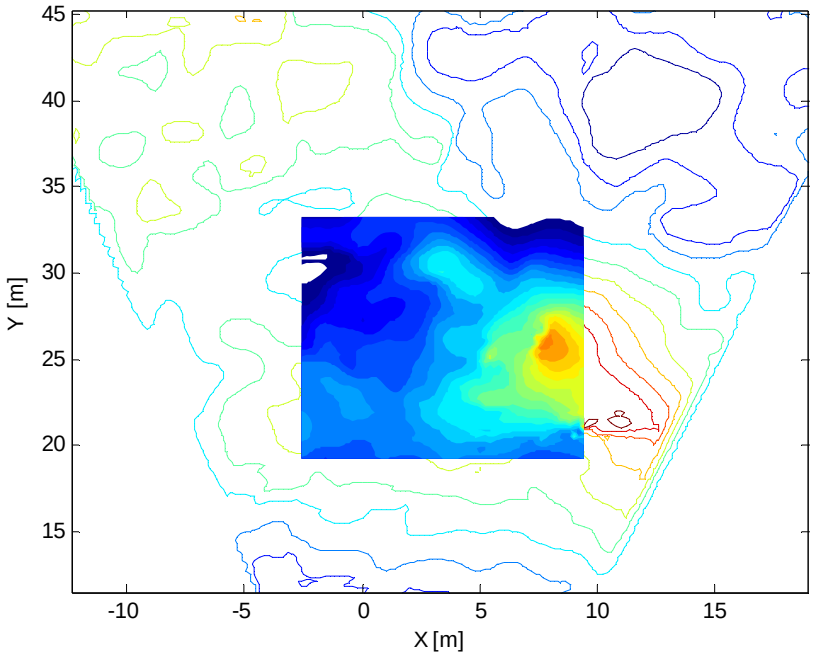

Figure 125 - Experiment 3: Small area S for EC computations.

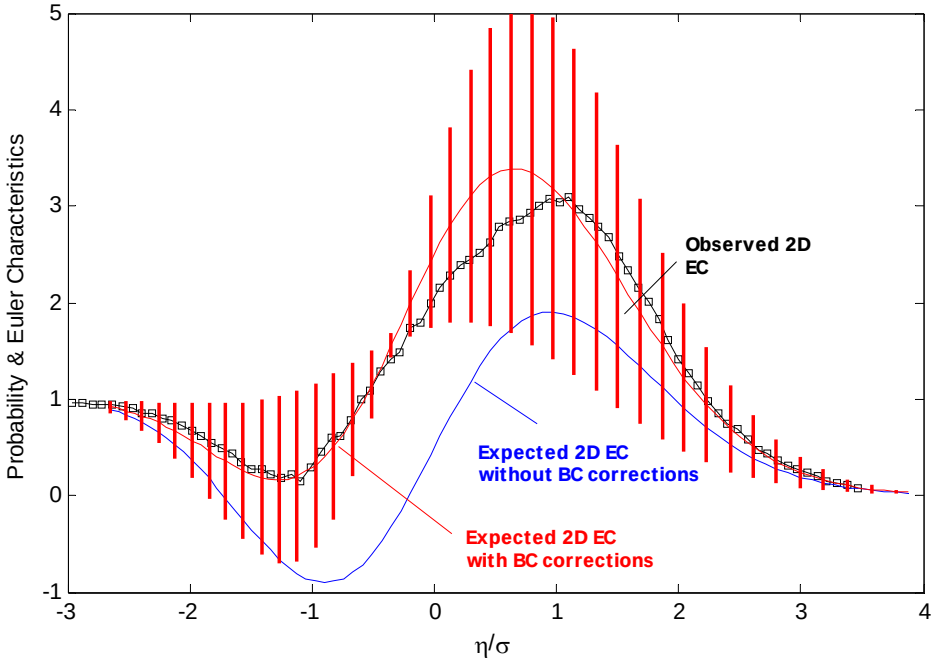

Figure 126 - Experiment 3: Observed Euler Characteristics and theoretical expected values over the small area S shown in figure 125.

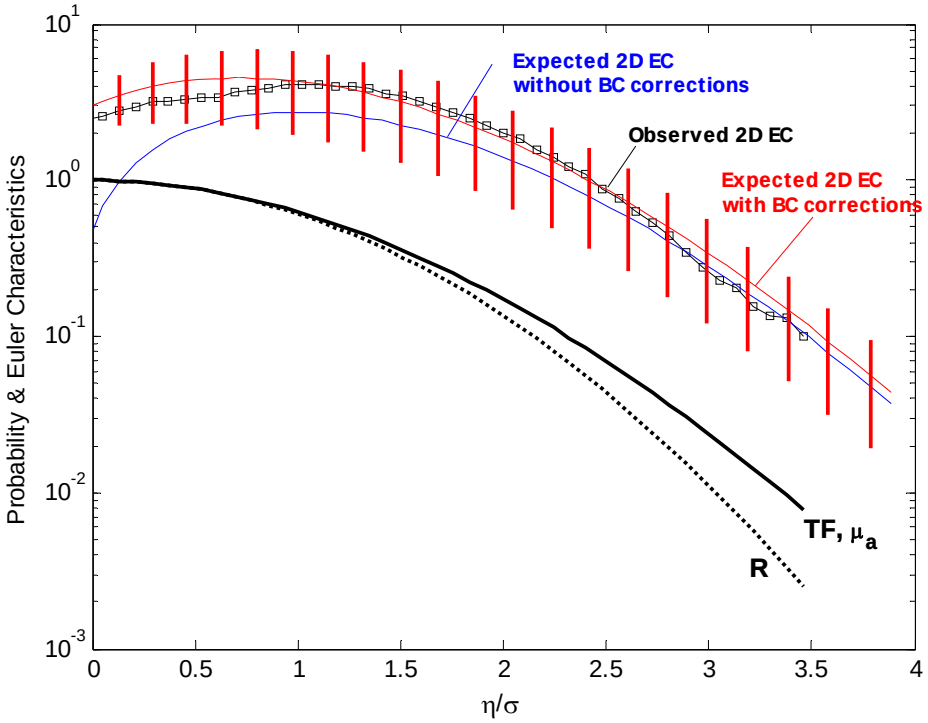

Figure 127 - Experiment 3: Observed Euler Characteristics and theoretical expected values over the small area S (see figure 125) compared to the R=Rayleigh and TF=Tayfun-Fedele models, respectively.

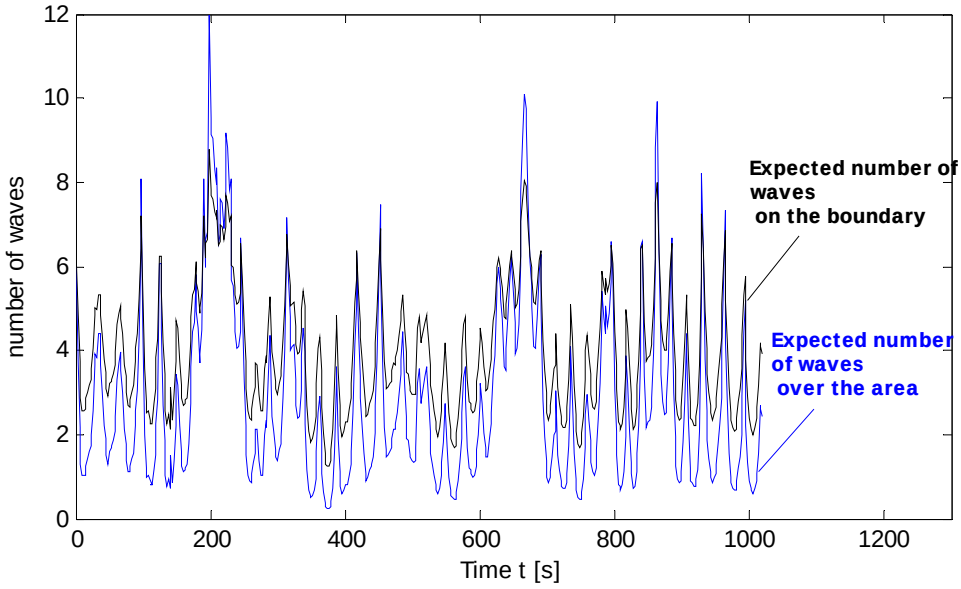

Figure 128 - Experiment 3: Expected number of waves over the small area S of Figure 123 and along its perimeter P.

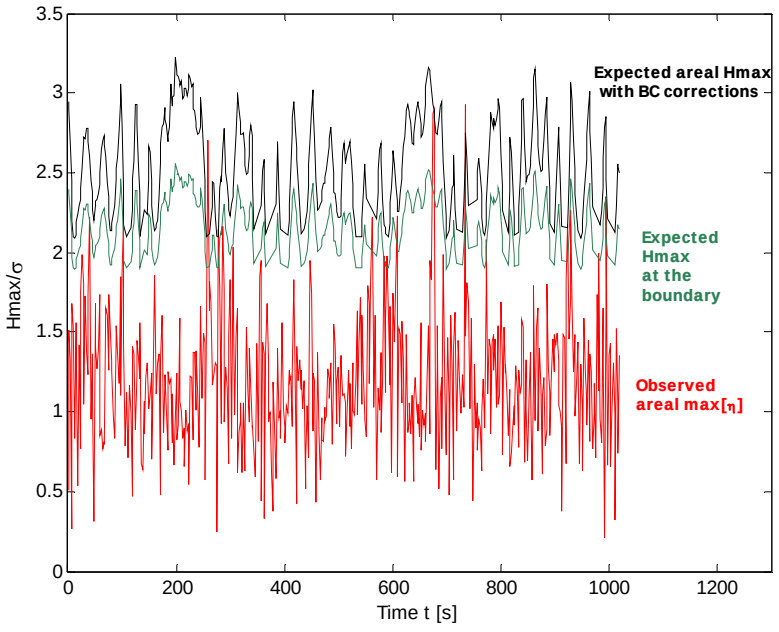

Figure 129 - Experiment 3: Time variation of the expected maximum wave surface over the small area S of Figure 125 computed with and without boundary corrections, the expected maximum along the boundary of S and the observed maximum over the area from data.

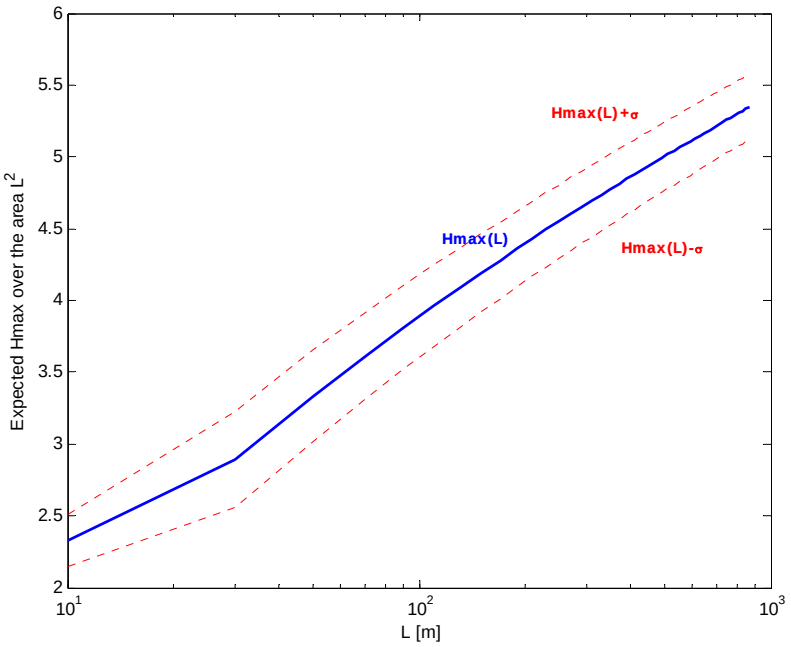

Figure 130 - Experiment 3: Expected maximum wave height over a square area as function of the side length L and associated stability bands $H_{max}(L)\pm\sigma$, σ being the standard deviation of the sampled wave heights.

4. CURRENT ESTIMATES

Consider the reconstructed wave surface during the March 2010 event (Experiment 3). From the wave space-time volume $\eta(x,y,t)$ we extract the surface height $\eta(s,t)$ along the North direction s (see Figure 131) passing by the centre of the reconstructed domain. During the March event the current was mostly directed along s, and according to the AWAC Acoustic Doppler Current Profile (ADCP) measurements it varied with depth as shown in Table 21 (see also Figure 135). In order to estimate currents, we first compute the 2D spectrum $S(k,f)$ of $\eta(s,t)$. On the domain (k,f) the log-amplitude map of S is given in Figures 132-133. The regions of non zero amplitudes identify the wave dispersion curve (black line). This does not match the theoretical dispersion curve (dot line)

$$k = \pm\frac{(2\pi f)^2}{g}, \qquad (72)$$

possibly because (72) does not account for current effects underneath the wave surface. The Doppler-shift, which causes the mismatch between the observed dispersion and (72), allows estimating the current speed as follows. In presence of a current U_0 collinear with the direction of wave propagation, (72) becomes (Boccotti, 2000)

$$k = \pm\frac{(2\pi f - U_0 k)^2}{g}. \qquad (73)$$

In reality U_0 in (73) is an average speed that accounts for the effects of long-wave modulation on short waves and the variability of current with depth (Stewart and Joy, 1974).

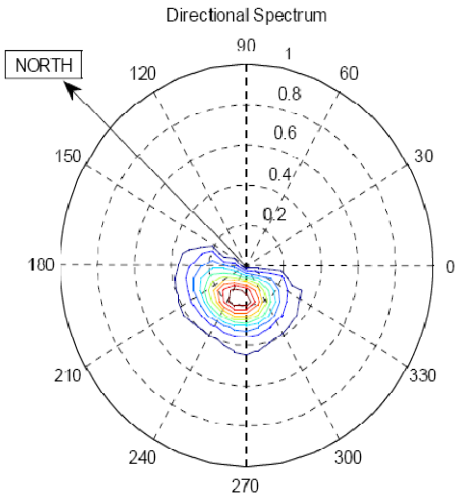

Figure 131 - North direction and WASS axes.

Further, U_0 is a function of k since longer waves feel the current at the sea bottom whereas shorter waves that nearby the surface. Indeed (Steward and Joy, 1974),

$$U_0(k) = 2k \int_{-\infty}^{0} U(z) \exp(2kz)\, dz\,, \qquad (74)$$

where $U(z)$ is the unknown current profile. The estimation of U from (73) and (74) is an ill-posed inverse problem which needs regularization. To do so, we add the constraint that $U(z)$ is an exponential profile such as

$$U(z) = U_{\max} \exp(\alpha z)\,, \qquad z \le 0, \qquad (75)$$

and from (74) it follows

$$U_0(k) = \frac{2kU_{\max}}{2k+\alpha}\,. \qquad (76)$$

Here, $k(f)$ is a function of f via the theoretical dispersion relation (73). As an example, Figure 134 plots $U_0(k)$ as function of k for different exponential vertical current profiles (75), viz. α=0,0.2, 0.5 and 1, respectively. As the current decays slower with depth, longer waves are affected by the deep current, whereas shorter waves are altered by the near-surface current. The best values for $U_{\max}$ and α that match the observed dispersion curve with the theoretical form (73) are $U_{\max}$=-0.45 m/s and $\alpha = 0.1$ 1/m, respectively. The fitted wave-current dispersion curve (73) is shown in Figures 132-133. WASS estimate of the current profile follows from (75) and it is shown in Figure 135 in comparison to that measured by the AWAC instrument operational at *Acqua Alta*. Note that the observed dispersion curve in Figure 133 shows a linear branch in the low-frequency range corresponding to a constant speed ~0.125 m/s. We speculate that this is the wave-induced current generated by longer waves larger than the imaged area.

Finally, we have repeated the same procedure as above using data from Experiment 2 (Oct 14 2009) to get current estimates. In particular, Figure 136 reports the 2D log spectrum estimated from the reconstructed surface and in table 22 the associated current estimates are given. The agreement with AWAC data is fair just nearby the free surface.

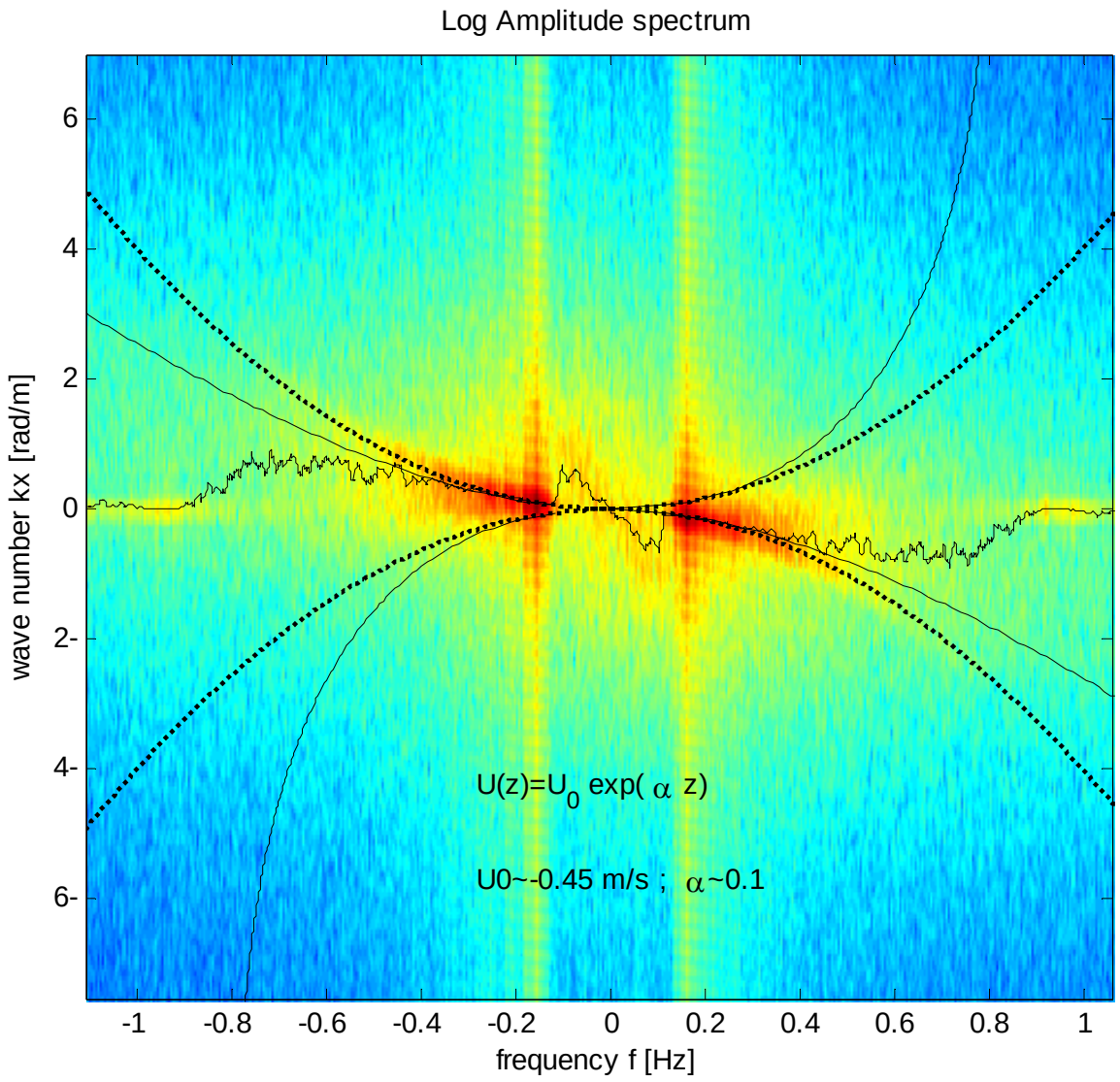

Figure 132 - 2D Log spectrum, observed dispersion curve (black line), theoretical dispersion curve without current (dot line) and with current (solid line).

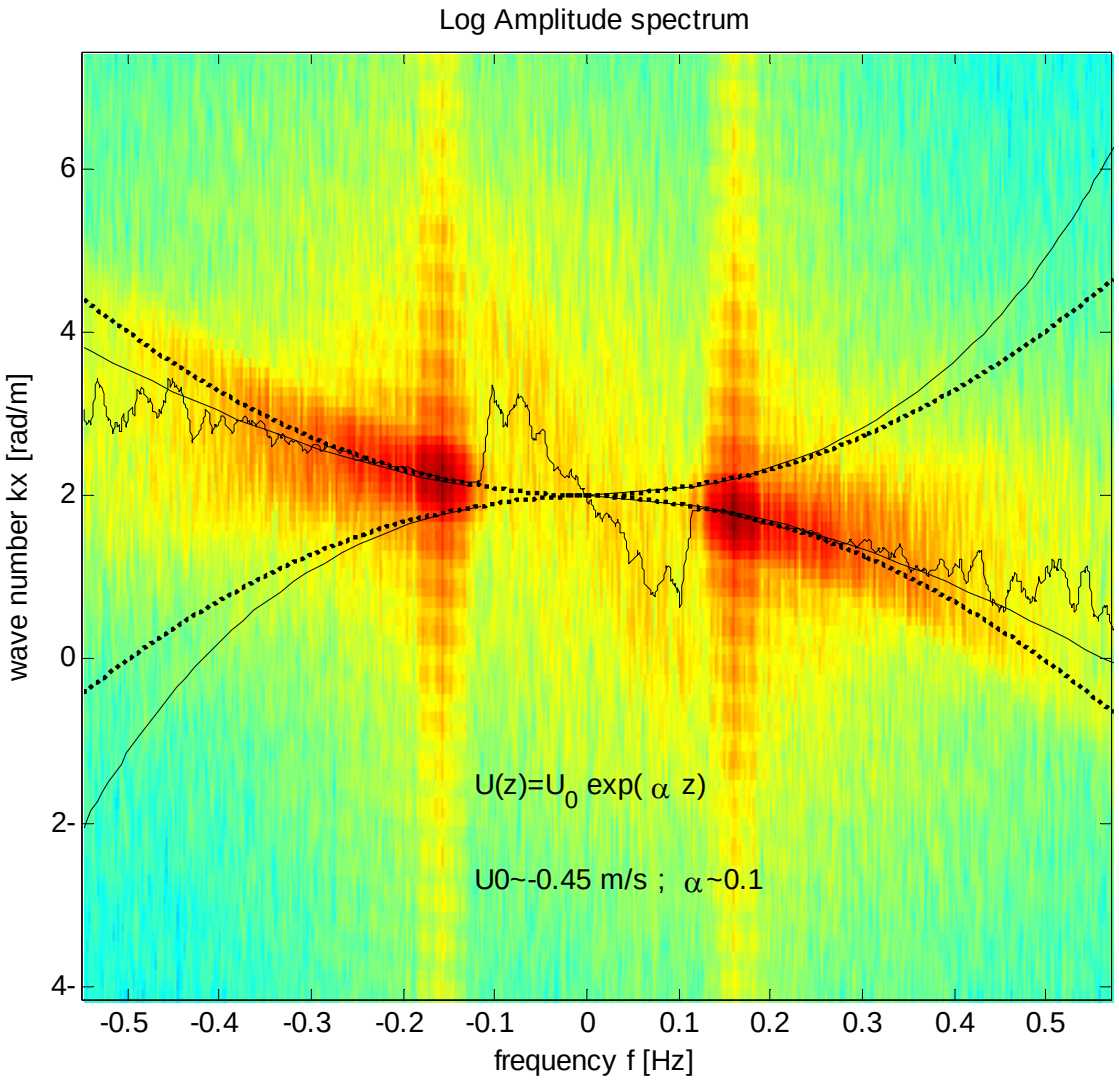

Figure 133 - Particular of the 2D Log spectrum of Figure 132.

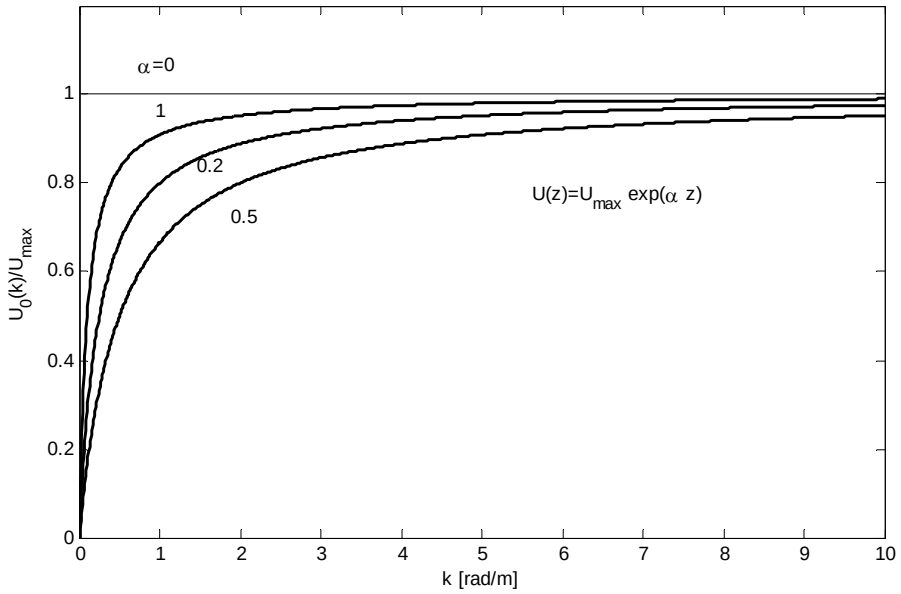

Figure 134 - The average current $U_0(k)$ for different exponential vertical current profiles.

Table 21: AWAC current measurements and WASS estimates

Distance [m] from bottom	Velocity North [m/s]	WASSEstimates [m/s]
1	-0.248	-0.111
2	-0.257	-0.123
3	-0.275	-0.136
4	-0.272	-0.150
5	-0.293	-0.166
6	-0.262	-0.183
7	-0.27	-0.202
8	-0.261	-0.223
9	-0.319	-0.247
10	-0.287	-0.273
11	-0.333	-0.303
12	-0.356	-0.333
13	-0.325	-0.368
14	-0.364	-0.407
15	-0.422	-0.450

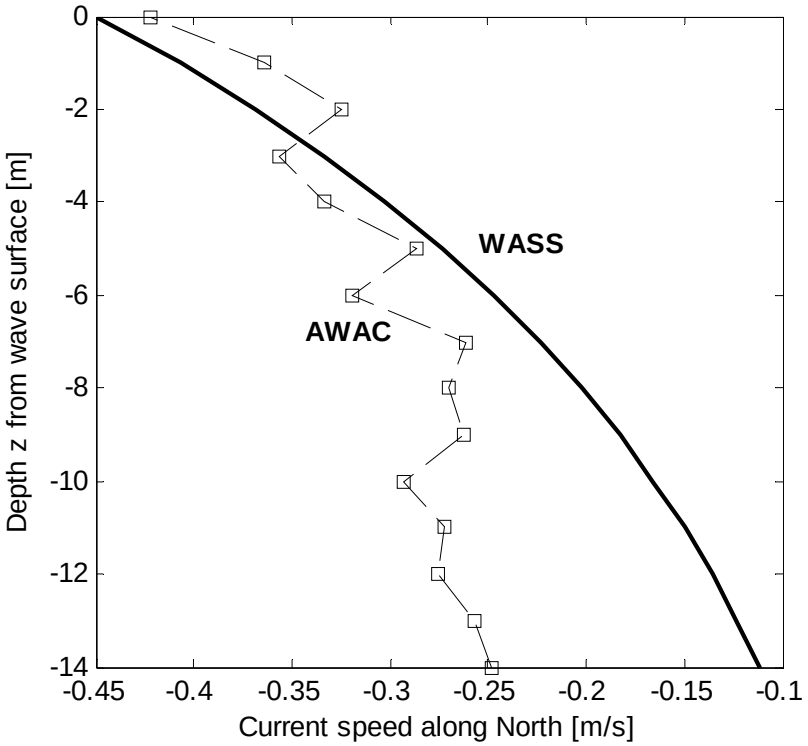

Figure 135 - AWAC current measurements and WASS estimates.

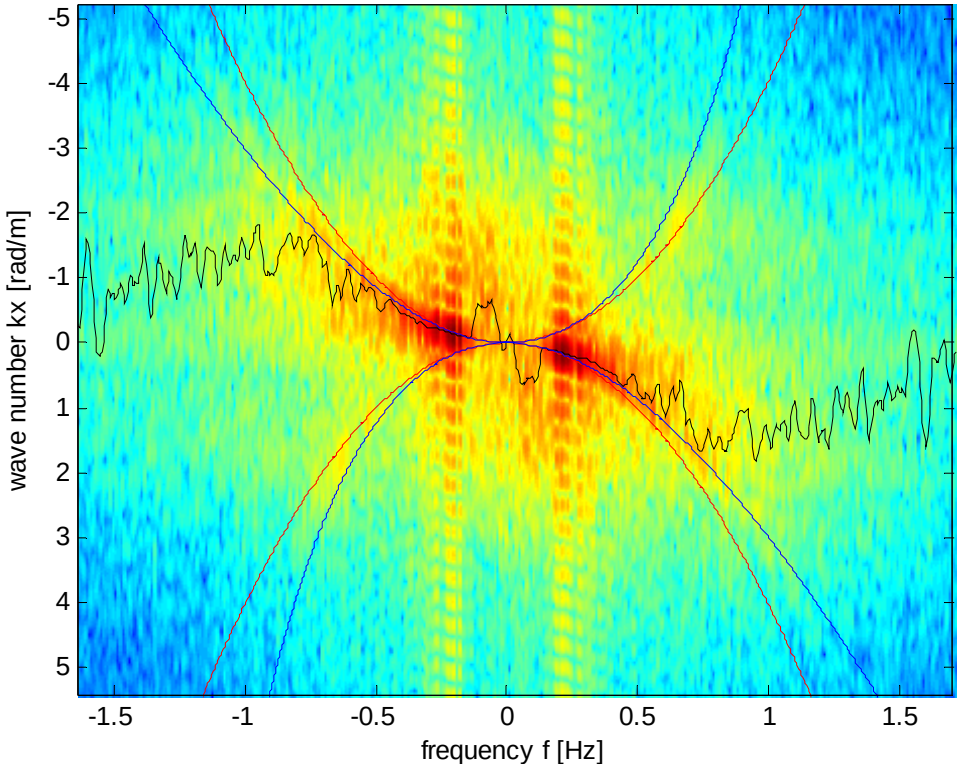

Figure 136 - 2D Log spectrum, observed dispersion curve (black line), theoretical dispersion curve without current (dot line) and with current (solid line).

Table 22: AWAC current measurements and WASS estimates

Distance [m] from bottom	Velocity North [m/s]	WASSEstimates [m/s]
1	-0.068	-0.018
2	-0.163	-0.022
3	-0.082	-0.027
4	-0.142	-0.033
5	-0.045	-0.041
6	-0.001	-0.050
7	-0.098	-0.061
8	-0.144	-0.074
9	-0.166	-0.090
10	-0.115	-0.110
11	-0.113	-0.134
12	-0.131	-0.164
13	-0.117	-0.201
14	-0.123	-0.245
15	-0.263	-0.280

5. SUPPLEMENTAL MATERIAL: MOVIES

We have prepared several movies in avi format of the 3D reconstructions, directional spectra and orbital velocities, the latter computed using the nonlinear algorithm formulated by Grue et al.(2008). The multimedia material can be downloaded at the ftp site (password*: Protecno10*)

ftp://voltaba_pd@ftp.protecno.it/../CNR_chevron/2010_chevron_report_movies/

or you can click on the links below for individual movies:

Experiment 1

- Experiment_1_image_and_3D.avi (95554 KB)
- Experiment_1_image_and_3D_short.avi (12637 KB)

Experiment 2

- Experiment_2_3D_and_directional_spectrum.avi (72357 KB)
- Experiment_2_3D_and_orbital_velocity.avi (10833 KB)
- Experiment_2_image_and_3D.avi (9408 KB)

Experiment 3

- Experiment_3_image_and_3D.avi (13938 KB)
- Experiment_3_image_and_time_series.avi (216257 KB)

6. CONCLUSIONS AND FUTURE DEVELOPMENTS

We have deployed a novel Wave Acquisition Stereo System (**WASS**) at the oceanographic tower '*Acqua Alta*' off the Venice coast, Italy. As a video observational technology, **WASS** was able to provide a multi-dimensional image of the oceanic state around the tower under both Bora and Scirocco wave conditions. To do so, advanced stereo techniques based on the epipolar geometry were exploited to obtain 3D reconstructions of the sea surface map in time. By just exploiting time series of reconstructed wave surface displacements extracted at virtual point probes, we proved that the accuracy of the **WASS** measurements is comparable to that of more traditional wave instruments. Further, the statistics of crest and trough heights, as well as that of crest-to-trough heights estimated via **WASS** agree very well with well known theoretical models, such as the Forristall and Tayfun-Fedele distributions for crests and the Boccotti model for wave heights.

A statistical analysis of the reconstructed spatial snapshots in time based on both Piterbarg's theory and Adler's Euler Characteristics revealed that the expected maximum wave surface height over an area is larger than that expected at a given point in space. Further, the directional spectrum can be estimated directly by averaging over the reconstructed spatial snapshots. If we then consider the entire data set as a space-time data volume then the 3D Fourier Transform provides estimates of wave dispersion and currents, and then orbital velocities on the surface can then be estimated via inversion of the Laplace equation (Grue et al. 2008).

In the future, we plan to improve the stereo reconstruction algorithm by means of Graphics Processing Units (GPU) that can compute the Fast Fourier Transform (FFT) efficiently. Indeed, the FFT is a key element of the stereo image processing. Preliminary results carried on a dual-core processor show that the computational time can be reduced by a factor 10 using standard GPU boards. This will empower the stereo reconstruction of high resolution images reducing noise in the space-time data, and extending the accuracy of spectra to higher frequencies and wavenumbers. Finally, GPU-based FFT algorithms will be beneficial for the computation of 3D wave spectra at high resolution and surface orbital velocities.

7. REFERENCES

Adler, R.J., 1981. *The Geometry of Random Fields*, New York: John Wiley.

Adler, R.J. & Taylor, J.E., 2007. *Random fields and geometry*. Springer Monographs in Mathematics Springer, New York.

Ballard, D.H., Brown, C.M., 1982. *Computer Vision*. Prentice-Hall, Englewood

Banner, M. L., Jones, S. F., Trinder, J. C., 1989. Wavenumber spectra of short gravity waves. *Journal of Fluid Mechanics*, 198: 321-344.

Baxevani, A., and I. Richlik, 2004. Maxima for Gaussian seas. *Ocean Engn.,* 33(7), 895-911.

Benetazzo, A., 2006. Measurements of short water waves using stereo matched image sequences Coastal Engineering 53:1013-1032

Boccotti P., 2000. *Wave Mechanics for Ocean Engineering*. Elsevier Science, Oxford.

Coté, L.J., Davis, J.O., Marks, W., McGough, R.J., Mehr, E., Pierson, W.J., Ropek, J.F., Stephenson, G., Vetter, R.C., 1960. The Directional Spectrum of Wind Generated Sea as Determined from Data Obtained by the Stereo Wave Observation Project. *Metereological Paper*, 2, No. 6, New York University, College of Engineering.

Dankert, H., Horstmann, J., Lehner, S.,Rosenthal, W.G., 2003. Detection of wave groups in SAR images and radar image sequences. *IEEE Transactionson Geoscience and Remote Sensing* 41,1437–1446.

Dugan, J.P., Piotrowsky, C.C., Williams,J., 2001. *Water depth and surface current retrievals from airborne optical measurements of surface gravity dispersion*. Journal of Geophysical Research, 106 (C8), 16903-16915.

Faugeras,O., 1993. *Three-dimensional Computer Vision: A Geometric Viewpoint*. MIT Press.

Fedele, F. 2008. Rogue Waves in Oceanic Turbulence. *Physica D* 237, 14-17:2127-2131

Fedele F. & Tayfun, M.A. 2009. On nonlinear wave groups and crest statistics" *J. Fluid Mech.* 620, 221-239

Forristall, G. Z., 2000. Wave crests distributions: observations and second order theory. *J. Phys. Oceanogr.*, 38(8): 1931–1943.

Forristall, G.Z. 2006, Maximum wave heights over an area and the air gap problem, OMAE2006-92022 paper, *Proc. ASME 25th Inter. Conf. Off. Mech. Arc. Eng.*, Hamburg.

Forristall, G.Z. 2007, Wave crest heights and deck damage in Hurricanes Ivan, Katrina and Rita, Offshore Technology Conference Proceedings, OTC 18620, Houston.

Gallego G, Benetazzo A., A. Yezzi, Fedele F. 2008 Wave spectra and statistics via a variational wave acquisition stereo system. OMAE2008-57160 paper, *Proc. ASME 27th Inter. Conf. Off. Mech. Arc. Eng.*, Estoril, Portugal.

Grue J., Romero L., Kleiss J., Melville W.K. 2008 Orbital velocity in spatial ocean wave elevation measurement: nonlinear computation and approximation. OMAE2008-57205 paper, *Proc. ASME 27th Inter. Conf. Off. Mech. Arc. Eng.*, Estoril, Portugal.

Jahne, B. ,1993. Spatio-Temporal Image Processing - Theory and Scientific Applications. Springer-Verlag Berlin Heidelberg

Holland, K.T. and R.A. Holman. 1997. Video estimation of foreshore topography using trinocular stereo. *Journal of Coastal Research* 13(1): 81-87

Holland, K.T., R.A. Holman, T.C. Lippmann, J. Stanley, and N. Plant. 1997. Practical use of video imagery in nearshore oceanographic field studies. *IEEE Journal of Oceanic Engineering* 22(1): 81-92.

Holthuijsen, L. H., 1983. Observations of the directional distribution of ocean wave energy, it Journal of Physical Oceanography, 13, 816-827.

Hwang, P.,Wang, D., Walsh, E., Krabill, W., Swift, R., 2000. Airborne measurements of the wavenumber spectra of ocean surface waves, part I: spectral slope and dimensionless spectral coefficient. *Journal of Physical Oceanography* 30, 2753–2767.

Kanade, T., Morris, D. D., 1998. Factorization methods for structure from motion. *Philosophical Transactions-Royal Society. Mathematical, Physical and Engineering Sciences*, the Royal Society 356,1153–1173.

Klette, R., Schlüns, K., Koschan, A., 1998. *Three-Dimensional Data from Images*. Springer, Singapore.

Krogstad, H.E., Liu, J., Socquet-Juglard H., Dysthe K.B. and K. Trulsen, 2004 Spatial Extreme Value Analysis of Nonlinear Simulations of Random Surface Waves, OMAE2004-51336 paper, *Proc. ASME 23th Inter. Conf. Off. Mech. Arc. Eng.*, Vancouver.

Lindgren, G. 1970. Some properties of a normal process near a local maximum. Ann. Math. Statist. 4(6),1870-1883.

Lindgren, G. 1972. Local maxima of Gaussian fields. Ark. fur Mat. 10,195-218.

Ma, Y. Soatto, S., Kosecka, J., Shankar Sastry, S., 2004. *An invitation to 3-D vision: from \images to geometric models.* Springer-Verlag New York

Phillips, O.M., 1958. The equilibrium range in the spectrum of wind-generated waves, *Journal of Fluid Mechanics*, vol. 4, no. 4, pp. 426-434.

Phillips, O.M., 1985. Spectral and statistical properties of the equilibrium range in wind-generated gravity waves, *Journal of Fluid Mechanics*, vol. 156, pp. 505-531.

Piterbarg V. 1995 *Asymptotic Methods in the Theory of Gaussian Processes.* American Mathematical Society, ser. Translations of Mathematical Monographs, Vol. 148, 205pp.

Pollefeys, M., 2000. *Tutorial on 3-D modelling from images*. Lecture Notes

Santel, F., Heipke, C., Könnecke, S., Wegmann, H., 2002. Image Sequence Matching for the Determination of three-dimensional Wave Surfaces. P*roceedings of the ISPRS Commission V Symposium*, Corfu, Greece, Volume XXXIV Part 5, 596-600.

Shemdin, O. H., Tran, H. M., Wu, S. C., 1988. Directional Mesurements of short ocean waves with stereography. *Journal of Geophysical Research*, 93, 13891-13901.

Schumacher, A., 1939. Stereophotogrammetrische Wellenaufnahmen. *Wiss. Ergeb. Dtsch. Atlant. Exped. Forschungs Vermessung*. "Meteor" 1925-1927, Ozeanographische Sonderuntersuchungen, Erste Lieferung, Berlin.

Stewart RH, Joy JW. 1974 HF radio measurements of surface currents. Deep-sea research 21(12):1039-1049

Stockdon, H. F., Holman, R. A., 2000. Estimation of wave phase speed and nearshore bathymetry from video imagery. *Journal of Geophysical Research,* 105 (C9), 22, 015–22, 033.

Sugimori, Y.,1975. A study of the application of the holographic method to the determination of the directional spectrum of ocean waves. *Deep Sea Research*, 22, 339-350.

Tayfun, MA 1986. On narrow-band representation of ocean waves. Part I: Theory. *J. Geophys. Res*., (1(C6):7743-7752

Tayfun, M.A., Fedele, F., 2007a, Wave-height distributions and nonlinear effects, *Ocean Engineering*, vol. 34, no. 11-12, pp. 1631-1649

Tayfun, M.A., & Fedele F. 2007b. Expected shape of extreme waves in sea storms. *Proc. ASME 26th Inter. Conf. Off. Mech. Arc. Eng.*, San Diego, USA.

Wanek, J.M. and Wu, C.H., 2006. Automated trinocular stereo imaging system for three-dimensional surface wave measurements, *Ocean Engineering*, 33(5-6) 723-747.

Worsley, K.J. 1995. Boundary corrections for the expected Euler characteristic of excursion sets of random fields, with an application to astrophysics. *Adv. App. Prob.*, 27:943-959.

Zakharov, V.E., 1999, Statistical theory of gravity and capillary waves on the surface of a finite-depth fluid, *Eur. J. Mech. B Fluids* 18(3):327-344

Zhang, Z., 2000. A flexible new technique for camera calibration. *IEEE Transactions on Pattern Analysis and Machine Intelligence*, 22(11):1330-1334